Enhancing time-resolved THz systems through the integration of optical fibers

by

Nicolas Couture

Thesis submitted in partial fulfillment
of the requirements for the
Doctorate in Philosophy degree in Physics

Department of Physics
Faculty of Science
University of Ottawa

Abstract

Time-resolved terahertz (THz) spectroscopy is an emerging optical characterization technique with the potential of becoming standard practice in fundamental research and in industry. These systems have the ability to be extremely broadband and can retrieve the phase and amplitude information of a THz pulse transmitted through a material, allowing the complex dielectric function of the material to be extracted. Although these systems are already extremely impactful, they nonetheless have their shortcomings. Namely, the data acquisition time required for a single measurement hinders their practicality in an industrial setting or retrieving interesting dynamics within a sample that are occurring on faster timescales. Moreover, broadband THz systems carry a significant financial burden as they rely on ultrafast near-infrared (NIR) sources delivering sub-100 fs pulses, limiting their accessibility. In this work, we address these issues plaguing time-resolved THz systems with the implementation of optical fibers.

We begin by describing the physical processes governing ultrashort pulse propagation in fiber and the generation and detection of THz pulses via nonlinear effects in semiconductor crystals. We then design and demonstrate a THz detection scheme able to resolve each of the generated THz pulses at a repetition rate of 50 kHz. This includes using fiber to generate a chirped NIR supercontinuum, imprinting THz waveforms onto the NIR spectrum and thereby enabling single-shot THz detection; and using fiber to achieve photonic time-stretch, a technique allowing us to detect each of the THz-encoded NIR pulses with high-speed electronics at a rate determined by the repetition rate of the laser. The resulting system is then used to track carrier dynamics in a semiconductor as they are dynamically accumulating and recombining.

We then combine nonlinear propagation in optical fiber with a time-resolved THz system allowing us to achieve broadband THz generation and detection. We describe two systems relying on this general scheme: The first system relies on a compact and cost-effective laser source and a standard fiber to generate and detect a THz spectrum extending up to 6 THz, alleviating the financial strain imposed by systems relying on sophisticated laser sources without sacrificing performance. The other system relies on an amplified laser source and gas-filled hollow-core photonic crystal fiber (PCF) to generate a tunable spectrum up to 20 THz.

Finally, we investigate the generation of a supercontinuum spanning more than two octaves inside a highly nonlinear solid-core PCF. For the first time, we explore both the spectral intensity and polarization structure of such a broad optical spectrum approaching the mid-infrared region.

List of Publications

Articles published in peer-reviewed journals

1. **N. Couture**, J. Schlosser, A. Ahmed, M. Wahbeh, G. Best, A. Gamouras, and J.-M. Ménard, "Compact, low-cost, and broadband terahertz time-domain spectrometer," *Appl. Opt.* **62**, 4097-4101 (2023).

2. **N. Couture**, W. Cui, M. Lippl, R. Ostic, D. J. J. Fandio, E. K. Yalavarthi, A. Vishnuradhan, A. Gamouras, N. Joly, and J.-M. Ménard, "Single-pulse terahertz spectroscopy monitoring sub-millisecond time dynamics at a rate of 50 kHz," *Nat. Commun.* **14**, 2595 (2023).

3. **N. Couture**, R. Ostic, P. H. Reddy, A. K. Kar, M. C. Paul, and J.-M. Ménard, "Polarization-resolved supercontinuum generated in a germania-doped photonic crystal fiber," *J. Phys. Photonics* **3**, 025002 (2021).

4. A. Halpin, **N. Couture**, and J.-M. Ménard, "Optical pulse structuring in gas-filled hollow-core PCF for generation and detection of phase-locked multi-THz pulses," *Opt. Mater. Express* **9**, 3115-3122 (2019).

5. W. Cui, A. W. Schiff-Kearn, E. Zhang, **N. Couture**, F. Tani, D. Novoa, P. St. J. Russell, and J.-M. Ménard, "Broadband and tunable time-resolved THz system using argon-filled hollow-core photonic crystal fiber," *APL Photonics* **3**, 111301 (2018).

Pre-prints

1. D. J. J. Fandio, A. Vishnuradhan, E. K. Yalavarthi, W. Cui, **N. Couture**, A. Gamouras, and J.-M. Ménard, "Sub-zeptojoule detection of terahertz pulses by parametric frequency upconversion," *arXiv*: 2310.08452 (2023).

2. **N. Couture**, M. Lippl, W. Cui, A. Gamouras, N. Y. Joly, and J.-M. Ménard, "Performance analysis of table-top single-pulse terahertz detection up to 1.1 MHz," *arXiv*: 2309.09803 (2023).

Conference proceedings

1. **N. Couture**, M. Lippl, W. Cui, R. Ostic, D. J. J. Fandio, E. K. Yalavarthi, A. Vishnuradhan, A. Gamouras, N. Joly, and J.-M. Ménard, "Towards single-pulse terahertz spectroscopy at MHz rates," *48th International Conference on Infrared, Millimeter, and Terahertz Waves (IRMMW-THz)*, pp. 1-2 (2023).

2. **N. Couture**, A. Ahmed, M. Wahbeh, G. Best, A. Gamouras, and J.-M. Ménard, "Development of a portable, broadband, and sensitive terahertz time-domain spectrometer," *SPIE Photonics West* 124050A (2023).

3. A. Gamouras, **N. Couture**, W. Cui, M. Lippl, R. Ostic, D. J. J. Fandio, E. K. Yalavarthi, A. Vishnuradhan, N. Y. Joly, and J.-M. Ménard, "Capturing microsecond dynamics one pulse at a time: single-shot time-resolved terahertz spectroscopy at 50 kHz," *SPIE Photonics West* PC12419 (2023).

4. **N. Couture**, W. Cui, M. Lippl, R. Ostic, D. J. J. Fandio, E. K. Yalavarthi, A. Vishnuradhan, A. Gamouras, N. Joly, and J.-M. Ménard, "Resolving sub-millisecond dynamics with single-pulse terahertz time-domain spectroscopy," *Frontiers in Optics* FW6C.2 (2022).

5. R. Ostic, **N. Couture**, P. H. Reddy, A. K. Kar, M. C. Paul, and J.-M. Ménard, "Simulation of depolarization effects during supercontinuum generation in optical fiber," *Photonics North* 1-1 (2021).

6. **N. Couture**, R. Ostic, P. H. Reddy, A. K. Kar, M. C. Paul, and J.-M. Ménard, "Polarization resolution of a fiber-based supercontinuum spanning more than two octaves," *Frontiers in Optics* FTh1E.5 (2020).

7. **N. Couture**, R. Ostic, P. H. Reddy, S. Das, A. Dhar, M, Pal, M. C. Paul, A. K. Kar, and J.-M. Ménard, "Polarization analysis of a supercontinuum generated in a germania-doped photonic crystal fiber," *CLEO: Science and Innovations* JW2E.12 (2020).
   Winner of best student poster awarded by Optica (formerly OSA) optical fiber modeling and fabrication technical group.

8. W. Cui, A. W. Schiff-Kearn, E. Zhang, **N. Couture**, F. Tani, D. Novoa, P. St. J. Russell, and J.-M. Ménard, "Frequency-tunable THz source using Ar-filled HC-PCF pulse shaper," *Photonics North* 1-1 (2018).

Acknowledgements

There are so many people that helped me along this journey. Jean-Michel, thank you for the guidance and support you have provided over the better part of a decade. I joined your group as a clueless undergraduate student just trying to fulfill graduation requirements, oblivious to the world of THz, photonics, and even academia as a whole. Thank you for giving me the opportunity to do research abroad, go to *many* conferences, and introduce me to amazing and brilliant people along the way. Your passion for science is contagious and without your confidence in me, this thesis would not exist. I am extremely grateful that our paths crossed, and you were able to introduce me to such an interesting and ripe field of research. I'm proud of everything we have accomplished in this time and know that the group will continue to thrive under your leadership. Angela, I find it funny how we first met through my co-op placement at NRC and we ended up working together again years later! You have been like a second supervisor to me since joining the group through the JCEP collaboration a few years ago. Thank you for the advice and guidance you've given me in that time. Whether your advice was about research or about life, it was invaluable, and I appreciate it.

To all the students and postdocs I've had the pleasure of working with, thank you so much. Wei, being two of the group's first members, we literally built this lab from the ground up. Although moving optical tables into the lab, building a customized shelving unit above the tables, and constant laser/plumbing troubleshooting isn't considered "research", it was essential to every project and I'm grateful we were able to do this together. I'm also grateful for the *actual* research we got to work on together. It was always nice bouncing ideas off each other in the lab to solve problems. I wish you luck in your future endeavors, I know you will continue to do outstanding work. Markus, it was a real pleasure working together, I'm glad we've had multiple opportunities to do so and that I've succeeded in transforming you into a "THz guy" even though you refuse to admit your love of THz. Please continue to have crazy ideas and convincing others to help you execute them! I know that you will do great things in the future, and I wish you the best of luck. Who knows, maybe we will even collaborate in the future. Rachel, although we only had a few years working together, we were efficient with this time and got some nice results, results which make up a large portion of this thesis. Thank you for being an awesome collaborator and Matlab wizard. Alexei, Lauren, your stays with the group were even shorter, but I

learned so much from you two and you set the bar so high. I'm so thankful I got to work with you both. Finally, thank you to all the past and present lab mates that I haven't mentioned by name – I may not have worked with you as closely, but we have spent a lot of time together during our weekly two-hour-long group meetings, which were three hours if Ahmed was chairing the meeting. I wish you all the best in your research and all your future endeavors. The lab is in your hands now!

I've been blessed with so many lifelong friendships, old and new, and they've all played an important part in this thesis. To *The Squad*, thank you for all the gaming sessions and long weekends together to blow off some steam. I wouldn't trade "squadtoberfest", "squadmas/squadmas in July", "squadoween", or any other ridiculously named event we've had for the world. Felix, Emily, Sam, and Nick I am so grateful for the (too many) pitchers of beer we have consumed together. Josh, Tom, and Andre, it was always fun sharing our grad school experiences over a few beers, even though I couldn't relate to the struggles your chemistry/biology experiments entailed. I thank you guys for that and the insane number of barbecues we've had together.

To my parents, thank you so much for your love and support not only during grad school, but my whole life. You both showed me that hard work and perseverance can lead to great things. Thank you for teaching me the values that make me who I am today and for the patience you've always had with me (especially when I was a moody teenager). Thank you for the precious advice you've given me over the years, I don't know where I'd be without you.

Last, but certainly not least, Kendra, thank you for always being there to support me. You've been an amazing partner through all of this. Your sacrifices did not go unnoticed and I promise to return the favor in the future. I'm so grateful that my extended stay in university did not get in the way of us starting a life together. Thank you for taking care of Marlow, making dinner during the countless evenings/nights I was staying late in the lab, celebrating the little victories, and for listening to me rant about interesting results even when you had no idea what I was talking about. You are one of the main reasons I was able to complete my PhD in a timely fashion, giving me a pep talk when I needed one and telling me to take a break when you knew I needed it. I'm excited to see where life will take us from here.

Statement of originality and collaborative contributions

To the best of his knowledge, the author states that the work described in this thesis constitutes original research. Author contributions to each of the publications in this thesis are listed below.

Chapter 4 contains the paper entitled "Single-pulse terahertz spectroscopy monitoring sub-millisecond time dynamics at a rate of 50 kHz" which was published in *Nature Communications* in 2023. N. Couture, W. Cui, and M. Lippl built the final system, performed the experiments, and collected data for the paper. N. Couture made the figures, drafted the original manuscript, and handled the correspondence with the editor. R. Ostic built the first version of the experimental apparatus with the help of L. Gingras. N. Couture and D.J.J. Fandio performed the simulations on photocarrier dynamics with assistance from E.K. Yalavarthi and A. Vishnuradhan. A. Gamouras, N.Y. Joly, and J.-M. Ménard supervised the project and the drafting of the original manuscript. All authors reviewed and contributed to the published manuscript.

Chapter 5 contains the paper entitled "Compact, low-cost, and broadband terahertz time-domain spectrometer" which was published in *Applied Optics* in 2023. N. Couture built the terahertz system, acquired and analyzed experimental data, made the figures, and drafted the original manuscript. J. Schlosser assisted with the acquisition and analysis of experimental data. A. Ahmed, M. Wahbeh, and G. Best designed the peak-field booster with the assistance of N. Couture. A. Gamouras and J.-M. Ménard supervised the project and the drafting of the original manuscript. All authors reviewed and contributed to the published manuscript.

Chapter 5 also contains the paper entitled "Optical pulse structuring in gas-filled hollow-core kagomé PCF for generation and detection of phase-locked multi-THz pulses" which was published in *Optical Materials Express* in 2019 as an invited research article. A. Halpin and N. Couture acquired and analyzed experimental data and both authors played significant roles in the drafting of the original manuscript. N. Couture made the figures with the assistance of A. Halpin. J.-M. Ménard supervised the project. All authors reviewed and contributed to the published manuscript.

Chapter 6 contains the paper entitled "Polarization-resolved supercontinuum generated in a germania-doped photonic crystal fiber" which was published in *Journal of Physics: Photonics* in 2021. N. Couture performed the experiments with the help of R. Ostic, made the figures, and drafted the original manuscript. R. Ostic performed the simulations with the help of N. Couture. P.H. Reddy, A.K. Kar, and M.C. Paul designed and fabricated the photonic crystal fiber used in this work and experimentally characterized its dispersive properties with a Mach-Zehnder interferometer. J.-M. Ménard supervised the supercontinuum experiments and the drafting of the original manuscript. All authors reviewed and contributed to the published manuscript.

Table of Contents

List of Figures

List of Tables

Chapter 1

Introduction

1.1 Nonlinear fiber optics

An optical fiber is a thin, flexible, and transparent filament made of high-quality glass that is used to transmit light over long distances. It consists of a core, which is the central region through which light travels, and a cladding layer that surrounds the core to confine the light within the fiber. In standard fibers, the core and cladding have different refractive indices which enables the fiber to guide light through total internal reflection. The core of an optical fiber is typically made of high-purity silica glass, which has excellent optical properties and low attenuation in the near-infrared (NIR) regime. The diameter of the core is typically on the order of a few micrometers to a few tens of micrometers, depending on the type of fiber. The cladding layer is made of a slightly lower refractive index material, such as a different type of glass or a polymer. This property allows light to be transmitted through the fiber with minimal loss. To further enhance the light-guiding properties, optical fibers often have a protective outer coating called the buffer or jacket. The buffer prevents moisture from entering, protects the fiber from physical damage, and provides mechanical strength resulting in lower bend-related loss.
Since the development of the first low-loss optical fiber in 1970 [6], researchers immediately flooded journals with impressive results in the field of fiber optics, and still do to this day. Notably, advances in fiber fabrication reduced the losses enough to enable the use of fibers in communication systems, allowing light to be detected after propagation through several

kilometers of fiber and offered significantly higher bandwidth capacity, speed, and reliability in comparison to traditional copper wires. Since silica has moderately low nonlinearity, fibers were not immediately considered viable vessels for nonlinear optical experiments. Soon enough, however, nonlinear effects in fiber relevant to this work were observed experimentally [7, 8, 9, 10, 11, 12, 13].

Optical fibers offer certain advantages over bulk nonlinear materials. Fibers transmit relatively intense optical fields over long propagation lengths, keeping the mode tightly confined ($\sim$5 μm spot size for single-mode fibers) throughout the whole fiber. In most situations, small spot sizes are only attainable at a single point when focusing light into bulk material. Moreover, fibers offer more versatility compared to bulk material. Surrounding a fiber core with structured air holes along the length of the fiber can alter the dispersive properties of the fiber, providing tunability and enhancement of phase matched nonlinear processes. These are known as microstructured fibers or photonic crystal fibers (PCFs) [14, 15, 16], which utilize a guiding mechanism equivalent to total internal reflection [17]. Though fiber properties can be exploited to suit certain applications, in this work, we use fiber to overcome issues impacting time-resolved terahertz (THz) systems and to generate a supercontinuum (SC) in the optical regime.

Supercontinuum generation refers to the situation where an extremely broadband spectrum is produced via nonlinear effects from a narrow-band pulse. Although a SC can be generated in bulk material [18], SC generation in fiber is often the method of choice as similar spectra can be produced with only a fraction of the optical intensity required in bulk. Dudley, Genty, and Coen summarize bulk- and fiber-based SC sources nicely in their famous review paper [19]. Even now, fiber-based SC sources are studied extensively as they benefit a considerable number of applications including coherent anti-Stokes Raman spectroscopy (CARS), ultrashort pulse generation, and time-resolved absorption spectroscopy [20]. Some properties of fiber-based SC, like polarization, are occasionally overlooked. When characterizing the polarization properties of the SC, often, only a single wavelength (the pump wavelength) is explored. In reality, light at different wavelengths behaves differently as they propagate through the fiber. In this work, namely chapter 6, we explored the polarization properties of a SC generated in a germania-doped PCF.

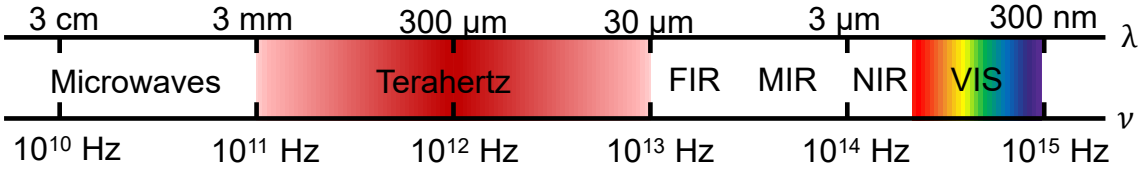

Figure 1.1: Electromagnetic spectrum in frequency (ν) and wavelength (λ) highlighting the THz band between 0.1 and 10 THz, also known as the gap between optics (IR) and electronics (microwaves).

1.2 THz radiation

The THz band roughly corresponds to frequencies between 0.1 and 10 THz. Figure 1.1 displays a portion of the electromagnetic spectrum spanning from the microwave to the UV regimes. This part of the spectrum is often divided into two subsection, the low frequency side (microwaves) corresponds to the field of electronics and the high frequency side (IR to UV) corresponds to optics [1]. Between them lies the THz band, which is occasionally referred to as the bridge between optics and electronics. This frequency gap remained relatively unexplored at first due to the incompatibility of sources and detectors in the THz band from the surrounding regimes of the electromagnetic spectrum.
With the exception of the Auston switch (otherwise known as a photoconductive antenna) [21], the first sources filling the THz gap were mostly continuous wave (CW) sources (Fig. 1.2). Advancements in optics and electronics, for instance the development of chirped-pulse amplification which rightfully won the Nobel prize in physics in 2018 [22], enabled key THz generation and detection capabilities. This advancement in laser technology permitted the use of nonlinear crystals to generate high intensity THz pulses as crystals have a higher damage threshold than Auston switches [23] and the strength of the generated THz pulses is directly dependent on the NIR pulse energy. The broader spectral coverage of chirped-pulse amplification-enabled femtosecond sources combined with the broadband transmittance of nonlinear crystals also permitted the generation and detection of extremely broadband THz pulses beyond the limit of Auston switches, providing the ability to probe a wider range of resonances in the THz regime with a single measurement. Light in this frequency band has certain properties that we can capitalize on for some interesting applications.

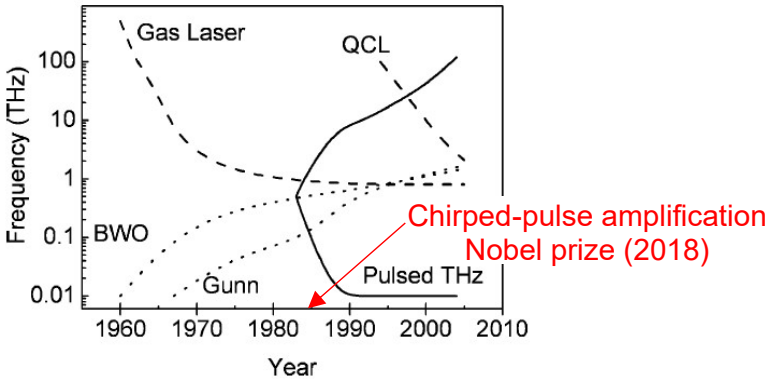

Figure 1.2: Graphical representation of coherent THz sources gradually filling the THz gap from [1]. Dashed lines represent CW THz sources and solid lines represent pulsed THz sources. Strickland and Mourou's work on chirped-pulse amplification in 1985 on high-intensity ultrashort pulses aided in the generation of broadband THz pulses. BWO: backward-wave oscillator; QCL: quantum cascade laser.

1. THz radiation is virtually harmless to humans. Its photon energy is not high enough to induce photoionization and is therefore unable to alter organic products (contrary to high photon energies in the UV and X-ray regimes) and would therefore be suitable as a non-invasive probe for quality control of food and drugs [24]. Moreover, it is heavily absorbed by water and therefore cannot penetrate past the skin [25].

2. It can be transmitted through many dielectric materials like cardboard, wood, and plastics; allowing us to examine contents of containers without opening them. For example, THz radiation has been used to read a book without opening it [26], which is crucial for archaeological purposes if, say, an old book does not have the structural integrity to be opened. Moreover, if we are to combine these two unique advantages of THz radiation, we have ourselves a valid tool for security purposes that can image what is hidden under clothing or in a box without harming the person being imaged or altering the contents inside the container [27].

3. Many molecules exhibit strong rotational and vibrational resonances in the THz regime. Each molecule has a unique absorption spectrum and THz radiation can

therefore be used to retrieve the spectral fingerprint of molecules [28].

4. THz waves hold promise as a carrier for indoor and outdoor wireless communication at unprecedented speeds due to its higher bandwidth capacity compared to microwaves [24, 29, 30].

5. In fundamental research, it can be used as a probe to characterize novel materials. For instance, THz radiation can reveal microscopic conductivity dynamics in atomically thin materials like graphene without applying an external gating voltage [31, 32].

To turn these listed applications into standard technologies, sophisticated THz systems need to be developed and optimized. Certain systems can be developed to tackle certain issues. For instance, THz detection speed may not be crucial for spectral fingerprinting, but a wide THz bandwidth may be necessary to extract as much information as possible in a single measurement (and with a single source). In quality control settings, a large bandwidth may not be essential, but fast THz detection is critical to keep up with manufacturing rates. In all cases, however, the cost of the system is always a factor in the implementation of a new tool. In the work presented in this thesis, we have developed several THz systems tackling separate issues in THz time-domain spectroscopy. In each THz system, presented in chapters 4 and 5, we use optical fibers to overcome certain limitations that are common to time-resolved THz spectroscopy configurations.

1.3 Outline

This thesis is structured as follows:
Chapter 2 contains background information regarding nonlinear propagation in fibers and THz generation and detection that the reader will find useful for ensuing chapters.
Chapter 3 provides intricate details about the experiments found in this thesis that are not discussed in the published papers associated to later chapters. This includes a detailed characterization of the ultrafast source used in most of this work, how to efficiently couple light into an optical fiber from a free-space source, and how to initially align a time-resolved THz spectrometer.
In chapter 4, we provide a solution to the data acquisition time required in standard THz time-domain spectrometers. We use standard silica fibers to generate broadband and chirped NIR spectra to achieve single-shot THz detection through chirped-pulse spectral encoding, and another fiber to realize single-pulse THz detection via a photonic time-stretch technique whose detection rate is set by the repetition rate of the laser [33]. Though the system was operated at a repetition rate of 50 kHz, resolving each of the THz waveforms every 20 μs, the system may be operated at arbitrarily fast rates with an appropriate ultrafast source. We used this tool to track optically injected carrier dynamics in a semiconductor as successive NIR pump pulses increased the carrier density and altered their spatial distribution.
In chapter 5, we use a standard fiber to broaden the NIR spectrum from a weak, compact, and low-cost femtosecond source to develop a broadband and cost-effective THz time-domain spectrometer, delivering a THz spectrum up to 6 THz with 50 dB dynamic range. This work provides a practical solution to the financial burden imposed by broadband THz systems which require sources delivering sub-100 fs NIR pulses, making THz spectroscopy a more accessible tool to researchers in all fields [34].
Chapter 5 also includes a system which tackles bandwidth issues imposed by an ultrafast source, but to an extreme. A gas-filled hollow-core PCF (HCPCF) is used to dramatically broaden NIR spectra such that THz frequencies up to 20 THz are generated and detected [35]. By simply altering the NIR pulse energy injected into the HCPCF, we tune the central frequency of the generated and detected THz spectra.
We conclude by summarizing a project in chapter 6, which aimed to utilize SC generation in fiber to generate mid-IR light. Though this result was not achieved, we discovered in-

teresting polarization properties of broadband spectra and solitons as they propagate in fiber. We experimentally resolved the degree of linear polarization across a broad supercontinuum to emphasize this phenomenon and found that higher optical frequencies are more susceptible to depolarization during propagation in the fiber and solitons preserve their polarization [36].

This thesis demonstrates the versatility of optical fibers and how they may provide straightforward solutions to common obstacles hindering the performance of systems operating in different regions of the electromagnetic spectrum.

Chapter 2

Theory

In this chapter, we discuss the theoretical background of physical processes found throughout this thesis. First, we explore propagation of ultrashort NIR pulses in optical fibers. This includes the linear and nonlinear effects one must consider for an accurate description of sub-picosecond pulse propagation in a fiber. Next, we cover THz generation through optical rectification, and THz detection via electro-optic sampling and chirped-pulse spectral encoding. Finally, we describe the process of extracting material parameters from time-domain THz spectroscopy data.

2.1 Ultrashort pulse propagation in optical fibers

For the sake of simplicity, we limit the topic of this section to pulse propagation in standard single-mode fibers made of silica. Standard optical fibers use a step-index configuration to guide light. Step-index fibers consist of a solid high-quality silica glass core whose index of refraction (n_1) is slightly higher than the index of the cladding layer surrounding it (n_c), as depicted in Fig. 2.1. These fibers utilize total internal reflection to guide light over extremely long distances. The term "single-mode" is rather self-explanatory: the fiber can only support a single mode. This means that the fiber will only transmit optical waves with a specific field pattern. The number of modes supported by the fiber is determined

by the V parameter

$$V = \frac{2\pi}{\lambda} a \sqrt{n_1^2 - n_c^2} \tag{2.1}$$

where λ is the wavelength of the light, a is the radius of the core, and $V < 2.405$ is the single-mode condition for the fiber [37]. As it is the most straightforward manner, the radius of the glass core is often the parameter that is varied when fabricating single- and multi-mode fibers; single-mode fibers having the smaller core size. Single-mode silica fibers propagating light with a wavelength near 1 μm have a core diameter on the order of 5 μm. As a result, since the mode is confined more tightly in single-mode fibers, nonlinear effects become more prominent. In this thesis, we aim to take advantage of nonlinear effects in fibers and therefore utilize single-mode fibers, but must also consider the consequences of linear effects.

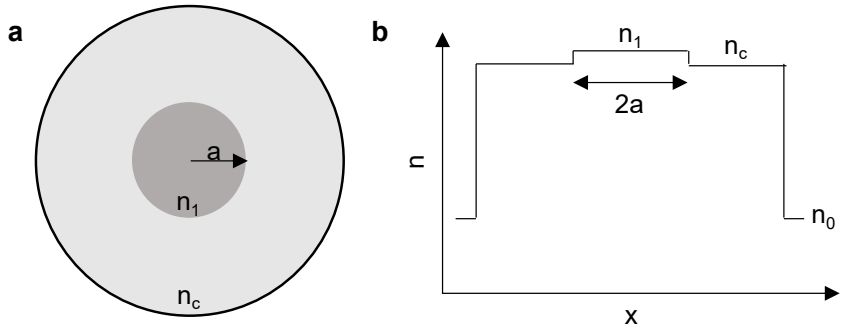

Figure 2.1: a) Schematic cross-section of step-index fiber of radius a, core index n_1 and cladding index n_c. b) Index profile as function of radial distance x.

2.1.1 Dispersion

In terms of ultrashort pulse propagation in fiber, where the spectral bandwidth is relatively large, chromatic dispersion plays an especially important role as it is a result of the frequency dependence of the refractive index. For instance, a Gaussian pulse with a sub-100 fs time duration has a broad spectral bandwidth on the order of ~5 THz. The spectral components at the edges of the spectrum can therefore experience strongly differing refractive indices, thus travelling at significantly different speeds within the fiber ($v(\omega) = c/n(\omega)$).

This effect leads to temporal broadening of the pulse, or, in other words, a pulse with a longer duration, which can be an undesired effect if one wants to use this pulse for a nonlinear optical process later on. Chromatic dispersion is often characterized by the propagation constant $\beta = n(\omega)\omega/c$, which is Taylor expanded about the central frequency of the light ω_0

$$\beta(\omega) = \frac{n(\omega)\omega}{c} = \beta_0 + \beta_1(\omega - \omega_0) + \beta_2\frac{(\omega - \omega_0)^2}{2} + ... \tag{2.2}$$

where

$$\beta_m = \left(\frac{d^m\beta}{d\omega^m}\right)_{\omega=\omega_0} \tag{2.3}$$

The first term in equation 2.2 provides information on the effective refractive index of the mode in the fiber. Performing the first derivative, we find that β_1 is related to the group velocity such that

$$\beta_1 = \frac{d}{d\omega}\left(\frac{n(\omega)\omega}{c}\right) = \frac{1}{c}\left(n(\omega_0) + \omega_0\frac{dn}{d\omega}\right) = \frac{n_g}{c} = v_g^{-1} \tag{2.4}$$

where we have introduced the group index $n_g = n(\omega_0) + \omega_0\frac{dn}{d\omega}$. The group velocity refers to the speed at which the pulse envelope, centered about ω_0, travels in the fiber. In the same spirit, we find

$$\beta_2 = \frac{1}{c}\left(2\frac{dn}{d\omega} + \omega_0\frac{d^2n}{d\omega^2}\right) \tag{2.5}$$

which is related to the group velocity dispersion (GVD) expressed in units of fs^2/mm and is often referred to as the group velocity parameter. When $\beta_2 > 0$, it produces an effect known as up-chirp, where the lower frequency components travel faster than the higher frequency components and the frequency of the pulse therefore increases with time. Conversely, down-chirp corresponds to the $\beta_2 < 0$ case, where the frequency of the pulse decreases with time. Note that fiber manufacturers often present the dispersion parameter D rather than β_2, which are related through $D = \left(\frac{-2\pi c}{\lambda^2}\right)\beta_2$ and D is expressed in units of ps/(nm km). In bulk material, dispersion parameters are entirely determined by the material properties. In fiber, however, we must consider the dielectric waveguiding as well as the material dispersion in order to obtain the full dispersive properties of the fiber. Microstructured optical fibers (or PCFs), which consist of capillaries (air holes) surrounding the core along the length of the fiber with specific diameter and spacing (pitch) between them, are a way of altering the waveguide properties to gain control of the linear and nonlinear properties

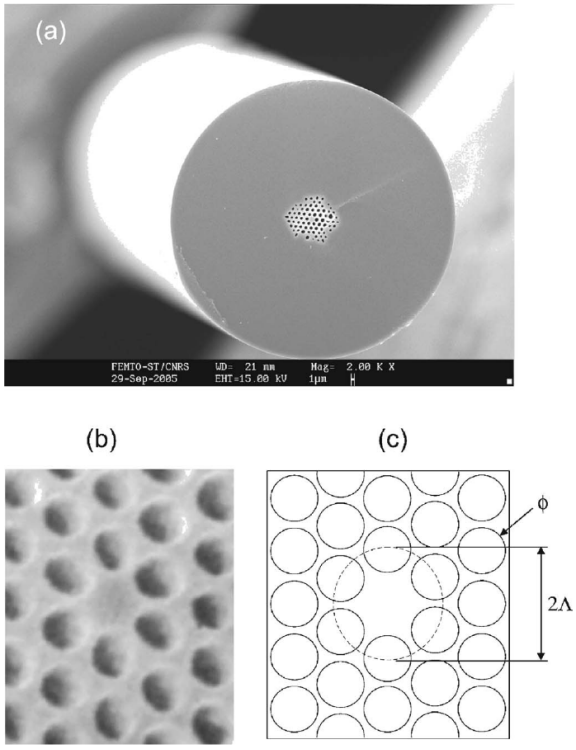

Figure 2.2: a) PCF cross-section of fiber used in [2] and b) same image emphasizing the solid core surrounded by capillaries. c) Schematic design of the fiber structure with a pitch of $\Lambda = 1.6$ μm and hole diameter $\phi = 1.4$ μm.

of the fiber while permitting single-mode guidance for all wavelengths [38, 39, 40]. One of the first PCFs ever made, from Ranka *et al.*, is shown in Fig. 2.2 [2]. Single-mode guidance is a desirable feature as the spatial profile of high order fiber modes are complex and can be difficult to handle and often experience more loss. Solving Maxwell's equations, one finds that fibers support the family of modes known as LP modes, some of which are shown in Fig. 2.3 as an example, where the LP_{01} mode (fundamental mode) is nearly Gaussian [3]. In general, the dispersion profile of a fiber has three main regions: the normal dispersion regime ($\beta_2 > 0$), the anomalous dispersion regime ($\beta_2 < 0$), and the zero-dispersion wavelength (ZDW). A standard fiber has a ZDW near 1250 nm, anomalous dispersion regime $\lambda >$ ZDW, and normal dispersion regime $\lambda <$ ZDW. In exceptional cases, the dispersion profile can be altered drastically enough to engineer fibers with two ZDWs [41, 42] or even

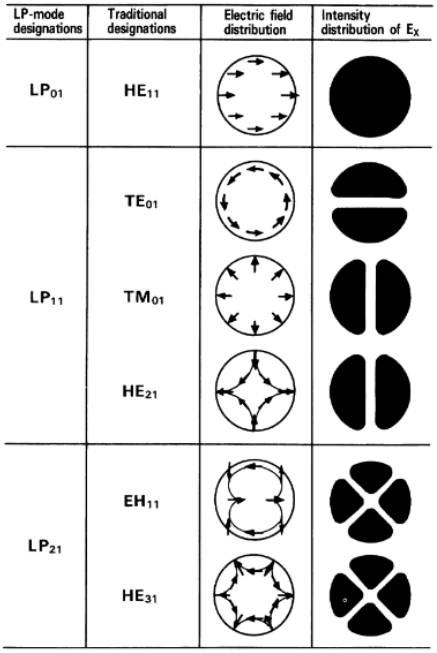

Figure 2.3: Modes supported by multimode fibers. Higher order modes (LP_{11} and LP_{21}) have complex electric field and intensity distributions, rendering them undesirable for certain applications while LP_{01} mode is similar to the Gaussian profile of laser sources [3].

all-normal dispersion [43, 44].

In a perfect world, when fabricating an optical fiber, environmental conditions are perfectly stable throughout the process and the result is a fiber with perfect cylindrical symmetry along the entire fiber length. In reality, environmental fluctuations throughout the fiber drawing process result in random asymmetry of the core along the fiber, causing crosstalk between orthogonal polarization states; this concept is at the core of chapter 6. The random fluctuations in core size can be approximated by an effective elliptical core along the whole fiber whose major and minor axes, also known as the principal axes of the fiber, possess a birefringence, i.e., individual refractive indices n_x and n_y. As a result, orthogonal polarization components travel at different speeds in the fiber; this effect is known as polarization mode dispersion (PMD). The axis with the lower index is referred to as the fast axis and the axis with the higher index is referred to as the slow axis. The polarization state of the light exiting an optical fiber can be heavily affected due to PMD. As an ex-

ample, let us consider the situation where we inject linearly polarized light at a 45 degree angle relative to one of the principal axes of the fiber, distributing an equal amount of light into each of the orthogonal axes. The phase between light travelling in the slow and fast axes of the fiber varies along the fiber, shifting the polarization from linear, to circular, to linear, to circular, and finally back to the input polarization state, as schematically shown in Fig. 2.4. The fiber length corresponding to the situation where the polarization state of the output light matches that of the input state is known as the beat length (L_B). Hence, the length of the fiber must be carefully chosen if the output polarization state is a crucial parameter.

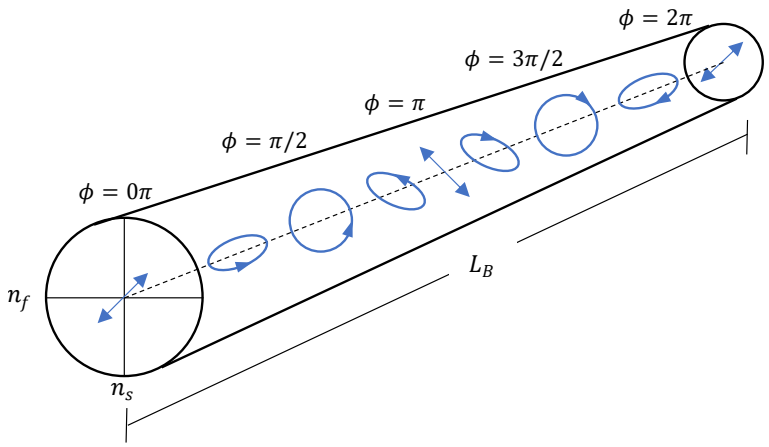

Figure 2.4: Polarization state along birefringent fiber where the fast and slow axes are defined by their refractive indices n_f and n_s, respectively, where $n_s > n_f$. The initially linearly polarized light, injected 45 degrees from a principal axis, varies along the fiber length due to PMD, returning to its original state after a single beat length (L_B). The phase shift between orthogonal polarization components (ϕ) over a single beat length corresponds to 2π. Figure adapted from [4].

Instead of relying on fiber fabrication imperfections as a source of birefringence, purposely fabricating an elliptical core or introducing stress rods can induce large amounts of birefringence. Such fibers reduce the amount of crosstalk between orthogonal polarization states to allow light to preferentially travel along a single fiber axis to preserve linear polarization, hence the reason these fibers are called polarization-maintaining fibers (PMFs) [45]. The

high birefringence results in significantly different propagation constants associated to each fiber axis, β_s and β_f, where the subscripts s and f indicate the slow and fast axes. The phase between orthogonal modes therefore drifts away from each other after very short propagation lengths in the fiber, minimizing the number of fiber imperfections the two modes can experience while in phase. It is important to note, however, that birefringence is also a frequency-dependent parameter, and such fibers may not perform optimally over a broad spectral bandwidth, as we will see in chapter 6. The birefringence and beat length are related through the expression

$$B = \lambda L_B^{-1}. \tag{2.6}$$

Extracting L_B at different wavelengths will therefore retrieve the birefringence of the fiber. As is the case with sub-picosecond pulse propagation in single-mode fibers, nonlinear effects occurring in the fiber can spectrally broaden the spectrum enough to reach this regime.

2.1.2 Nonlinear propagation in fiber

When a medium is exposed to intense optical fields, such as femtosecond NIR pulses, its response becomes nonlinear. The total polarization of the material can therefore be written as

$$\vec{P} = \varepsilon_0\Big(\chi^{(1)}\vec{E} + \chi^{(2)}\vec{E}^2 + \chi^{(3)}\vec{E}^3 + ...\Big) \tag{2.7}$$

where ε_0 is the permittivity of free space, $\chi^{(j)}$ is the j^{th} order susceptibility ($j > 1$ corresponding to the nonlinear terms), and $\vec{E}$ is the electric field [46]. The first order susceptibility is the dominating component of $\vec{P}$ and describes linear effects such as index of refraction and absorption coefficient of the material. The second order susceptibility is responsible for nonlinear effects such as second harmonic generation, sum frequency generation, difference frequency generation, and optical rectification. Some of these effects are described in more detail in later sections in the context of THz generation and detection. However, in the context of silica based optical fibers, we neglect this term due to the inversion symmetry in silica. For centrosymmetric media, such as silica, $\chi^{(2)} = 0$ and third order nonlinearities are therefore the lowest order nonlinear effects considered. In most cases, the dominant nonlinear effect in silica fibers, a $\chi^{(3)}$ effect, is a result of the intensity dependent refractive

index (n_2)

$$n = n_0 + n_2 I = n_0 + \bar{n}_2 |\vec{E}|^2 \tag{2.8}$$

where I is the peak intensity of the optical field. We can derive the nonlinear refractive index in a rather straightforward manner. In the frequency domain, we begin with the total polarization of the material at a frequency ω

$$\vec{P}_{total}(\omega) = \varepsilon_0 \Big(\chi^{(1)} \vec{E}(\omega) + 3\chi^{(3)} |\vec{E}(\omega)|^2 \vec{E}(\omega) \Big) = \varepsilon_0 \chi_{eff} \vec{E}(\omega) \tag{2.9}$$

where the factor of 3 accounts for degeneracy in this specific nonlinear process. In general,

$$n^2 = 1 + \chi_{eff}. \tag{2.10}$$

Substituting equations 2.8 and 2.9 into equation 2.10 we obtain

$$\Big(n_0(\omega) + 2\bar{n}_2 |\vec{E}(\omega)| \Big)^2 = 1 + \chi^{(1)} + 3\chi^{(3)} |\vec{E}(\omega)|^2 \tag{2.11}$$

$$n_0(\omega)^2 + 4 n_0 \bar{n}_2 |\vec{E}(\omega)|^2 = 1 + \chi^{(1)} + 3\chi^{(3)} |\vec{E}(\omega)|^2 \tag{2.12}$$

Note that we have neglected terms on the order of $|\vec{E}(\omega)|^4$. Equating terms, we find that $n_0(\omega) = \sqrt{1 + \chi^{(1)}}$, as is usually the case, and $\bar{n}_2 = 3\chi^{(3)}/4n_0$. Thus, third order nonlinear effects can be accessed by either pumping a material with an extremely large optical field, or, modestly pumping a material with high $\chi^{(3)}$ coefficient.

A consequence of the intensity-dependent refractive index is an intensity-dependent phase

$$\phi = n k_0 L = \Big(n_0 + n_2 I \Big) \frac{2\pi}{\lambda} L = \phi_L + \phi_{NL}(I) \tag{2.13}$$

where L is the fiber length and ϕ_L is the linear phase. The nonlinear phase shift, ϕ_{NL}, is known as self-phase modulation (SPM), which is properly name as it is a phase shift of a pulse induced by its own optical field. This nonlinear effect is responsible for the generation of new frequencies and is utilized to overcome spectral bandwidth limitations of the sources used in the THz systems described in chapters 4 and 5.

It is important to note that the temporal profile of an ultrashort pulse is not infinitely narrow, like a Dirac delta function, or uniform over a certain width, like a top-hot function. Laser sources often have pulses with Gaussian temporal shapes. Thus, we can include a time-dependence on the SPM-induced phase shift

$$\phi_{SPM}(t) = n_2 I(t) k_0 L \tag{2.14}$$

where $I(t)$ is the Gaussian profile of the pulse in the time domain. SPM-induced phase shift therefore also has a Gaussian profile, with the maximum phase shift occurring at the center of the pulse, as depicted in Fig. 2.5a. This time-dependent phase shift is the reason SPM results in spectral broadening, as the instantaneous frequency varies across the pulse. The instantaneous frequency is defined as the negative of the time derivative of the phase. The SPM-induced instantaneous frequency is thus determined by the derivative of the temporal profile of the pulse such that

$$\delta\omega_{SPM} = -\frac{d\phi_{SPM}}{dt}. \tag{2.15}$$

For Gaussian pulses, the symmetry of the temporal profile therefore results in symmetric spectral broadening since the rising and falling edges of the pulse have the same slope; the rising edge contributing red shift and the falling edge contributing blue shift to the spectrum.

The instantaneous frequency of a Gaussian pulse is shown in Fig. 2.5b, highlighting the symmetry in phase shift about the center of the pulse. Another consequence of this effect is that shorter pulses, whose rising and falling edges (leading and trailing edges, respec-

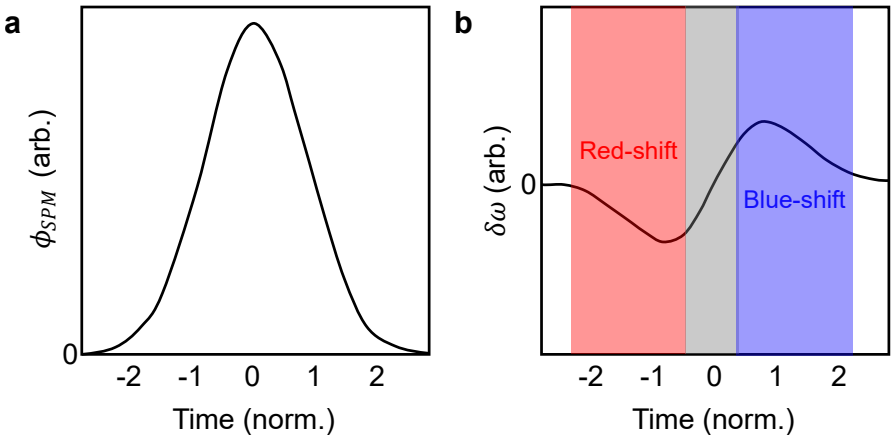

Figure 2.5: a) SPM-induced phase shift and b) corresponding instantaneous frequency of a Gaussian pulse plotted as a function of time normalized by the pulse duration. Negative $\delta\omega$ corresponds to a red-shift (red shaded area) and positive $\delta\omega$ corresponds to a blue-shift (blue shaded area) in the spectrum. The grey shaded area represents the portion of the pulse experiencing linear up-chirp. Figure adapted from [4].

tively) are steeper than longer pulses, experience more significant spectral broadening. The central region of the pulse, where the instantaneous frequency increases with time, produces an SPM-induced chirp, which is always positive for Gaussian pulses. Pulses with more complex temporal profiles, for example pulses that possess higher order dispersion, therefore experience more erratic spectral broadening as they propagate in the fiber. However, we limit our discussion to Fourier transform limited Gaussian pulses, $\Delta\omega\Delta\tau = 0.88\pi$ where $\Delta\omega$ and $\Delta\tau$ are spectral and temporal width at full-width half-maximum (FWHM), respectively, as other situations do not apply to the results contained in this thesis.

Although this section has solely focused on SPM so far, in reality, there are numerous other nonlinear effects influencing pulse propagation in a fiber. For instance, self-steepening is another outcome of the nonlinear refractive index. Here, the nonlinear refractive index causes the most intense portion of the pulse to experience a higher refractive index and therefore travel slower than the leading edge, breaking the symmetry of an initially Gaussian pulse and consequently breaking the symmetry of SPM-induced spectral broadening. We will not describe every nonlinear effect a pulse may experience in an optical fiber, but instead describe those that are pertinent to this thesis.

In general, the wave equation describing pulse propagation in the fiber is determined by solving Maxwell's equations while considering linear and nonlinear effects. If we are only to consider the lowest order nonlinearities in silica and neglect higher order dispersion, the wave equation takes the form

$$\frac{\partial}{\partial z}A + \beta_1\frac{\partial}{\partial t}A + \frac{i\beta_2}{2}\frac{\partial^2}{\partial t^2}A + \frac{\alpha}{2}A = i\gamma|A|^2A \tag{2.16}$$

where A is the pulse envelope, α is the absorption coefficient of the medium, and we have introduced the nonlinear parameter $\gamma = \omega_0 n_2\Big(cA_{eff}\Big)^{-1}$ where A_{eff} is the effective mode area [4]. The effective mode area is determined by fiber parameters, but largely dependent on the radius of the fiber core; tighter confinement leading to increased γ. Equation 2.16 ignored many higher order linear and nonlinear effects, which is a valid approach in the context of "long" optical pulses. However, when working with sub-picosecond pulses, some higher order linear and nonlinear terms like β_3 and intrapulse Raman scattering cannot be ignored [4]. In such a case, the nonlinear wave equation becomes

$$\frac{\partial}{\partial z}A + \frac{\alpha}{2}A + \beta_1\frac{\partial}{\partial T}A + \frac{i\beta_2}{2}\frac{\partial^2}{\partial T^2}A = i\gamma\Big(|A|^2A + \frac{i}{\omega_0}\frac{\partial}{\partial T}(|A|^2A) - T_RA\frac{\partial}{\partial T}|A|^2\Big) \tag{2.17}$$

where T_R is the first moment of the Raman response function of the fiber and we have shifted to a moving reference frame such that $T = t - \beta_1 z$ [4]. Although we now consider more terms in equation 2.17, we still neglect many others. For instance, we still neglect terms related to self-steepening, which will significantly affect spectral broadening.
Solving equation 2.17 is not a straightforward task. Attempting to solve the nonlinear wave equation analytically is only possible in particular situations, making a numerical solution the only viable method. The split-step Fourier method is a practical approach and is the method used to simulate nonlinear pulse propagation in the works found in chapter 5. It involves launching a Gaussian pulse into a fiber that is divided into alternating sections: one where only linear effects (left hand side of equation 2.17) are considered and one where only nonlinear effects (right hand side of equation 2.17) are considered, using the resulting pulse of preceding sections as the input for subsequent sections. The split-step Fourier method has proven to be a valid method for predicting pulse behavior in a fiber. However, if one truly wants an accurate model to predict pulse properties all linear and nonlinear effects must be considered, especially in extreme cases like supercontinuum generation.

2.1.3 Optical solitons and supercontinuum generation

The term *soliton* refers to waves which do not change as they propagate. In optics, they occur when linear and nonlinear effects cancel each other out during propagation, leaving the pulse unchanged as it propagates. Spatially, this occurs when self-focusing – a consequence of the intensity-dependent refractive index – balances out diffraction as the pulse propagates through a medium (or even in air). In fiber, however, the light is already confined to the core and spatial solitons are therefore irrelevant. On the other hand, temporal solitons are of great interest and occur when nonlinear dispersion balances out linear dispersion (GVD) of the fiber, allowing the pulse to propagate through the fiber without altering its duration. Since positive dispersion is induced during nonlinear spectral broadening (Fig. 2.5b), the light must travel in the anomalous dispersion regime of the fiber to allow for soliton formation. This is when it becomes beneficial to engineer the dispersion profile of a PCF. Shifting the anomalous regime of the fiber towards the wavelength of the laser source can promote soliton formation.

Let us introduce the soliton order parameter N [4], which states

$$N^2 = \frac{\gamma P_0 T_0^2}{|\beta_2|} \tag{2.18}$$

where γ is the nonlinear parameter of the fiber, P_0 is the peak power of the input pulse, and T_0 is the pulse duration. The fundamental soliton ($N = 1$) can therefore only form if $P_0 T_0^2 \geq |\beta_2|/\gamma$, setting constraints on the peak power and pulse duration required for soliton generation. With femtosecond sources, T_0 is miniscule and higher peak power is therefore required. Conversely, pulses of longer duration require lower peak powers for soliton formation. Another consequence of equation 2.18 is that in most situations, fiber specifications and pulse duration are fixed parameters and the peak power launched into the fiber is the only experimentally tunable setting determining the soliton order.

Raman solitons in optical fibers are a fascinating phenomenon that occurs due to the interplay between nonlinear effects, such as SPM and Raman scattering, and linear dispersion. Raman solitons are self-sustaining optical pulses that propagate without distortion over long distances in optical fibers, maintaining their shape and intensity profile. To understand the theoretical explanation of Raman solitons, let's consider a standard single-mode optical fiber with a core material characterized by a nonlinear refractive index and a dispersion profile.

The primary nonlinear effect involved in Raman soliton generation is stimulated Raman scattering (SRS), which is a result of an intense optical pulse interacting with the vibrational modes of the material, transferring energy to lower or higher frequency components through an inelastic scattering process. In the case of Raman solitons, the higher-frequency components of the pulse are downshifted, while the lower-frequency components are upshifted due to the Raman effect. The first crucial step in the formation of Raman solitons is SPM, keeping in mind that the high frequency components travel faster than the low frequency components in the fiber and that SPM induces up-chirp. As the pulse broadens due to SPM, the energy in the high-frequency components begins to overlap with the low-frequency components, resulting in efficient energy transfer through Raman scattering. The high-frequency components lose energy to the lower-frequency components through SRS, leading to the formation of solitons. This process is repeated along the entire fiber. The dispersion profile of the fiber also plays a crucial role in shaping the Raman solitons. In the anomalous dispersion regime, the high-frequency components of the pulse travel

faster than the low-frequency components. This effect counteracts the SPM-induced spectral broadening, helping to maintain the soliton's shape. Similarly, SPM-induced up-chirp counteracted by the anomalous dispersion of the fiber.
The input pulse parameters, such as duration, energy, and spectral profile, along with the fiber's dispersion and nonlinear properties, need to be appropriately tailored to achieve soliton propagation. The generation and dynamics of Raman solitons can be mathematically described by the nonlinear Schrödinger described in equation 2.17. Assuming fiber losses are negligible and $N = 1$, solving equation 2.17 allows us to predict the Raman-induced frequency shift relative to the pump wavelength after propagation through a fiber of length L such that

$$\Omega_R = -\frac{8T_R\gamma P_0}{15T_0^2}L = -\frac{8T_R|\beta_2|}{15T_0^2}L \tag{2.19}$$

First, we notice that the Raman soliton will always shift to lower frequencies (longer wavelengths) and that fiber length, input power, and pulse duration are experimentally tunable parameters to generate a Raman soliton at a desired wavelength.
Soliton dynamics govern the world of supercontinuum generation in fiber, even to broaden optical spectra towards shorter wavelengths relative to the optical pump. With the fission of a soliton, propagating in the anomalous dispersion regime, comes the generation of a dispersive wave, occasionally referred to as non-solitonic radiation, which has a frequency within the normal dispersion regime of the fiber having the same phase as the soliton responsible for its generation [47, 48]. Fission of N^{th}-order solitons generates N dispersive waves, all with slightly different wavelengths. Soliton-dispersive wave pairs can therefore generate supercontinua spanning multiple octaves, like the one described in chapter 6, covering both the normal and anomalous dispersion regimes of the fiber.

2.2 THz generation and detection in electro-optic crystals

Although there are several ways to generate and detect THz pulses, the methods used in this thesis rely on nonlinear effects in electro-optic crystals, i.e. crystals possessing high $\chi^{(2)}$ coefficients and low absorption at the central wavelength of the lasers used in this work (1030 nm and 1064 nm). These methods are specifically chosen since they allow for THz generation and detection over a relatively broad frequency range.

2.2.1 Optical rectification

To analytically describe the THz generation process, we rely on Maxwell's equations and the total polarization of the material exposed to intense optical fields in equation 2.7. Maxwell's equations in a dielectric are

$$\nabla \cdot \vec{E} = 0 \tag{2.20a}$$

$$\nabla \times \vec{E} = -\frac{\partial}{\partial t}\vec{B} \tag{2.20b}$$

$$\nabla \times \vec{B} = \mu_0 \varepsilon_0 \frac{\partial}{\partial t}\vec{E} + \mu_0 \frac{\partial}{\partial t}\vec{P} \tag{2.20c}$$

$$\nabla \cdot \vec{B} = 0 \tag{2.20d}$$

where μ_0 is the magnetic susceptibility and $\vec{B}$ is the magnetic field vector. Taking the curl of equation 2.20b and using the relation $\nabla \times (\nabla \times \vec{E}) = \nabla(\nabla \cdot \vec{E}) - \nabla^2 \vec{E}$ we find

$$\nabla \times (\nabla \times \vec{E}) = -\frac{\partial}{\partial t}(\nabla \times \vec{B}) \tag{2.21}$$

$$\nabla(\nabla \cdot \vec{E}) - \nabla^2 \vec{E} = -\frac{1}{c^2}\frac{\partial^2}{\partial t^2}\left(\vec{E} + \frac{\vec{P}}{\varepsilon_0}\right) \tag{2.22}$$

$$\nabla^2 \vec{E} - \frac{1}{c^2}\frac{\partial^2}{\partial t^2}\vec{E} = \frac{1}{\varepsilon_0 c^2}\frac{\partial^2}{\partial t^2}\vec{P} \tag{2.23}$$

where we have substituted equation 2.20a into equation 2.22. Inserting the expanded polarization of the material from equation 2.7 yields

$$\nabla^2 \vec{E} - \frac{n_0^2}{c^2}\frac{\partial^2}{\partial t^2}\vec{E} = \frac{1}{\varepsilon_0 c^2}\frac{\partial^2}{\partial t^2}\vec{P}^{NL} \tag{2.24}$$

which utilizes the fact that the linear refractive index of the material is associated to the first order susceptibility of the material such that $n_0^2 = 1 + \chi^{(1)}$. Equation 2.24 is known as the nonlinear wave equation in bulk material. When solving the nonlinear wave equation, one can simply replace $\vec{P}^{NL}$ with the nonlinear term of their choice from equation 2.7 and the appropriate degeneracy coefficient [46]. For example, for optical rectification $P^{NL} = 2\varepsilon_0\chi^{(2)}\vec{E}\vec{E}^*$ and for second harmonic generation $P^{NL} = \frac{1}{4}\varepsilon_0\chi^{(2)}\vec{E}\vec{E}$. Here, we assume that the medium is lossless and dispersionless such that $\vec{P}$ and $\vec{E}$ are scalar quantities and $\vec{P}$ depends only on the instantaneous electric field strength [46]. With the nonlinear wave equation described in equation 2.24, we can describe unique nonlinear optical processes. We assume that the electric field is of the form $E_i = A_i(z)e^{i(k_i z - \omega_i t)}$, where $A(z)$ is the amplitude of the field that is changing as a function of the propagation direction z, $k_i = n_i\omega_i/c$ (analogous to β_0 in section 2.1.1), and the subscript i represents specific frequency components of the electric field. The nonlinear wave equation describing generation of a

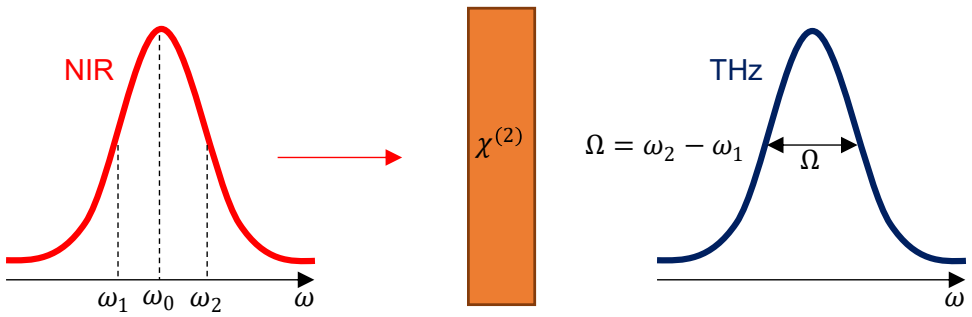

Figure 2.6: Schematic representation of THz generation in a $\chi^{(2)}$ crystal via optical rectification. An ultrashort NIR pulse (red) centered at a frequency ω_0 is focused into the nonlinear crystal to produce a THz pulse (blue). The frequency components contained in the NIR pulse are used for frequency mixing in the crystal. The spectral bandwidth of the NIR pulse determines the spectral bandwidth of the generated THz pulse, provided that phase matching conditions are satisfied.

single THz frequency $\Omega = \omega_2 - \omega_1$ via optical rectification, depicted in Fig. 2.6, becomes

$$\nabla^2 \vec{E}_\Omega - \frac{n_0^2}{c^2}\frac{\partial^2}{\partial t^2}\vec{E}_\Omega = \frac{2\chi^{(2)}}{c^2}\frac{\partial^2}{\partial t^2}\vec{E}_2\vec{E}_1^*. \tag{2.25}$$

Since the pulse is chosen to propagate along a single direction (z), $\nabla^2 = (\partial/\partial z)^2$. Performing the derivatives in equation 2.25,

$$\Big(2ik_\Omega\frac{\partial}{\partial z}A_\Omega + \frac{\partial^2}{\partial z^2}A_\Omega\Big)e^{i(k_\Omega z - \Omega t)} = -\frac{2(\omega_2-\omega_1)^2\chi^{(2)}}{c^2}A_2A_1^*e^{i((k_2-k_1)z-(\omega_2-\omega_1)t)} \tag{2.26}$$

Here, we adopt the slowly varying amplitude approximation such that $\frac{\partial^2}{\partial z^2}A_\Omega = 0$ as its magnitude is significantly smaller than the other term on the left-hand side of equation 2.26, which becomes

$$2ik_\Omega\Big(\frac{\partial}{\partial z}A_\Omega\Big)e^{ik_\Omega z} = -\frac{2\Omega^2\chi^{(2)}}{c^2}A_2A_1^*e^{i((k_2-k_1)z} \tag{2.27}$$

$$\frac{\partial}{\partial z}A_\Omega = \frac{i\Omega^2\chi^{(2)}}{k_\Omega c^2}e^{i\Delta k z} \tag{2.28}$$

where we have introduced $\Delta k = k_2 - k_1 - k_\Omega$ which represents the wavevector mismatch between NIR and THz waves propagating in the crystal. Integrating equation 2.28 over the length of the nonlinear medium (the crystal in this case) will yield the amplitude of the THz field. A consequence of generating THz pulses in this manner is that the spectral bandwidth of NIR pulse used for optical rectification determines the maximum attainable THz bandwidth. Ultrashort NIR pulses up to a time duration of 200 fs become ideal for this process as their spectral bandwidth span a few THz and, depending on the source itself, can reach bandwidths on the order of tens of THz to achieve extremely broadband THz generation. However, the wavevector mismatch becomes especially important to consider when attempting to produce broadband THz radiation.

In the case of perfect phase matching, $\Delta k = 0$ and can therefore be rewritten such that $k_\Omega = k_2 - k_1$ and $n_\Omega\Omega = n_2\omega_2 - n_1\omega_1$. In other words, the phase velocity of the THz wave must match the group velocity of the NIR pulse to achieve perfect phase matching. Thus, phase matching can be achieved by choosing the appropriate nonlinear crystal based on the wavelength of the ultrafast source available. The optimal phase matching wavelength for various nonlinear crystals used for THz generation is shown in Table 2.1. Here, the optimal phase matching wavelength corresponds to the wavelength at which n_g is approximately equal to the square root of the relative dielectric constant of the crystal [5, 49].

One may take advantage of birefringent materials with high $\chi^{(2)}$ coefficients to achieve phase matching over broad frequency ranges. This is done by taking advantage of the material's ordinary and extraordinary refractive indices by tuning the angle of the crystal. For instance, gallium selenide (GaSe) is a popular nonlinear crystal for achieving phase matching in such a manner and is discussed in a later chapter.

When choosing an appropriate nonlinear crystal for a THz system, the thickness of the crystals is also an important parameter to consider. If we are to integrate equation 2.28 under the undepleted pump approximation, that is, A_2 and A_1^* are treated as constants throughout a crystal of length L, we find

$$A_\Omega(L) = \frac{i\Omega^2\chi^{(2)}}{k_\Omega c^2} A_2 A_1^* \int_0^L e^{i\Delta k z} dz = \frac{\Omega^2\chi^{(2)}}{k_\Omega c^2} A_2 A_1^* \frac{e^{i\Delta k L} - 1}{\Delta k} \tag{2.29}$$

which means the generated THz field should increase as it propagates through the crystal. The intensity of the generated THz field is therefore

$$I_\Omega \propto |A_\Omega|^2 \propto \left| \frac{e^{i\Delta k L} - 1}{\Delta k} \right|^2 = L^2 \left(\frac{e^{i\Delta k L} - 1}{\Delta k L} \right) \left(\frac{e^{-i\Delta k L} - 1}{\Delta k L} \right) \tag{2.30a}$$

$$I_\Omega \propto L^2 \frac{2 - 2\cos(\Delta k L)}{\Delta k L} = L^2 \frac{\sin^2(\Delta k L/2)}{(\Delta k L/2)} \tag{2.30b}$$

$$I_\Omega \propto L^2 sinc^2 \left(\frac{\Delta k L}{2} \right) \tag{2.30c}$$

However, this is not necessarily the case for all frequency components of the THz field. The coherence length is often a parameter that is useful for determining the maximum THz bandwidth where $L_{coh} \propto (\Delta k)^{-1}$. This parameter determines the coherent buildup length of the nonlinear interaction. Each of the generated THz frequency components will have a unique wavevector mismatch associated to them. Lower THz frequencies (1-3 THz) often have more attainable phase matching conditions and therefore have inherently longer coherence lengths in comparison to higher THz frequencies (>3 THz). Satisfying phase

Table 2.1: NIR wavelength leading to phase matched generation of 1 THz by optical rectification in various nonlinear crystals [5].

	ZnS	**ZnTe**	**GaP**	**InP**	**GaAs**
Phase matching wavelength (nm)	470	822	1030	1230	1405

matching conditions over a frequency range spanning several optical octaves in the THz regime is a challenge that can therefore accomplished by using thin nonlinear crystals. A common theme throughout this thesis is that one must sacrifice THz field strength by using thin nonlinear crystals to achieve broadband THz generation. This theme, however, also applies to THz detection through electro-optic sampling.

2.2.2 Electro-optic sampling of THz waveforms

Accessing the frequency content of a THz pulse is not as straightforward as in the visible or NIR regimes, where gratings and detector arrays can be used to extract spectral information. The THz band does not have this luxury. Detecting optical power in the THz regime often relies on bolometers and Golay cells, which do not take the frequency of the light into consideration. An array of these types of detectors, which could be used to extract frequency content, is an expensive and impractical approach to accessing the THz spectrum. The method of electro-optic sampling (EOS), which relies on a different $\chi^{(2)}$ nonlinear process, was introduced to retrieve the frequency content of a THz field and has become a standard technique in THz spectroscopy [50, 51].

A standard EOS experimental configuration relying on balanced detection is depicted in Fig. 2.7. First, let's consider the case where there is no THz field incident on the crystal, as shown in Fig. 2.7a. A weak linearly polarized NIR femtosecond pulse is incident on a second-order nonlinear crystal, identical to the type of nonlinear crystal described in the previous section. After propagation through the crystal, the polarization state of the NIR pulse is unchanged. The pulse is then transmitted through a quarter-wave plate whose orientation is aligned to produce circularly polarized light. A Wollaston prism spatially separates the two orthogonal polarization components of the circularly polarized light, whose respective intensities are measured with (reasonably) identical detectors. Without a THz field present, these detectors will measure the same intensities and their voltage difference (ΔD) is therefore zero. In the situation where a THz field is also incident on the detection crystal, as illustrated in Fig. 2.7b, the THz field induces a birefringence on the crystal. Through the Pockels effect, the polarization of the NIR pulse is rotated, yielding elliptical polarization after propagation through the quarter-wave plate and $\Delta D \neq 0$. Since the THz pulse oscillates on the order of a few picoseconds and the NIR pulse duration is

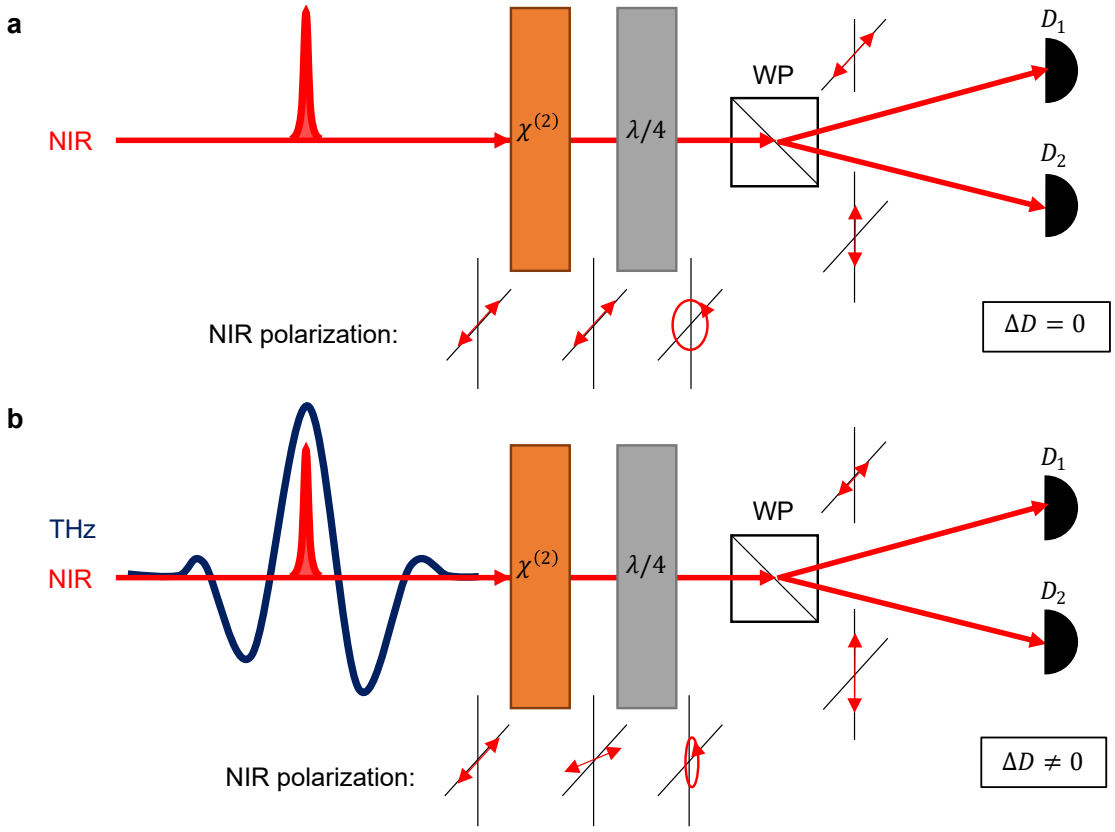

Figure 2.7: Schematic representation of an electro-optic sampling scheme. a) A linearly polarized femtosecond NIR pulse is transmitted through a $\chi^{(2)}$ crystal. Without a THz field present, the polarization state is unchanged after propagation through the crystal. A quarter-wave plate ($\lambda/4$) produces circularly polarized light and a Wollaston prism (WP) spatially separates the orthogonal polarization components of the light. The intensity of the orthogonal polarization components are measured by individual detectors (D_1 and D_2), whose voltage difference (ΔD) is zero. b) The same scheme as described in a) but with a THz pulse spatially and temporally overlapped with the NIR in the crystal. The birefringence induced by the THz field induces a change in polarization on the NIR pulse, rendering $\Delta D \neq 0$. The process is repeated for several time delays to map out the electric field of the THz pulse one data point at a time.

presumably on the order of 100-200 fs, the NIR pulse probes only the fraction of the THz field corresponding to the temporal overlap. The Pockels effect is linear with the THz electric field through a second-order nonlinear process driven by the $\chi^{(2)}$ coefficient described in equation 2.7, where the local THz electric field is treated as a DC field [52, 53]. The strength of the polarization rotation, and hence ΔD, are directly related to the strength of the THz field at a given relative delay between the NIR detection pulse and the THz pulse. In fact, this detection technique is sensitive to the direction of the THz field, or in other words, the phase retardation induced by the THz field. For example, if a positive THz field causes a polarization rotation to the right and $\Delta D > 0$, a negative THz field will cause a polarization rotation to the left and $\Delta D < 0$. This phase retardation is quantified by

$$\Delta\varphi = \frac{\omega L}{c} n_0^3 r_{41} E_\Omega \tag{2.31}$$

where L is the nonlinear interaction length in the crystal, n_0 is the refractive index of the crystal at NIR probing wavelength, r_{41} is the electro-optic coefficient (associated with $\chi^{(2)}$ of the crystal), and E_Ω is the strength of the THz field at a given temporal overlap [54]. Repeating this process for all relevant time delays, controlled by a mechanical delay stage not pictured in Fig. 2.7, results in the retrieval of the THz electric field and the frequency content of the THz pulse is extracted with a fast Fourier transform.

Retrieving THz fields with EOS is a powerful and reliable technique as it provides both amplitude and phase information of a THz pulse. As we will see in a later section, recording a THz waveform in this manner after the pulse has been transmitted through a material allows for the complex dielectric function of the material to be extracted without relying on Kramers-Kronig relations. This technique, however, also has its drawbacks:

1. It is subject to the same phase matching conditions as optical rectification. A broadband detection window is therefore only accessible with thin nonlinear crystals, sacrificing signal strength and thereby sacrificing signal-to-noise ratio.

2. To reduce background noise in the measurement, the photodiodes are connected to a lock-in amplifier and each data point requires a waiting time 5× the integration time of the lock-in amplifier for each data point. The data acquisition time is therefore on the order of minutes. In terms of spectroscopy, this limits the extractable information of a sample. If the sample under investigation is changing as a function of time, the

measurement may only extract dynamics that are slower than the data acquisition time. Resolving fast changes in a sample therefore requires a faster THz detection technique.

2.2.3 Chirped-pulse spectral encoding and photonic time-stretch

The ability to quickly record a THz waveform allows more information to be extracted from a series of measurements. To achieve this, one could simply rely on a sophisticated delay stage and relatively fast diodes in their THz system, rapidly varying the relatively delay between NIR and THz pulses and continuously recording ΔD as the stage oscillates. Fast delay stages have been achieved relying on acousto-optic filters [55], rotating helical mirrors [56], and shaker delay lines [57]. These techniques have pushed EOS to record waveforms at a rate of tens of kHz. Recording a THz waveform in a single shot, however, grants access to even more information as it does not have to rely on averaging over many laser pulses to retrieve the THz field. Of the many single-shot THz detection methods [58, 59, 60, 61, 62, 63], chirped-pulse spectral encoding (CPSE) is one of the more straightforward single-shot detection methods to implement into existing THz systems. The concept of CPSE is shown in Fig. 2.8. Here, instead of relying on femtosecond, Fourier transform limited NIR detection pulses at various time delays to probe the THz field, a NIR supercontinuum (SC) chirped to a duration longer than that of the THz waveform is used for detection. The spectral components of the SC, separated in time, probe the THz field as they propagate in a $\chi^{(2)}$ crystal. The THz waveform imprints itself on the spectrum of the chirped SC. Thus, a spectrometer operating in the NIR may be used to record both supercontinua, the unmodulated SC and the THz-encoded SC. Subtracting the unmodulated SC from that of the THz-encoded SC and a simple frequency-to-time calibration yields the THz waveform information. Resolving the THz field in this manner also has its drawbacks. With EOS, the temporal resolution of the measurement is largely dependent on the duration of the NIR pulse used for detection and the step size of the delay stage. With CPSE, the temporal resolution, δt, is related to the spectral bandwidth of the SC and the amount of chirp applied to the pulse such that

$$\delta t = \sqrt{\tau_0 \tau_C} \tag{2.32}$$

where τ_0 is the duration of the SC in the Fourier transform limited case ($\tau_0 = 0.88\pi/\Delta\omega$ for Gaussian pulses) and τ_C is the duration of the chirped SC [64, 65]. Consequently, increasing the duration of the chirped SC, increasing the temporal window, and a spectrally narrow SC degrade the temporal resolution of the measurement, a parameter that is crucial for resolving high THz frequencies. Finding a balance between spectral bandwidth and chirp is therefore required for detecting THz pulses in this manner, but can be overcome with more sophisticated versions of the technique like diversity EOS [66].

Although resolving the THz waveform with CPSE and a spectrometer is significantly faster than standard EOS, it is still intrinsically limited as the diode arrays of USB spectrometers often require integration times over 1 ms. Thus, if one was to perform time-resolved THz spectroscopy with the CPSE detection method, they would be limited to millisecond dynamics. This is still a massive improvement over standard EOS, and has even reduced the data required acquisition time by a factor of 160 using a 1 kHz system [67]. However, the limitations imposed by the electronics used to record the NIR spectra provide an unwanted ceiling to the technique. Introducing a photonic time-stretch technique to CPSE removes this ceiling and allows for THz detection at arbitrarily fast rates with single pulse resolution.

In theory, we should be able to resolve a chirped SC with a diode since the spectrum changes as a function of time. However, if we were to shine the THz-encoded SC on a

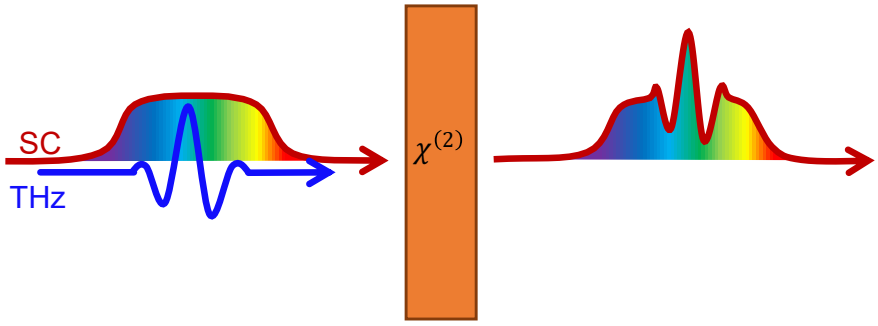

Figure 2.8: Schematic representation of CPSE. A NIR supercontinuum (SC) is temporally and spatially overlapped with a THz pulse in a $\chi^{(2)}$ crystal. The frequency components of the SC probe the THz waveform at different delays, resulting in the THz waveform being imprinted on the spectrum of the SC.

high-end diode, since the pulse duration is on the order of picoseconds, the pulse is still too short to resolve the spectrum as current electronics are still too slow to resolve changes in signal at these speeds. The photonic time-stretch technique utilizes GVD in a standard optical fiber to spread out the frequency components of the SC in time, into the nanosecond regime, such that the signal varies slow enough to be sampled with a high-speed photodiode and sophisticated oscilloscope [68]. Provided that the oscilloscope is properly triggered, mapping the SC spectrum to the time domain in this manner allows for every single pulse from a pulse train to be resolved at even MHz rates. Performing THz spectroscopy at such unprecedented rates allows for the complex dielectric function of a material to be extracted at sub-millisecond and potentially even sub-microsecond timescales. This concept is at the core of the work presented in chapter 4.

2.2.4 THz time-domain spectroscopy parameter retrieval

When performing optical spectroscopy, the light that is transmitted through or reflected from the surface of a material is investigated and compared to the light from the source. In the NIR regime, this is performed with a simple USB spectrometer by measuring the spectrum before and after the sample under study, providing information on the absorption spectrum of the sample within the spectral bandwidth of the source. The frequency dependent complex refractive index of a material is

$$\tilde{n}(\omega) = n_s(\omega) - i\kappa_s(\omega) \tag{2.33}$$

where n_s (not to be confused with the index of the slow axis of a fiber in section 2.1.1) is the linear refractive index and κ_s is the extinction coefficient of the sample. The absorption of the material is related to the complex part of the refractive index through

$$\alpha_s(\omega) = \frac{2\omega\kappa_s(\omega)}{c} \tag{2.34}$$

Thus, measuring the spectrum transmitted through a material only provides information on the complex part of the refractive index and no information on the real part n_s. The real part requires phase information and is directly measured with the THz detection techniques described in previous sections.

The THz field in the frequency domain transmitted through a material can be expressed as

$$E_s(\omega) = \frac{4\tilde{n}_s}{(\tilde{n}_s+1)^2} e^{-i\tilde{n}_s\omega L/c} E_0(\omega) \tag{2.35}$$

where E_0 is the incident wave and L is the thickness of the sample under investigation. The reference measurement, i.e. the THz field travelling through the same system but without the sample in the THz path is

$$E_{ref}(\omega) = e^{-i\omega L/c} E_0(\omega) \tag{2.36}$$

Experimentally, $E_s(\omega)$ and $E_{ref}(\omega)$ are obtained by calculating the Fourier transform of the recorded THz waveform. Normalizing the transmitted THz spectrum by the reference spectrum provides us with a transfer function

$$H(\omega) = \frac{E_s(\omega)}{E_{ref}(\omega)} = \frac{4n_s}{(n_s+1)^2} e^{-\kappa_s\omega L/c} e^{-i(n_s-1)\omega L/c} \tag{2.37}$$

Equating the real parts and taking the logarithm we obtain

$$\ln(H(\omega)) = \ln\left(\frac{4n_s}{(n_s+1)^2}\right) - \kappa_s\frac{\omega L}{c} \tag{2.38}$$

and can rearrange the result to extract the absorption coefficient of the material

$$\alpha(\omega) = \frac{2\omega\kappa_s(\omega)}{c} = \frac{2}{L}\left(\ln\left(\frac{4n_s}{(n_s+1)^2}\right) - \ln\Big(H(\omega)\Big)\right) \tag{2.39}$$

As for the imaginary part in equation 2.37, we require the phase of the transfer function that is directly related to the phase of the reference and transmitted signals. We find that

$$\arg\Big(H(\omega)\Big) = -\left(\frac{n_s\omega L}{c} - \frac{\omega L}{c}\right) = -(\phi_s - \phi_{ref}) = -\Delta\phi \tag{2.40}$$

Since we directly measure the phase and can extract with simple programming functions, we can extract the refractive index of the material without performing any extra measurements. Rearranging equation 2.40 we find

$$n_s = \frac{\Delta\phi c}{\omega L} + 1 \tag{2.41}$$

The ability to directly characterize the complex refractive index of a material has many positive consequences. The complex dielectric function of a material, defined as

$$\tilde{\epsilon}_s = \tilde{n}_s^2 = (n_s + i\kappa)^2 \tag{2.42}$$

can therefore be extracted as well and, if applicable, can quantify electrical properties of a material with the Drude model [69]. This method of material parameter is valid assuming that the following is true [70]:

1. The sample is homogeneous along the direction of propagation of the THz wave.
2. The THz wave incident on the sample is at normal incidence.
3. The sample has flat and parallel surfaces.
4. The experimental setup is purged of water vapor to avoid complexity due to water vapor absorption.

In this work, the samples under investigation are thick enough such that their thickness can be accurately measured with a caliper. Thus, the thickness of the sample L is also assumed to be known and does not need to be extracted with the time delay between Fabry-Pérot reflections within the sample [71].

Chapter 3

Experimental details

3.1 Amplified laser

The majority of the work in this thesis relies on the same ultrafast laser source: a PHAROS laser from Light Conversion utilizing Yb:KGW as a gain medium. This laser delivers pulses with a 180 fs duration (FWHM) centered at a wavelength of 1030 nm, has a maximum average power of 6 W, and allows us to choose a pulse repetition rate between 6 kHz and 1.1 MHz via software. Consequently, the output pulse energy of the laser is tunable between 5.5 μJ and 1 mJ, corresponding to repetition rates of 1.1 MHz and 6 kHz, respectively, without considerably altering the pointing of the beam out of the laser. As we will see in later chapters, sacrificing pulse energy to achieve higher repetition rates can be a nuisance in some situations, like single-pulse THz detection, but can be advantageous when detecting THz waveforms with standard detection methods that rely on averaging, like EOS. The time duration of the PHAROS NIR pulse is measured with an intensity autocorrelator relying on a BBO crystal [72], and the spectrum is measured with a standard USB spectrometer.

The autocorrelation trace, shown in Fig. 3.1a, yields a pulse width of 255 fs (FWHM) and corresponds to a duration of 180 fs after applying the deconvolution factor of $\sqrt{2}/2$ [73]. The spectral width (shown in Fig. 3.1b) is ∼12 nm, or 3.5 THz in frequency, meaning this laser almost has the appropriate specifications for broadband THz generation and detection via optical rectification and EOS, respectively. The pulse is also characterized by means of

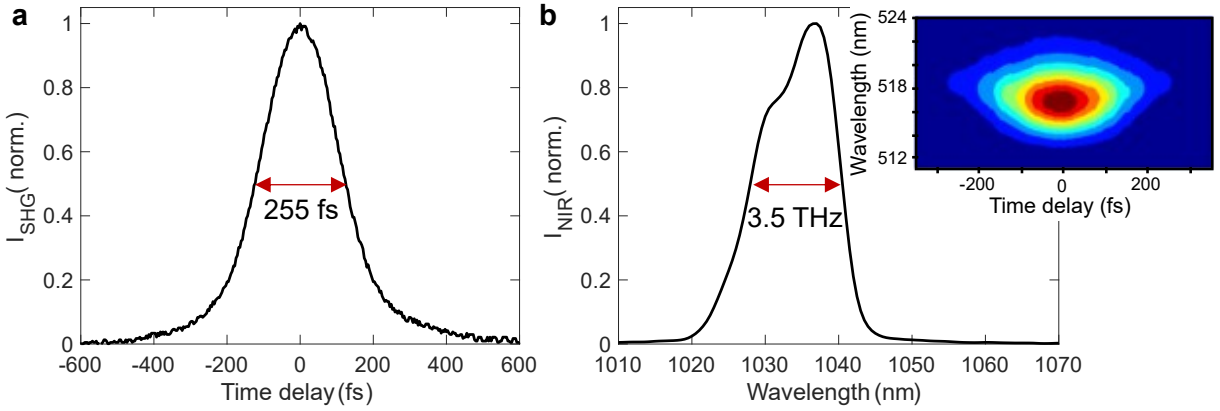

Figure 3.1: a) Temporal and b) spectral profiles of the amplified output of the laser used throughout this work. Temporal and spectral widths (FWHM) are indicated by red arrows. After considering deconvolution of the autocorrelation trace in a), the pulse duration is 180 fs (FWHM) and the spectral width is 3.5 THz (FWHM). A measured FROG spectrogram (inset) shows that the laser output is near transform-limited.

frequency-resolved optical gating (FROG), whose experimental configuration is identical to that of an intensity autocorrelator except that the second harmonic is resolved by a spectrometer instead of a photodiode. The spectrogram of the laser's output pulse, which displays the spectrum of the second harmonic signal as a function of relative delay, is shown in the inset of Fig. 3.1b and indicates that the pulse is near transform-limited [74, 75, 76].

3.2 Fiber coupling

Although it may seem relatively straightforward, there are many factors to consider when attempting to couple light into an optical fiber. First, the light must be focused to a smaller spot size than the core of the fiber and follow a trajectory within the acceptance cone of the fiber. The acceptance cone of the fiber is determined by the numerical aperture (NA) such that $NA = \sin(\theta)$ where θ is the angle of acceptance about the optical axis. This constraint requires that an aspheric lens, to minimize spherical aberrations, with an appropriate focal length be chosen while also considering the size of the beam before the

lens. Due to the Gaussian spatial profile of laser pulses, the spot size at the focus follows the equation

$$w_0 = \frac{4\lambda F}{\pi D} \tag{3.1}$$

where w_0 is the diameter of the beam at the focal point, F is the focal length of the lens, and D is the diameter of the beam incident on the lens. Measuring the beam diameter before the lens used to couple light into the fiber becomes crucial, as Gaussian beams diverge as they propagate. Another factor to consider is the direction of propagation of the pulse. Not only must the pulse be focused on the core of the fiber, its propagation direction must also match the orientation of the fiber core over the first few centimeters of fiber.

To facilitate alignment into the fiber, we utilize the grid of the optical table as a reference and a pair of irises whose heights are set to the height of the fiber. The irises are mounted along one of the grid lines of the optical table with sufficient distance between them in order to maximize beam pointing accuracy. The beam is aligned through the irises by adjusting the angle of two mirrors placed before them and maximizing power transmitted through both partially closed irises. Aligning the beam in this manner ensures that the central (most intense) portion of the Gaussian beam is aligned to the center of the fiber core. An aspheric lens, with its flat side facing where the fiber tip will be, is then placed in the beam path, ensuring that the center of the beam is incident on the center of the lens by monitoring the path of the back reflection. Finally, the fiber is mounted on a three-dimensional stage and placed after the lens along the same gridline as the initial irises. The transmitted power is monitored as the position of the input facet of the fiber is optimized for maximum optical throughput. Once the coupling efficiency is maximized, the output facet of the fiber is also mounted on a three-dimensional stage and a lens is placed after it to collimate the transmitted light. Depending on the fiber in question, this lens may have to be achromatic over a large spectral bandwidth or replaced by an off-axis parabolic (OAP) mirror to avoid spatial chirp.

3.3 Standard THz time-domain spectrometer

It is worth describing each component of a standard THz system that relies on nonlinear crystals for THz generation and detection and an EOS scheme to reconstruct the THz waveform. As shown in Fig. 3.2, a linearly polarized pulse from a femtosecond laser source (as described in section 3.1) is split into two paths by a beamsplitter (dashed black line): a generation (Gen.) line and a detection (Det.) line. Most of the optical power is used for THz generation (usually ∼90%) and the remainder is used for detection. The pulse used for generation is focused into a nonlinear crystal to generate a THz pulse via optical rectification (see section 2.2.1). The THz field is collimated and focused using OAP mirrors, creating focal points to investigate a sample and onto a detection crystal (Det.) for THz detection via EOS. Though the use of transmission optics, like lenses, to collimate and focus the THz radiation are more straightforward and simpler to align, reflective optics are chosen to avoid losing light at interfaces due to Fresnel reflection and echoes of the main THz pulses due to internal reflections within the transmissive optics. These echoes limit the temporal window of the time-resolved measurement and thereby limit the achievable frequency resolution of the system, which relies on the Fourier transform of the time-domain signal.

The orientation of the OAPs is crucial and great care is taken in their alignment. First and foremost, the beam height for the entire system is set to height of the center of the OAPs, which are all fixed on identical optical mounts. The distance between the center of the first OAP and the generation crystal is vital for collimating the THz emitted from the generation crystal, and the OAP must be oriented such that the beam keeps its Gaussian spatial profile in the far-field. Initial alignment of the OAPs takes advantage of the fact that reflective optics will behave similarly at visible and THz frequencies. The femtosecond source is blocked, and its beam path is mimicked by a laser diode operating in the visible regime and the generation crystal is replaced by a pinhole, creating quickly diverging diffractions rings. This diffraction pattern makes it easier to recognize deviations in beam shape in the far-field after the beam is collected by the first OAP. The grid of the optical table is used as a reference to ensure the beam is reflected 90 degrees from the incident beam. Fine adjustments are made to the position and orientation of the OAP such that the diffraction pattern is collimated over a long distance (at least a few meters) and in the proper direction. One-by-one the ensuing OAPs are placed into the beam path, ensuring

that the focal points are as Gaussian as possible and at the correct height, and the beam is properly collimated where applicable.

To remove the NIR beam leaking through the generation crystal, a germanium (Ge) wafer is placed in the beam path and acts as a spectral filter. Here, we take advantage of the band gap of germanium (0.67 eV at room temperature [77]) to block the incoming NIR light through the THz path and transmitting approximately 40% of the THz radiation through the wafer due to Fresnel reflection on both sides of the wafer ($n_{Ge}(\nu = 1\ \text{THz}) \approx 4$ [78, 79]).

The detection line (Det. line) consists of a delay stage with retroreflector to mechanically adjust the delay between the THz pulse and NIR detection pulse, and a lens to focus the beam onto the detection crystal, spatially and temporally overlapping the pulses in the crystal. Polarization optics after the crystal and the delay stage work together to reconstruct the THz waveform one data point at-a-time as described in section 2.2.2. Often, GaP is the crystal of choice in our lab for THz generation and detection simply because of the favorable phase-matching conditions at near 1 μm NIR wavelength [80].

Proper balancing of the photodetectors is also an essential step in ensuring a low noise level during EOS. To achieve this, the THz beam is blocked, the quarter-wave plate ($\lambda/4$) is removed from the beam path, and the Wollaston prism (WP) is oriented such that all the

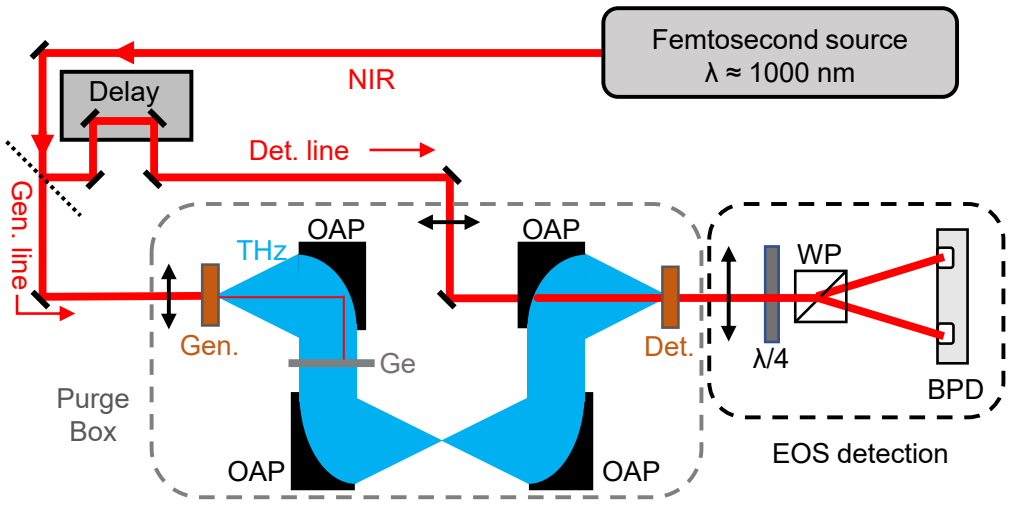

Figure 3.2: Schematic of experimental configuration of standard THz time-domain spectrometer relying on collinear generation and detection geometry in nonlinear crystals.

optical power is incident on one of the detectors. After fixing the WP, the quarter-wave plate is put back in the setup and oriented such that signal on the balanced photodiodes (BPD) is zero (i.e. $\Delta D = 0$). With proper balancing, the position and orientation of the generation and detection crystals are sequentially altered to optimize the THz signal. Finally, the portion of the setup containing the THz radiation is enclosed (usually with 1/4" thick acrylic panes) and purged with dry air to remove absorption spikes in the THz data due to atmospheric water vapor.

Chapter 4

Enabling single-pulse THz spectroscopy with optical fibers

In this chapter, we tackle the issue of data acquisition time required for the detection of phase-locked THz pulses, which often relies on lock-in amplifiers and mechanical delay lines. In general, only dynamics on a timescale longer than the data acquisition time can be resolved. With standard THz detection techniques where the data acquisition time is on the order of minutes, like EOS, the system is limited to resolving only slow phenomena. Here, we built a system capable of retrieving THz waveforms on the order of microseconds and therefore able to resolve microsecond dynamics. The work contained in this chapter relies on more complex THz generation and detection schemes than the one described in the previous chapter. Here, we use the tilted-pulse-front THz generation technique in a lithium niobate ($LiNbO_3$, LN) crystal and chirped-pulse spectral encoding (CPSE) combined with a photonic time-stretch technique for THz detection, allowing single THz pulses to be detected with fast electronics.

4.1 Tilted-pulse-front THz generation

A key advantage to using LN as a nonlinear medium for THz generation is that its electro-optic coefficient is significantly larger than other common crystals used for THz generation such as the ones listed in Table 2.1; enabling the generation of higher THz fields through nonlinear optical effects. The electro-optic coefficient of LN is 168 pm/V [81], GaP is 1 pm/V [82], and GaSe is 54 pm/V [83]. However, the phase-matching conditions in LN are extremely unfavorable for NIR frequencies. Recall from section 2.2.1 that the group velocity of the NIR pulse must match the phase velocity of the generated THz frequency for optimal phase matching. In LN, the group index (n_g) near 1 μm is nearly two times lower than the phase index at 1 THz (300 μm) [84, 85]. A tilted-pulse-front technique can be used to overcome this significant phase mismatch, where we have implemented the configuration described in [86] and schematically shown in Fig. 4.1a.
In short, the NIR beam is shined onto a blazed grating to tilt the pulse-front and the grating is then imaged onto the LN crystal. The crystal is cut as a wedge and the pulse-front-tilt angle, controlled with the angle of incidence on the grating, is chosen such that

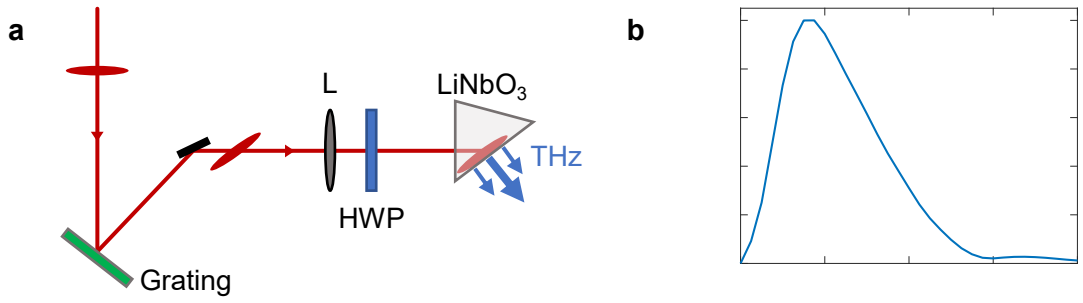

Figure 4.1: a) Schematic of tilted-pulse-front THz generation scheme. A NIR pulse (red line) with pulse-front (red shaded area) initially perpendicular to direction of propagation is incident on a diffraction grating, tilting the pulse-front to match the angle of the crystal wedge. A lens (L) images the grating onto the crystal and a half-wave plate (HWP) rotates the linear polarization of the NIR beam to optimize THz generation. The THz radiation (blue) is emitted perpendicular to the tilted pulse-front. b) Spectrum of THz field detected with EOS from the titled-pulse-front generation scheme with a PHAROS laser.

the tilt matches the angle of the wedge. A half-wave plate (HWP) alters the polarization of the NIR beam incident on the crystal to optimize THz generation. As the NIR propagates through the crystal, it emits wavelets of THz waves at different positions in the crystals. Since the THz waves travel much slower than the NIR, the wavelets generated at different positions interfere constructively in a direction orthogonal to the pulse-front-tilt angle, creating a Cherenkov-like cone of emitted radiation [87]. This is known as a non-collinear phase matching scheme, as the generated THz field does not propagate collinearly with the NIR wave responsible for its generation. This offers an important technical advantage: Since the NIR leaking through the crystal does not follow the THz beam path, we do not need to place a spectral filter, like a germanium wafer, to block the NIR and transmit the THz light. This lack of component in the THz beam path provides a higher THz field (factor of 2) to reach the detection crystal, thereby increasing the detection efficiency.
Upon exiting the LN crystal, the THz radiation is collimated then focused onto a detection crystal with OAP mirrors. The spectrum generated from this type of scheme peaks just below 1 THz and extends to nearly 3 THz, as shown in Fig. 4.1b. This THz generation scheme can reach field strengths of several hundred kV/cm with an appropriate ultrafast NIR source, as the large damage threshold of LN can handle considerable NIR intensities. High intensity THz sources can be applied to interesting studies such as nonlinear THz spectroscopy and nonlinear optics [87], and even THz-pump THz-probe spectroscopy [88]. In our case, however, we instead utilize strong THz fields to enable single-pulse THz spectroscopy, where the detection scheme relying on weak nonlinear interactions does not benefit from lock-in detection and averaging to lower the noise level.

4.2 Single-pulse THz spectroscopy

With this high-field THz source and appropriate focusing optics to tightly focus the THz radiation on a detection crystal, we can achieve sufficient nonlinear interaction in a detection crystal to abandon averaging and resolve single THz pulses. To achieve this, we implement CPSE (employing GaP as the $\chi^{(2)}$ crystal) and a photonic time-stretch technique, which are described in section 2.2.3. The combination of these techniques, schematically shown in Fig. 4.2, allows us to resolve single THz pulses at arbitrary repetition rates. The “eye-

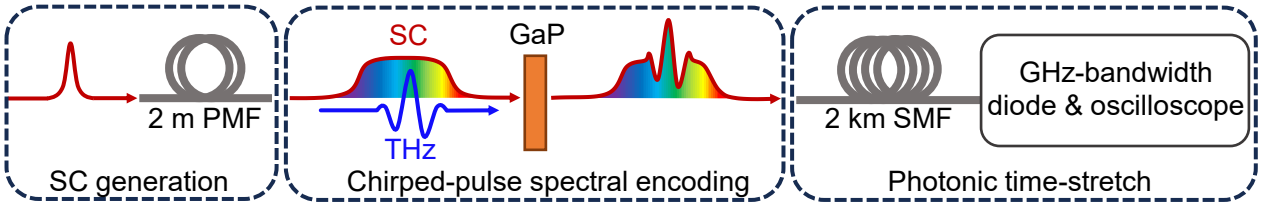

Figure 4.2: Schematic of chirped-pulse spectral encoding combined with photonic time-stretch technique. A NIR pulse is launched into a 2 m-long polarization maintaining fiber (PMF), generating a chirped supercontinuum (SC) with a duration of a few picoseconds. The SC and a THz pulse are spatially and temporally overlapped in a GaP crystal, imprinting the THz waveform onto the spectrum of the SC. The SC carrying the THz information in injected into a 2 km-long single-mode fiber, dispersing the pulse into the nanosecond regime, effectively mapping the frequency components to the time domain. The spectrum is subsequently resolved in time with a GHz-bandwidth photodiode and oscilloscope.

candy" version of this schematic is displayed in Fig. 4.3. The combination of these two techniques has even enabled THz detection rates of 88 MHz, which detected THz pulses emitted from a synchrotron source which therefore benefitted from high energy THz pulses at high repetition rates [89]. Here, we sacrifice THz pulse energy by using an ultrafast source but drastically decrease the size of the system, which is entirely table-top. Relying on a single ultrafast source for THz generation and detection also eliminates issues arising due to timing jitter between multiple optical sources.

We used this detection technique to perform single-pulse THz spectroscopy with 20 μs resolution. The results were published in *Nature Communications* in 2023 in an article titled "Single-pulse terahertz spectroscopy monitoring sub-millisecond time dynamics at a rate of 50 kHz" [33], and presented at several conferences [90, 91, 92]. This article and supplementary information document are found in this chapter in their published forms. In this article, we performed optical-pump THz-probe spectroscopy and monitored THz probe pulses transmitted through a silicon wafer as optically injected carrier modified the material's parameters on a pulse-to-pulse basis with an entirely table-top experimental setup. We extracted the real and imaginary parts of the evolving dielectric function every 20 μs with methods described in section 2.2.4 and a modified version of the Drude model

to account for the inhomogeneous carrier distribution within the thick wafer. For more information on the performance of this system, we direct the reader to our pre-print which investigated its signal-to-noise ratio and dynamic range at several laser repetition rates up to 1.1 MHz (i.e. <1 μs resolution) [93].

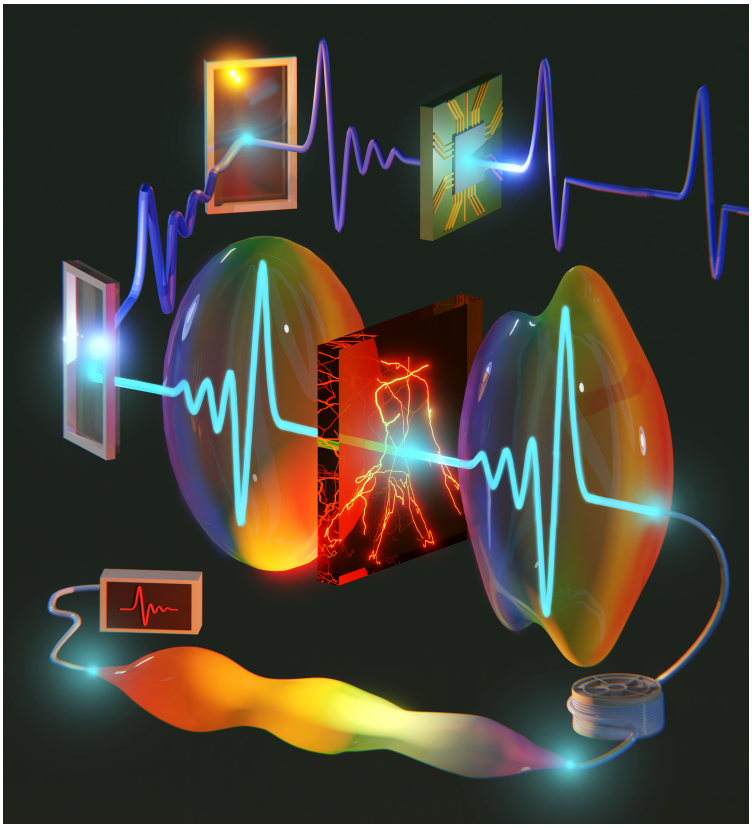

Figure 4.3: Artist rendition of the single-pulse THz spectroscopy experiments probing a silicon chip before interaction with a chirped SC.

nature communications

Article

https://doi.org/10.1038/s41467-023-38354-3

Single-pulse terahertz spectroscopy monitoring sub-millisecond time dynamics at a rate of 50 kHz

Received: 7 September 2022

Accepted: 25 April 2023

Published online: 05 May 2023

Check for updates

Nicolas Couture[1,2] ✉, Wei Cui[1,2], Markus Lippl[3,4], Rachel Ostic[1,2], Défi Junior Jubgang Fandio[1,2], Eeswar Kumar Yalavarthi[1,2], Aswin Vishnuradhan[1,2], Angela Gamouras[1,5], Nicolas Y. Joly[4,3,6] & Jean-Michel Ménard[1,2,5] ✉

Slow motion movies allow us to see intricate details of the mechanical dynamics of complex phenomena. If the images in each frame are replaced by terahertz (THz) waves, such movies can monitor low-energy resonances and reveal fast structural or chemical transitions. Here, we combine THz spectroscopy as a non-invasive optical probe with a real-time monitoring technique to demonstrate the ability to resolve non-reproducible phenomena at 50k frames per second, extracting each of the generated THz waveforms every 20 µs. The concept, based on a photonic time-stretch technique to achieve unprecedented data acquisition speeds, is demonstrated by monitoring sub-millisecond dynamics of hot carriers injected in silicon by successive resonant pulses as a saturation density is established. Our experimental configuration will play a crucial role in revealing fast irreversible physical and chemical processes at THz frequencies with microsecond resolution to enable new applications in fundamental research as well as in industry.

A large class of phenomena is currently impossible to investigate since they are either too fast, non-reproducible, or both. Slow motion movies and high-speed video captures help us visualize events such as the locomotion of organisms, biological processes, as well as fluid and particle dynamics in the visible and near-infrared (NIR) spectral ranges. Similar time-resolved imaging techniques in the far-infrared could provide unique insight into chemical reactions and physical processes that will not only deepen our understanding of the world around us, but will also reveal insights into future technologies. Water distribution in plants[1], carrier transport in materials[2], and protein dynamics[3] could be analyzed at sub-millisecond timescales, leading to ground-breaking scientific discoveries. In industry, implementation of fast terahertz time-domain spectroscopy (THz-TDS) would provide efficient and non-invasive quality control of goods. For example, in pharmaceutical assembly lines, such a characterization technique would allow companies to determine with great accuracy the material content and thickness of the coating on their tablets, a crucial component of the solid drug delivery mechanism, without sacrificing any satisfactory tablets[4]. The current issue with THz-TDS for these applications, is that the technique mostly relies on electro-optic sampling (EOS) in electro-optic crystals[5,6]. Although EOS in general directly provides the full amplitude and phase information to extract the complex dielectric function of materials, it is a relatively slow point-by-point sampling process that involves mechanically scanning a NIR pulse across a THz wave. To combat this shortcoming, researchers have been attempting to decrease the scanning and data acquisition time required to retrieve the full THz transient by replacing the mechanical delay line by more sophisticated techniques such as rotary mirror arrays[7], electronically

[1]Department of Physics, University of Ottawa, Ottawa, ON K1N 6N5, Canada. [2]Max Planck Centre for Extreme and Quantum Photonics, Ottawa, ON K1N 6N5, Canada. [3]Max Planck Institute for the Science of Light, 91058 Erlangen, Germany. [4]Department of Physics, University of Erlangen-Nürnberg, 91058 Erlangen, Germany. [5]National Research Council Canada, Ottawa, ON K1A 0R6, Canada. [6]Interdisciplinary Center for Nanostructured Films, 91058 Erlangen, Germany. ✉[redacted]

controlled optical sampling[8], asynchronous optical sampling[9], optical sampling by cavity tuning[10], and acousto-optic programmable dispersive filters[11]. These methods of THz detection have increased scanning rates from a fraction of Hz to the kHz range.

Another approach to decreasing data acquisition times in THz-TDS has been to implement single-shot THz detection through time-to-frequency (which includes spectral encoding[12] and spectral interferometry[13,14]), time-to-space[15], and time-to-angle[16] mapping techniques[17]. In fact, THz-TDS of a unique transient state has been realized with these approaches. For example, it has been used to resolve strong magnon–magnon coupling[18] and measure the complex dielectric function of semiconductors[19], thin metal films[20], and other THz materials[21]. Of these listed methods, frequency-to-time mapping by spectral encoding is arguably the most straightforward to implement as it requires only minor modifications to a standard THz-TDS system. It is accomplished by spatially and temporally overlapping a chirped NIR detection pulse with a THz pulse in an electro-optic crystal, such as gallium phosphide (GaP) or zinc telluride (ZnTe), resulting in the time-domain waveform of the THz pulse being imprinted via nonlinear effects onto the NIR spectrum. Single-shot THz detection has been achieved with this technique by resolving THz pulses, generated with ultrafast sources, imprinted onto a NIR pulse with a spectrometer based on cameras[20,22]. Nevertheless, the data collection and data transfer processes performed by the spectrometer can be drastically limited by the speed of the electronics and the large number of photodetectors, which limits the practicality of these approaches. To our knowledge, the fastest table-top shot-to-shot THz-TDS to date is 1 kHz and utilizes the echelon mirror technique[23]. Single-pulse THz detection has also been achieved at MHz acquisition rates using the photonic time-stretch technique[22,24–27], where the experiments relied on large synchrotron facilities and therefore benefited from large peak power at high repetition rates. Table-top optical sources offer a trade-off between the repetition rate and the peak power, where the latter determines the amplitude of the generated THz electric field. Therefore, a higher repetition rate leads to a lower generated THz field amplitude and a lower signal-to-noise ratio (SNR) in experiments resolving single THz pulses. This trade-off is expected to represent a bottleneck for reaching arbitrarily high repetition rates in single-pulse THz-TDS systems.

Here, we present a complete table-top system capable of single-pulse THz-TDS at a repetition rate of 50 kHz based on chirped-pulse spectral encoding, a photonic time-stretch measurement technique, and fast detection electronics[28,29]. The resulting system relies on a single ultrafast source, which enables the detection of every single generated THz pulse, emitted and detected every 20 µs. To explore the capabilities of our system, we monitor pulse-to-pulse microsecond carrier dynamics in a silicon wafer using successive pairs of NIR pump and THz probe pulses in a transient regime. Each THz wave transmitted through the sample is time-resolved every 20 µs, providing phase and amplitude information, to achieve single-pulse THz spectroscopy of the pump-induced change in the complex dielectric function. With the standard EOS technique, only the equilibrium states of the sample can be measured: the un-pumped or saturated states. With the single-pulse detection technique, we probe the sample at the repetition rate of the laser (50 kHz) to obtain a series of measurements tracing microscopic dynamics that are changing on a pulse-to-pulse basis. Using a theory based on the Drude model, we can extract the density and relaxation time of injected carriers by analyzing the complex transmission spectrum of the THz pulse. We also include in our model dynamic effects such as inhomogeneous carrier distribution in the sample along the THz propagation direction, spatial diffusion, and carrier density-dependent scattering time. The system we present in this work lays the foundation towards the implementation of THz-TDS as a non-invasive tool for quality control of pharmaceuticals and as a low-energy probe to resolve microsecond processes such as the motion of proteins[30,31], chemical and physical exchange processes[32], and other complex systems in all fields of scientific research.

Results

Experiments are performed with an amplified ultrafast laser source delivering femtosecond pulses at a 50 kHz repetition rate. We generate THz transients by optical rectification using the standard tilted-pulse-front configuration in a lithium niobate ($LiNbO_3$) crystal[33] and resolve each transient with a structured NIR gating pulse as schematically shown in Fig. 1a. This gating pulse is obtained by launching a NIR pulse into a 2 meter-long polarization-maintaining fiber (PMF). Self-phase modulation and linear dispersion in the fiber yield a chirped NIR supercontinuum (SC) with ~100 nm bandwidth and 6 ps pulse

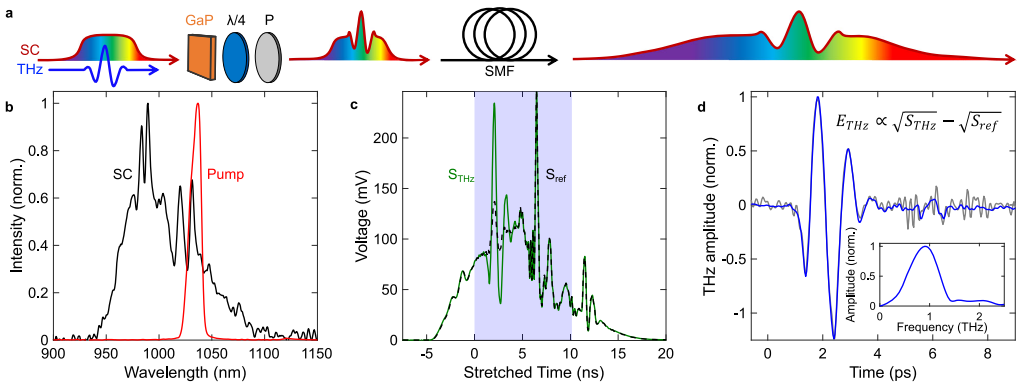

Fig. 1 | Single-pulse THz detection scheme. a Schematic of the spectral encoding of the THz pulse onto the spectrum of the chirped supercontinuum (SC) in a 2-mm-thick gallium phosphide (GaP) crystal. The modulated spectrum is passed through a quarter-wave plate (λ/4) and a polarizer (P) and then coupled into a 2 km-long single-mode fiber (SMF), mapping the frequencies of the NIR pulse to the time-domain to then be resolved on an oscilloscope. **b** Spectrum of the pulse injected into the short polarization maintaining fiber (Pump) and the output supercontinuum (SC), which is used for spectral encoding. **c** Measured signals of the modulated (S_{THz}) and unmodulated (S_{ref}) spectra on the oscilloscope. The area highlighted in blue represents the relevant section of the spectrum which contains the THz transient. **d** Extracted THz electric field (E_{THz}) from the curves in **c** and the Fourier transform of the averaged transient (inset). The blue line is the signal averaged over 10k pulses while the gray line is a single-pulse measurement.

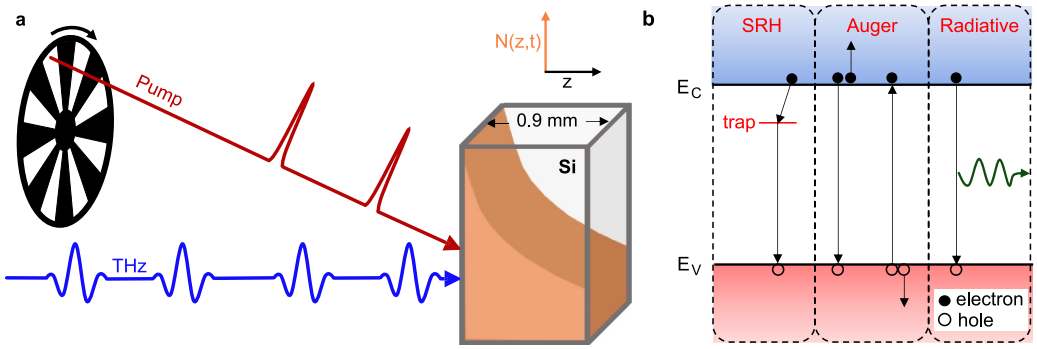

Fig. 2 | Optical-pump THz-probe single-pulse THz spectroscopy. a Schematic of the experimental configuration used to measure the low-energy response of optically injected carrier density $N(z, t)$ (orange) in a 0.9 mm-thick nominally undoped silicon (Si) sample. The train of NIR resonant pulses (Pump) can be chopped to investigate the dynamics of pulse-to-pulse carrier injection followed by carrier relaxation. **b** Schematic of the recombination mechanisms considered in simulations where the red area represents the valence band (E_V), and blue represents the conduction band (E_C). Shockley–Read–Hall (SRH), Auger, and radiative recombination mechanisms are considered.

duration. The spectra measured before and after nonlinear propagation in the PMF are shown in Fig. 1b. The stretched pulse is then used to encode, through a nonlinear interaction process, an oscillating THz transient by spatially and temporally overlapping the two beams into a second-order nonlinear crystal. After the nonlinear interaction process, the oscillating THz field is encoded in the polarization state of individual spectral components of the SC. To read this information with optimal sensitivity, we first use a quarter-wave plate and a linear polarizer to efficiently extract the THz-modulated signal while blocking most of the unaltered NIR beam. We then perform the photonic time-stretch technique, a single-pulse spectroscopy technique also known as the dispersive Fourier transform, by dispersing spectral components of the polarization-filtered SC into a 2 km-long commercial single-mode fiber (SMF) before time-resolving each nanosecond-stretched NIR pulse with fast electronics. A background signal is removed by subtracting the unmodulated SC (S_{ref} in Fig. 1c) from the THz-modulated SC (S_{THz} in Fig. 1c). Both signals, approximately 20 ns in duration, recorded with the oscilloscope after propagation through the 2 km-long SMF are plotted in Fig. 1c. The resulting signal is the THz transient (E_{THz}), which is shown in Fig. 1d along with its spectrum (inset) corresponding to the Fourier transform. The derivation of the formula shown in Fig. 1d can be found in section 2 of the Supplementary Information. The oscilloscope time axis is calibrated by comparing measurements obtained at different time intervals between the THz and detection NIR pulses, which is accurately controlled by a delay stage[34]. The resulting linear relationship between relative delay (in ps) and stretched time on the oscilloscope (in ns) yields the calibration factor, otherwise known as the time-stretch factor, of 1130. With this technique, the THz acquisition rate is determined by the repetition rate of the laser; meaning that with a laser emitting NIR pulses at a rate of 50 kHz, we retrieve corresponding THz waveforms every 20 μs.

Monitoring pulse-to-pulse carrier accumulation dynamics

We demonstrate the capabilities of our single-pulse THz detection scheme by performing optical-pump THz-probe spectroscopy on 0.9 mm-thick nominally undoped silicon to monitor carrier dynamics. Such measurements can notably be used to monitor the accumulation of optically injected carriers from successive pump pulses or the gradual recombination of free carriers. Intrinsic silicon has a relatively long carrier relaxation time of a few hundred microseconds at low carrier densities. As a result, successive resonant pump pulses at a repetition rate of 50 kHz lead to carrier accumulation until a saturation density is reached. In general, the single-pulse technique provides a unique access to fast dynamical systems as standard pump-probe schemes are not only inadequate to probe non-reproducible phenomena, but would require km-long delay lines to map out microsecond dynamics.

We perform these experiments in two manners: (i) by activating the pump and probe pulses simultaneously to observe the carrier saturation dynamics and (ii) by inserting a chopper in the pump beam to monitor both the carrier accumulation and recombination dynamics, which are cyclically reproduced as the pump beam is being blocked and unblocked (Fig. 2a). We use a translation stage to adjust the time delay between the THz probe and NIR pump pulses, allowing us to adjust the THz probe to any time delay before or after carrier injection by the corresponding NIR pump pulse. When the probe shortly precedes the pump pulse, spectroscopy measurements become sensitive to residual carriers with unique characteristics as they undergo about 20 μs (or the inverse of the laser repetition rate) of thermalization, diffusion and recombination. Inhomogeneous carrier distribution ($N(z,t)$) along the propagation direction of the pump (z) is assumed as well as Shockley–Read–Hall (SRH), Auger, and radiative carrier recombination mechanisms (Fig. 2b). We also consider spatial diffusion in our model.

Figures 3a–c show the peak amplitude of the transmitted THz pulse, which can be used to indicate the carrier density as a function of time. We explore three pump power regimes injecting different carrier densities corresponding to 0.6×10^{15}, 1.1×10^{15}, and 2×10^{15} cm^{-3} per pulse. The experiments are repeated several times for each carrier density considered in order to extract a standard deviation – the data presented in Fig. 3 is averaged over ten iterations. Obtaining a standard deviation is an essential step in evaluating the signal-to-noise ratio. The fact that the silicon wafer experiences the same equilibrium state before optical pumping allows us to perform several experiments under the same conditions. The standard deviation, represented as error bars in Fig. 3a–c, quantitatively demonstrates the reproducibility and validity of our single-pulse THz-TDS technique and shows a relative variation of ~10% for all data points. The experiment is performed as the THz probe pulse is delayed by 300 ps after the NIR pump pulse (dark colored circles) or precedes the same pump pulse by 130 ps (light colored circles). In our experiment, the saturation carrier density is reached after 200 μs, corresponding to 10 pump pulses. At low pump pulse energy, fewer carriers are injected into the sample resulting in a lower absorption of the THz field and a higher overall transmission amplitude. Conversely, the transmission is the lowest at the highest

https://doi.org/10.1038/s41467-023-38354-3

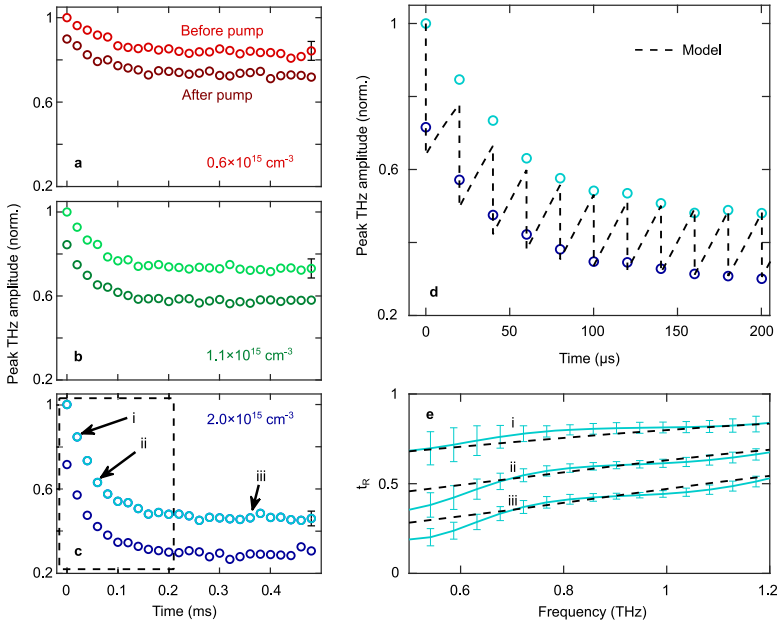

Fig. 3 | Carrier accumulation dynamics in silicon monitored with single-pulse THz detection. The peak of the THz transient as the pump pulses arrive before (dark circles) and after (light circles) the THz pulse for carrier densities of **a** 0.6 (red), **b** 1 (green), and **c** 2 (blue) $\times 10^{15}$ cm^{-3}. The area inside the dashed line box in **c** is displayed in **d** along with the results from theoretical calculations (dashed black line). **e** Transmission of the amplitude spectra relative to the unpumped silicon (t_R) of the pulses labeled *i*–*iii* in Fig. 3c and results from the theoretical model (dashed black line). Theoretical time dynamics are calculated with the Drude model and the free carrier rate equation considering an initial recombination time of 30 μs, a density of available traps of 6×10^{11} cm^{-3}, and an initial scattering time of 190 fs. Error bars throughout all panels represent the standard deviation over ten measurements.

pump pulse energy. Here, we take advantage of the fact that optically injected carrier dynamics in semiconductors is a pulse-to-pulse reproducible process to average data collected over ten measurements. In Fig. 3d, we plot the same data as in Fig. 3c on a shorter time scale to resolve fine details of the time-varying THz transmission during carrier accumulation from the successive NIR pump pulses. As carriers accumulate in the sample with each pump pulse, we observe an increase of the rate of carrier recombination. Our experimental results agree well with numerical calculations of photocarrier dynamics in silicon (dashed black line). In these simulations, we model the inhomogeneous injected carrier distribution by considering multiple thin slices of fixed carrier concentration across the Si sample in the direction of THz propagation (z). Carrier relaxation mechanisms listed in Fig. 2b are considered for each slice as well as carrier diffusion across neighboring slices. The THz absorption of each region is modeled with the Drude model and Beer–Lambert law. Then, these results are combined to obtain the transmission amplitude through the whole sample thickness. Calculations are carried out with an initial trap-assisted effective recombination time of 30 μs, a density of available traps of 6×10^{11} cm^{-3} and an intrinsic scattering time of 190 fs. With these standard parameters[35–37], our model and experimental measurements are in good agreement. A more detailed description of the model is provided in section 3 of the Supplementary Information. The real part of the transmitted THz amplitude spectrum relative to the unpumped silicon (t_R) of three measurements labeled *i*–*iii* in Fig. 3c is displayed in Fig. 3e, error bars corresponding to the standard deviation over ten measurements, along with the corresponding calculated transmission spectra using the model described above (dashed black lines). Here we limit our analysis to the frequency components contained within the FWHM of the THz spectrum shown in Fig. 1d. We also find a good agreement between the model and the measurements in this case. Since carrier-induced absorption preferentially reduces the spectral amplitude at low frequencies, creating a steep spectral edge, we obtain the smallest error bars in the region around 0.9 THz and slightly higher ones near 0.6 THz. Note that an experimental THz scheme relying on the standard EOS detection technique could be used to characterize steady states, corresponding here to the measurements *iii* in the saturation regime, but not the microsecond dynamics revealing transient states, such as the measurements corresponding to *i* and *ii*.

We use the complex transmission amplitude to calculate the change in the real and imaginary parts of the dielectric function, which are shown in Fig. 4a, b, respectively[38]. In our experiment, we can neglect the effect of the carrier density on the Fresnel transmission coefficient. As a result, the phase difference between the pumped and unpumped silicon is associated with the change in the refractive index of the sample, while t_R, shown in Fig. 3e, is directly associated to the change in absorption. We consider the same three measurements *i*–*iii*, as those identified in Fig. 3c, e, but this time we overlay the experimental results with a standard Drude model. The basic model is based on a homogenous carrier distribution, which is a valid approximation considering that diffusion has 20 μs after the last NIR excitation pulse to flatten the carrier distribution. We also set a non-carrier dependent scattering time for simplicity. Overall, we observe excellent agreement (dashed black lines) with carrier density corresponding to 4×10^{14}, 8.5×10^{14}, 1.4×10^{15} cm^{-3} and a scattering time corresponding to 155 fs. The data presented in Figs. 3 and 4 shows that our single-pulse THz detection scheme can reliably perform spectroscopy and extract material parameters at a rate of 50 kHz, allowing us to observe dynamical changes in a system by resolving each successive THz pulse

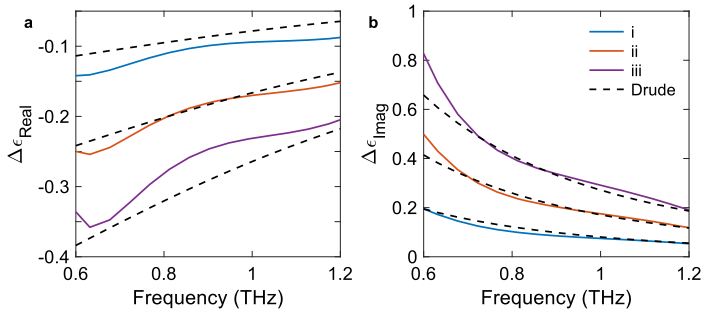

Fig. 4 | Pulse-to-pulse changes in the complex dielectric function of optically pumped silicon. Extracted **a** real and **b** imaginary change in dielectric function calculated from the transmission spectra presented in Fig. 3e (pulses labeled *i*, *ii*, and *iii*) and the phase information of the THz pulses. Carrier distribution and scattering time (fixed at 155 fs) are used as fitting parameters for the Drude model.

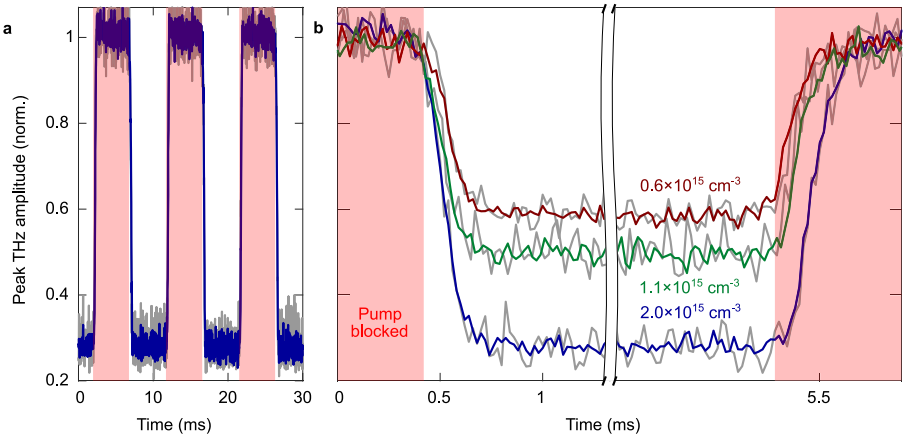

Fig. 5 | Amplitude variations of THz transients tracing cyclical carrier accumulation and relaxation dynamics. Optical-pump THz-probe results achieved by tightly focusing the pump beam into a mechanical optical chopper, with the pump pulse arriving before the THz probe. **a** Injected carrier density is fixed at 2×10^{15} cm^{-3} and the peak THz amplitude from single-pulse THz detection is extracted over three chopper cycles. **b** Peak THz amplitude extracted the same way as in **a**, with carrier densities of 0.6 (red), 1.1 (green), and 2 (blue) $\times 10^{15}$ cm^{-3}. The areas highlighted in red correspond to the situation without any pump. Colored lines represent data averaged over 3 chopper cycles, while gray lines are single-pulse measurements.

separated by 20 μs. Standard pump-probe techniques intrinsically relying on pulse averaging cannot be used to directly extract the same information.

Resolving carrier accumulation and relaxation

In a second type of experiment, we use a chopper wheel to block and unblock the pump beam. Carrier accumulation and recombination dynamics in Si are recorded cyclically at a frequency of 100 Hz while measuring the transmitted THz transient with the single-pulse detection technique. Figure 5a shows the peak THz amplitude over three chopper cycles and Fig. 5b provides a closer look over a single chopper cycle. This configuration not only allows us to measure the carrier injection dynamics as in Fig. 3, but also passively measures the carrier recombination dynamics when the pump pulse is blocked by the chopper (red highlighted area). On the left side of Fig. 5b, after the pump is unblocked, we have the carrier injection rate for each previously considered pump energies; and on the right side of Fig. 5b, after the pump is blocked, we have carrier recombination times which depend on the carrier density in the silicon. Our experiment yields the full recombination dynamics occurring over a millisecond time scale, while standard optical-pump THz-probe systems relying on a translation stage to incrementally change the time delay between the pump and probe are limited to nanoseconds scanning range due to the physical size of the stage. More importantly, the THz time-domain signal is sampled at a frequency of 50 kHz, corresponding to the repetition rate of the laser, allowing us to resolve fast and complex temporal dynamics. In our experiment, the excitation pulse is periodically chopped, allowing measurements to be repeated over several identical cycles. As shown in Fig. 5b, the SNR corresponding to single-pulse (gray lines) data is increased when we average over three cycles (colored lines) because carrier dynamics in semiconductors are reproducible for identical optical excitation conditions. However, no averaging is intrinsically required to monitor low-energy dynamics, and this is one of the main advantages of this technique. As such, we believe our system to be appropriate for the exploration of non-reproducible phenomena such as oxidation or combustion, or the study of chaotic dynamical systems notably arising in chemistry and biology. Finally, we believe improvements to our current setup will lead to an improved SNR of single-pulse measurements allowing us to operate the system at MHz frequencies to resolve sub-microsecond dynamics.

In summary, we have presented a table-top system capable of single-pulse THz spectroscopy by combining chirped-pulse spectral encoding and a photonic time-stretch. With this technique, we have experimentally revealed pulse-to-pulse carrier dynamics and changes in the complex dielectric function of silicon. We have validated these experimental results with theory considering diffusion and Shockley-Read-Hall, Auger, and radiative recombination mechanisms. Although we performed our THz spectroscopy experiments at a repetition rate of 50 kHz, revealing sub-millisecond dynamics in silicon, our acquisition rate was limited only by the signal-to-noise ratio at higher repetition rates. Further development of this system will enable us to reach acquisition rates in the MHz to reveal sub-microsecond processes in systems resonant to THz frequencies. This THz-TDS technique promises to be a powerful tool for the observation of fast physical, biological, and chemical processes, non-reproducible phenomena, chaotic systems, and a robust technique for rapid non-invasive quality control in industrial applications.

Methods

The setup relies on an amplified ultrafast laser source delivering 180 fs pulses (FWHM) at a central wavelength of 1030 nm, a pulse energy of 120 µJ, and a repetition rate of 50 kHz. The optical beam is split into three paths (a schematic of the experimental setup is shown in Fig. S1 of the Supplementary Information). In the first path, NIR pump pulses impinge on the silicon sample for resonant excitation. In the second path, where most of the optical power lies, the NIR pulses are used to generate THz pulses in a lithium niobate ($LiNbO_3$) crystal with a tilted-pulse-front configuration[33]. In the third path, the NIR beam is launched into a 2 m-long PMF (OZ Optics PMF-980-6/125-0.25-L) to obtain a chirped SC with ~100 nm bandwidth and 6 ps pulse duration. This stretched pulse is then used to encode, through a nonlinear interaction process in a 2 mm-thick 110-oriented GaP crystal, an oscillating THz transient. Using this technique, we can trace an oscillating THz field with a resolution of $\delta t = 300$ fs (see section 1 of the Supplementary Information for details about this calculation)[12], reliably resolving frequencies up to 1.6 THz according to the Shannon–Nyquist criteria. Polarization filtering is performed with a quarter-wave plate and a linear polarizer to limit the transmission of unaltered NIR light. We then perform the photonic time-stretch technique by dispersing spectral components of the polarization-filtered SC into a 2 km-long SMF (Corning HI1060 flex) before time-resolving each nanosecond-stretched NIR pulse with a fast photodiode (Newport 1544-B, 12 GHz, 32 ps rise time) and a GHz-bandwidth oscilloscope (Tektronix MSO68B, 10 GHz).

Reporting summary

Further information on research design is available in the Nature Portfolio Reporting Summary linked to this article.

Data availability

The data in this study have been deposited in the Figshare database and are available to the public at https://doi.org/10.6084/m9.figshare.22575004.

Code availability

The code used in this study is available from the corresponding author upon request.

References

1. Shchepetilnikov, A. V., Zarezin, A. M., Muravev, V. M., Gusikhin, P. A. & Kukushkin, I. V. Quantitative analysis of water content and distribution in plants using terahertz imaging. *Opt. Eng.* **59**, 061617 (2020).
2. Delport, G., Macpherson, S. & Stranks, S. D. Imaging carrier transport properties in halide perovskites using time-resolved optical microscopy. *Adv. Energy Mater.* **10**, 1903814 (2020).
3. Wolff, A. M. et al. Mapping protein dynamics at high-resolution with temperature-jump X-ray crystallography. Preprint at *bioRxiv* https://doi.org/10.1101/2022.06.10.495662 (2022).
4. Ho, L. et al. Analysis of sustained-release tablet film coats using terahertz pulsed imaging. *J. Controlled Release* **119**, 253–261 (2007).
5. Aoki, K., Savolainen, J. & Havenith, M. Broadband terahertz pulse generation by optical rectification in GaP crystals. *Appl. Phys. Lett.* **110**, 201103 (2017).
6. Leitenstorfer, A., Hunsche, S., Shah, J., Nuss, M. C. & Knox, W. H. Detectors and sources for ultrabroadband electro-optic sampling: experiment and theory. *Appl. Phys. Lett.* **74**, 1516–1518 (1999).
7. Molter, D. et al. High-speed terahertz time-domain spectroscopy of cyclotron resonance in pulsed magnetic field. *Opt. Express* **18**, 26163–26168 (2010).
8. Kim, Y. & Yee, D.-S. High-speed terahertz time-domain spectroscopy based on electronically controlled optical sampling. *Opt. Lett.* **35**, 3715–3717 (2010).
9. Yasui, T., Saneyoshi, E. & Araki, T. Asynchronous optical sampling terahertz time-domain spectroscopy for ultrahigh spectral resolution and rapid data acquisition. *Appl. Phys. Lett.* **87**, 061101 (2005).
10. Hochrein, T. et al. Optical sampling by laser cavity tuning. *Opt. Express* **18**, 1613–1617 (2010).
11. Urbanek, B. et al. Femtosecond terahertz time-domain spectroscopy at 36 kHz scan rate using an acousto-optic delay. *Appl. Phys. Lett.* **108**, 121101 (2016).
12. Jiang, Z. & Zhang, X.-C. Electro-optic measurement of THz field pulses with a chirped optical beam. *Appl. Phys. Lett.* **72**, 1945–1947 (1998).
13. Sharma, G., Singh, K., Al-Naib, I., Morandotti, R. & Ozaki, T. Terahertz detection using spectral domain interferometry. *Opt. Lett.* **37**, 4338–4340 (2012).
14. Zheng, S. et al. Improved common-path spectral interferometer for single-shot terahertz detection. *Photonics Res.* **6**, 177 (2018).
15. Shan, J. et al. Single-shot measurement of terahertz electromagnetic pulses by use of electro-optic sampling. *Opt. Lett.* **25**, 426–428 (2000).
16. Minami, Y., Hayashi, Y., Takeda, J. & Katayama, I. Single-shot measurement of a terahertz electric-field waveform using a reflective echelon mirror. *Appl. Phys. Lett.* **103**, 051103 (2013).
17. Teo, S. M., Ofori-Okai, B. K., Werley, C. A. & Nelson, K. A. Invited Article: Single-shot THz detection techniques optimized for multidimensional THz spectroscopy. *Rev. Sci. Instrum.* **86**, 051301 (2015).
18. Makihara, T. et al. Ultrastrong magnon–magnon coupling dominated by antiresonant interactions. *Nat. Commun.* **12**, 3115 (2021).
19. Minami, Y., Horiuchi, K., Masuda, K., Takeda, J. & Katayama, I. Terahertz dielectric response of photoexcited carriers in Si revealed via single-shot optical-pump and terahertz-probe spectroscopy. *Appl. Phys. Lett.* **107**, 171104 (2015).
20. Russell, B. K. et al. Self-referenced single-shot THz detection. *Opt. Express* **25**, 16140 (2017).
21. Du, L. et al. Organic crystal-based THz source for complex refractive index measurements of window materials using single-shot THz spectroscopy. *Appl. Phys. A* **127**, 846 (2021).
22. Roussel, E. et al. Phase diversity electro-optic sampling: a new approach to single-shot terahertz waveform recording. *Light Sci. Appl.* **11**, 14 (2022).
23. Gao, F. Y., Zhang, Z., Liu, Z.-J. & Nelson, K. A. High-speed two-dimensional terahertz spectroscopy with echelon-based shot-to-shot balanced detection. *Opt. Lett.* **47**, 3479–3482 (2022).
24. Roussel, E. et al. Observing microscopic structures of a relativistic object using a time-stretch strategy. *Sci. Rep.* **5**, 10330 (2015).
25. Evain, C. et al. Direct observation of spatiotemporal dynamics of short electron bunches in storage rings. *Phys. Rev. Lett.* **118**, 054801 (2017).

26. Szwaj, C. et al. High sensitivity photonic time-stretch electro-optic sampling of terahertz pulses. *Rev. Sci. Instrum.* **87**, 103111 (2016).
27. Steffen, B. et al. Compact single-shot electro-optic detection system for THz pulses with femtosecond time resolution at MHz repetition rates. *Rev. Sci. Instrum.* **91**, 045123 (2020).
28. Tong, Y. C., Chan, L. Y. & Tsang, H. K. Fibre dispersion or pulse spectrum measurement using a sampling oscilloscope. *Electron. Lett.* **33**, 983–985 (1997).
29. Goda, K., Solli, D. R., Tsia, K. K. & Jalali, B. Theory of amplified dispersive Fourier transformation. *Phys. Rev. A* **80**, 043821 (2009).
30. Otosu, T., Ishii, K. & Tahara, T. Microsecond protein dynamics observed at the single-molecule level. *Nat. Commun.* **6**, 7685 (2015).
31. Thompson, M. C. et al. Temperature-jump solution X-ray scattering reveals distinct motions in a dynamic enzyme. *Nat. Chem.* **11**, 1058–1066 (2019).
32. Dzikovski, B. et al. Microsecond exchange processes studied by two-dimensional ESR at 95 GHz. *J. Am. Chem. Soc.* **142**, 21368–21381 (2020).
33. Hebling, J., Yeh, K.-L., Hoffmann, M. C., Bartal, B. & Nelson, K. A. Generation of high-power terahertz pulses by tilted-pulse-front excitation and their application possibilities. *J. Opt. Soc. Am. B* **25**, B6–B19 (2008).
34. Kobayashi, M. et al. High-acquisition-rate single-shot pump-probe measurements using time-stretching method. *Sci. Rep.* **6**, 37614 (2016).
35. Schroder, D. K. Carrier lifetimes in silicon. *IEEE Trans. Electron Devices* **44**, 160–170 (1997).
36. Yokoyama, K., Lord, J. S., Miao, J., Murahari, P. & Drew, A. J. Photoexcited muon spin spectroscopy: a new method for measuring excess carrier lifetime in bulk silicon. *Phys. Rev. Lett.* **119**, 226601 (2017).
37. Jacoboni, C., Canali, C., Ottaviani, G., & Alberigi Quaranta, A. A review of some charge transport properties of silicon. *Solid State Electron.* **20**, 77–89 (1977).
38. Withayachumnankul, W. & Naftaly, M. Fundamentals of measurement in terahertz time-domain spectroscopy. *J. Infrared Millim. Terahertz Waves* **35**, 610–637 (2014).

Acknowledgements

We would like to acknowledge Testforce Systems Inc. for loaning the Tektronix MSO68B oscilloscope used in these experiments and Lauren Gingras for technical help. J.-M.M. acknowledges funding from the Natural Sciences and Engineering Research Council of Canada (NSERC) Discovery Grant RGPIN-2016-04797 and the Canada Foundation for Innovation (CFI) (Project Number 35269). This work was also supported by the High Throughput and Secure Networks Challenge Program at the National Research Council of Canada. J.-M.M. and A.G. acknowledge the Joint Centre for Extreme Photonics and N.Y.J. and M.L. acknowledge the Max Planck Institute for the Science of Light in Erlangen for financial support.

Author contributions

J.-M.M. and N.Y.J. conceived the idea. N.C., W.C., and M.L. performed the experiments. R.O. built the first version of the experimental setup and collected preliminary data. N.C., D.J.J.F., E.K.Y., and A.V. performed the simulations. N.C., A.G., N.Y.J., and J.-M.M. analyzed the data and wrote the manuscript with the help of all co-authors.

Competing interests

The authors declare no competing interests.

Additional information

Supplementary information The online version contains supplementary material available at https://doi.org/10.1038/s41467-023-38354-3.

Correspondence and requests for materials should be addressed to Nicolas Couture or Jean-Michel Ménard.

Peer review information *Nature Communications* thanks Bernd Steffen and the other, anonymous, reviewer(s) for their contribution to the peer review of this work.

Supplementary Information: Single-pulse terahertz spectroscopy monitoring sub-millisecond time dynamics at a rate of 50 kHz

Nicolas Couture[1,2,*], Wei Cui[1,2], Markus Lippl[3,4], Rachel Ostic[1,2], Défi Junior Jubgang Fandio[1,2], Eeswar Kumar Yalavarthi[1,2], Aswin Vishnuradhan[1,2], Angela Gamouras[1,5], Nicolas Y. Joly[4,3,6], and Jean-Michel Ménard[1,2,5,**]

[1]Department of Physics, University of Ottawa, Ottawa, Ontario K1N 6N5, Canada
[2]Max Planck Centre for Extreme and Quantum Photonics, Ottawa, Ontario K1N 6N5, Canada
[3]Max Planck Institute for the Science of Light, Erlangen 91058, Germany
[4]Department of Physics, University of Erlangen-Nürnberg, Erlangen 91058, Germany
[5]National Research Council Canada, Ottawa, Ontario K1A 0R6, Canada
[6]Interdisciplinary Center for Nanostructured Films, Erlangen 91058, Germany
[redacted]

1. Full description and schematic of the optical-pump THz-probe experimental setup

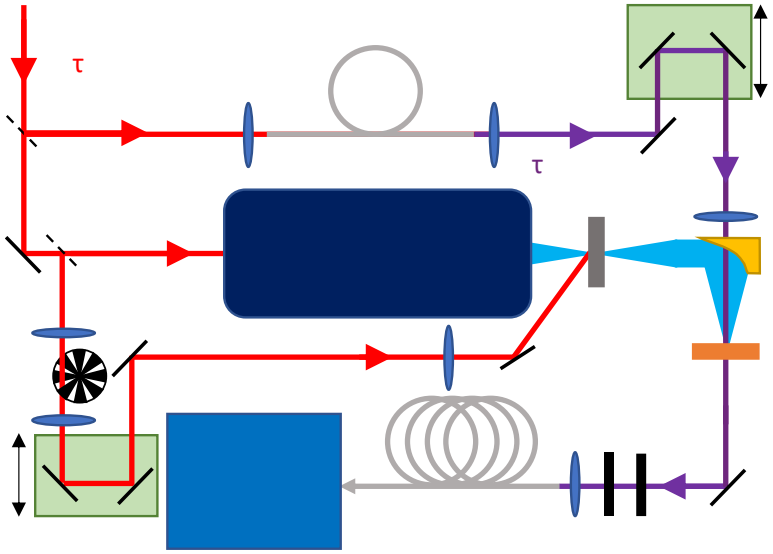

Figure S1. Schematic of the optical-pump THz-probe experimental setup. BS: beamsplitter; PMF: polarization maintaining fiber; DS: delay stage; Si: silicon wafer; GaP: Gallium Phosphide; λ/4: quarter-wave plate; P: polarizer; SMF: single-mode fiber.

The output from a Yb:KGW ultrafast source (1030 nm central wavelength, 120 µJ pulse energy, 50 kHz repetition rate, 180 fs FWHM time duration) (red line) is split into two initial paths with a beamsplitter (BS1, 10R:90T). The reflected beam (12 µJ), to be used as a detection pulse, is attenuated to ~10 nJ and launched into a 2-meter-long polarization maintaining fiber (PMF) whose slow axis is oriented parallel to the linear polarization of the incoming pulse. Self-phase modulation and linear dispersion in the fiber yield a NIR supercontinuum (SC) with a spectral bandwidth approaching ~100 nm and a time duration of 6 ps (purple line Fig. S1). The temporal resolution of this method is given by $\delta t = \sqrt{T_o T_C}$, where T_0 is the unchirped time duration of the SC in the Fourier transform limited case and T_C is the time duration of the chirped pulse[1]. Although the spectral profile of the SC is not Gaussian (Fig. 1b of the main manuscript), a spectral bandwidth of ~100 nm (at 10 dB) is available for spectral encoding; meaning T_0 ~15 fs when assuming a Gaussian temporal profile. The result is a temporal resolution δt = 300 fs, which is sufficient to

resolve the bandwidth of our THz pulse according to the Shannon-Nyquist criterion. The remaining power is passed through a second beamsplitter (BS2, 20R:80T); most of the energy (~86 μJ) is used for THz generation via the tilted-pulse-front technique[2] and the remainder (~22 μJ) is used to optically pump the 0.9-mm-thick silicon wafer (Si). The pump beam is attenuated with neutral density filters (not shown in Fig. S1) to achieve the various carrier injection rates shown in Fig. 3 of the main manuscript. An optical chopper is placed in the beam pumping the silicon, placed at the focus of a 1x telescope. The chopper blade spins fast enough such that fewer than five pulses are only partially transmitted (on average). Delay stages adjust the temporal delay between the detection and THz pulses (DS1), and between the pump and THz pulses (DS2). The experimental setup is used in one of two manners: i) the chopper is off and the pulsed laser output is actively controlled with the pulse picker of the laser; and ii) the laser remains operational with a continuous pulse train output and the chopper is turned on to activate and deactivate the pump at a frequency of 100 Hz. The spot size of the NIR pump on the Si wafer has a radius of ~2 mm at $1/e^2$. The THz pulse transmitted through the Si wafer and the NIR detection pulse are overlapped in a 2-mm-thick gallium phosphide (GaP) crystal. The time domain THz waveform modulates the spectrum of the NIR detection pulse, passes through a quarter-wave plate (λ/4) and polarizer (P), and is launched into a 2-km-long single-mode fiber (SMF). The quarter-wave plate, with its fast axis aligned to the polarization of the unmodulated chirped SC, and linear polarizer, oriented such that the unmodulated chirped SC is nearly completely attenuated (~97% attenuation), filter out unmodulated NIR background light reaching the detector, thus increasing the signal-to-noise ratio of the measurement[1]. The SMF stretches the THz-modulated NIR pulse to the nanosecond timescale such that the spectrum of the NIR pulse is retrieved measuring the temporal intensity trace using a fast photodiode (12 GHz, 32 ps rise time) and oscilloscope (Tektronix MSO68B, 10 GHz bandwidth, 25 GSamples/s). Overall, this scheme measures the THz waveform quite accurately. The standard deviation over 10 measurements typically corresponds to 10% but can still be improved by removing external sources of noise due to air current and vibrations.

2. Derivation of $E_{THz} \propto \sqrt{S_{THz}} - \sqrt{S_{ref}}$

Using Jones matrices, the THz detection conditions used in the main manuscript are derived. The birefringent crystal used for detection is represented as

$$C = \begin{pmatrix} e^{-\frac{in_S L}{\lambda}} & 0 \\ 0 & e^{-\frac{in_f L}{\lambda}} \end{pmatrix} = e^{-i\Theta} \begin{pmatrix} e^{-\frac{i\Gamma}{2}} & 0 \\ 0 & e^{\frac{i\Gamma}{2}} \end{pmatrix}, \tag{S2.1}$$

where L is the crystal length, n_S and n_f are the indices of the slow and fast axes, respectively, and λ is the wavelength. With $\Theta = \frac{(n_s+n_f)L}{2\lambda}$, $\Gamma = \frac{(n_s-n_f)L}{\lambda} \propto \chi^{(2)} E_{THz}$ is the phase retardation experienced by the NIR pulse in the presence of a THz field due to the Pockels effect. Polarization optics include a quarter-wave plate (QWP) with its fast axis aligned horizontally

$$QWP = \begin{pmatrix} e^{-\frac{i\pi}{4}} & 0 \\ 0 & e^{\frac{i\pi}{4}} \end{pmatrix}, \tag{S2.2}$$

and polarizer whose T-axis is oriented at some angle β from the polarization of the NIR detection pulse (horizontal)

$$P(\beta) = (\cos\beta \quad \sin\beta). \tag{S2.3}$$

In our case, the linear polarization of the NIR detection pulse E_i is horizontal such that

$$E_i = E_0 \begin{pmatrix} 1 \\ 0 \end{pmatrix}. \tag{S2.4}$$

As a result, the electric field at the output of our detection scheme becomes

$$E_{out} = P(\beta)\ QWP\ R(-\alpha)\ C\ R(\alpha)\ E_i, \tag{S2.5}$$

where the rotation matrix

$$R(\alpha) = \begin{pmatrix} \cos\alpha & \sin\alpha \\ -\sin\alpha & \cos\alpha \end{pmatrix}, \tag{S2.6}$$

with $\alpha = \pi/4$ ensures maximum modulation from the THz field while maintaining phase information. The intensity $|E_{out}|^2$ yields the measured signal on the diode

$$S = E_0^2 \sin^2\left(\beta - \frac{\Gamma}{2}\right) \tag{S2.7}$$

$$S \approx E_0^2 \left(\beta - \frac{\Gamma}{2}\right)^2 \text{ for } \left|\beta - \frac{\Gamma}{2}\right| \ll 1. \tag{S2.8}$$

In our experiment, $\beta = 0.17$ rad and $\Gamma/2$ is always lower than 0.9 rad, ensuring that the condition defined in Eq. S2.8 is valid and we remain in a linear regime. Thus, without the THz field, the recorded reference signal becomes

$$S_{ref} = S(\Gamma = 0) = \beta^2. \tag{S2.9}$$

With the THz field inducing a birefringence on the crystal, we substitute Eq. S2.10 into the situation where $\Gamma \neq 0$.

$$S_{THz} = S(\Gamma \neq 0) \propto \left(\beta - \frac{\Gamma}{2}\right)^2 \tag{S2.10}$$

$$\sqrt{S_{THz}} \propto \beta - \frac{\Gamma}{2} = \sqrt{S_{ref}} - \frac{\Gamma}{2} \tag{S2.11}$$

$$\Gamma \propto \sqrt{S_{ref}} - \sqrt{S_{THz}}\ . \tag{S2.12}$$

Since the sign of the time domain signal is irrelevant and $E_{THz} \propto \Gamma$, we obtain the equation shown in Fig. 1d of the main manuscript.

$$E_{THz} \propto \sqrt{S_{ref}} - \sqrt{S_{THz}}. \tag{S2.13}$$

Here, the proportionality relationship, instead of an equality, is sufficient as we rely on normalized spectral components to calculate changes in the complex dielectric function of a material.

3. Multilayer method for evaluation of THz transmission

The transmission of the THz field through a photoexcited semiconductor is related to the dynamics and the transport of photocarriers. In bulk Si, photocarrier transport is well described by the Drude model. Moreover, the electron mobility is three times larger than the hole mobility; therefore it is assumed that charge transport is dominated by electrons[4]. Based on this assumption, the dielectric constant of Si, $\epsilon(\omega, z, t)$, can be expressed as:

$$\epsilon(\omega, z, t) = \epsilon_r + \frac{i}{\omega\epsilon_0}\sigma(\omega, z, t) = \epsilon_r + \frac{i}{\omega\epsilon_0}\frac{N(z,t)e^2\tau_s\big(N(z,t)\big)}{m^*\left(1 - i\omega\tau_s\big(N(z,t)\big)\right)}, \tag{S3.1}$$

where ω is the THz angular frequency, z is the distance along the THz field propagation, t is time, $\epsilon_r = 11.72$ is the relative real part of the permittivity for Si at room temperature[5], $\epsilon_0 = 8.85 \times 10^{-12}$ F m^{-1} is the free-space permittivity, $\sigma(\omega, z, t)$ is the complex conductivity, $m^* = 0.2 \times 9.11 \times 10^{-31}$ kg is the electron effective mass[4], e is the elementary charge, and $N(z, t)$ is the carrier density. The carrier density-dependent scattering time, $\tau_s\big(N(z, t)\big)$, is expressed as:

$$\tau_s = \tau_s\big(N(z,t)\big) = \tau_0\left(1 + \sqrt{\frac{N(z,t)}{N_{ref}}}\right)^{-1}, \tag{S3.2}$$

where $\tau_0 = 190$ fs is the initial scattering time, and phenomenological parameter $N_{ref} = 10^{17}$ cm^{-3} [4]. The corresponding THz power absorption coefficient can be expressed as:

$$\alpha_{THz}(\omega, z, t) = \frac{2\omega}{c} Im\left(\sqrt{\epsilon(\omega, z, t)}\right), \tag{S3.3}$$

where c is the speed of light in vacuum. For a uniformly excited sample, the THz field transmission $T(\omega, t)$ can be expressed using the Beer-Lambert law as[6]:

$$T(\omega, z, t) = e^{-\alpha_{THz}(\omega,z,t)d/2}. \tag{S3.4}$$

The spatial distribution of the photocarriers is not uniform upon injection as the optical pump power decreases exponentially within the sample and the photocarrier distribution is expected to change at early times after the injection due to diffusion. The multilayer method has been proven to be an accurate method to evaluate the transmission over non-uniformly distributed carriers in photoexcited samples[7]. This approach considers the photoexcited sample to consist of several layers of identical thickness where the dielectric permittivity $\epsilon(\omega, z, t)$ is constant over the considered layer. Figure S2 illustrates the partition of the photocarrier distribution into several layers. The photocarrier density in the p^{th} layer is

$$N(z = pd, t = 0) = N_0 e^{-(p-1)\alpha_{pump}d} \approx N_0 e^{-\alpha_{pump}z}, \tag{S3.5}$$

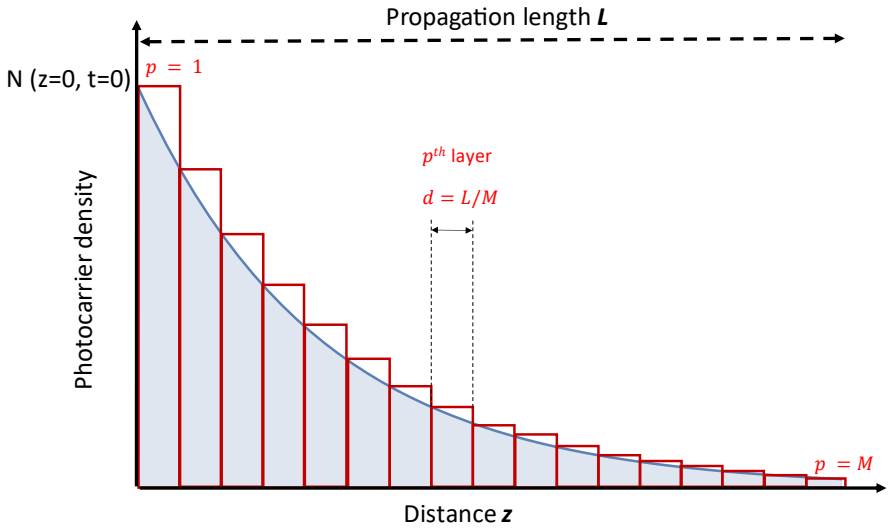

Figure S2. Spatial distribution of carriers upon optical injection. The pump propagation distance is divided in M layers of equal thickness d where permittivity is assumed constant.

where $\alpha_{pump} = 30.2$ cm^{-1} for our pump wavelength of 1030 nm[8], and $d = L/M$ is the thickness of a single layer. L is the total length of the sample and M is the total number of layers considered. The total THz field transmission over all layers can be expressed as the product of the THz transmission over all layers

$$T_{total}(\omega, z, t) = \prod_{p=1}^{M} e^{-\alpha_{THz}^{(p)}(\omega,z,t)d/2}, \tag{S3.6}$$

where $\alpha_{THz}^{(p)}(\omega, z, t)$ is the THz absorption of the p^{th} layer. The scattering time τ_s is assumed to be carrier density-dependent following Eq. 3.2. In this work, the value $M = 60$ was used for all simulations and corresponds to $d = 15$ µm. The derived expression of the transmission in Eq. 3.6 is used to evaluate the time-dependent transmission once the photocarrier dynamics over each layer are obtained.

3.1. Photocarrier dynamics and spatial distribution

The equation governing free- and trapped-carrier dynamics is given by the carrier rate equation in one-dimension expressed as[9–12]:

$$\frac{dN(z,t)}{dt} = G(t) + D(N(z,t))\frac{d^2N(z,t)}{dz^2} - \frac{N(z,t)}{\tau_{eff}(t)} \tag{S3.7}$$

$$\frac{dN_{trap}(z,t)}{dt} = \frac{-N_{trap}(z,t) + N(z,t)}{\tau_{eff}(t)} \tag{S3.8}$$

where $N(z,t)$ is the density of free carriers, $G(t)$ is a photocarrier source function that generates photocarriers into the system at a rate of 50 kHz, $D(N(z,t))$ is the carrier density-dependent diffusion coefficient, $\tau_{eff}(t)$ is the trapped carrier density-dependent recombination time[12], and $N_{trap}(z,t)$ is the density of trapped photocarriers[13]. The trap-assisted recombination time is of the form:

$$\tau_{eff}(t) = \tau_R \Big/ \left(1 - \frac{N_{trap}(z,t)}{N_{trap}^{max}}\right), \tag{S3.9}$$

where $\tau_R = 1/(\tau_{SRH}^{-1} + \tau_{rad}^{-1} + \tau_{Auger}^{-1})$ considers Shockley-Read-Hall (τ_{SRH}), radiative (τ_{rad}), and Auger (τ_{Auger}) recombination times [12], and N_{trap}^{max} is the density of available traps[13]. Equations 7 and 8 assume a uniform distribution of photocarriers in the plane of incidence of the pump beam. At early times after injection, the spatial distribution of photocarriers is expected to follow the exponential decay $N(z,t) = N(0,t)e^{-\alpha_{pump}z}$ assuming every pump photon generates an electron-hole pair. This inhomogeneous distribution is important in evaluating the total THz transmission as the penetration depth of the pump pulse $\alpha_{pump}^{-1} = 0.33$ mm is small compared to the optical propagation length of 0.9 mm. Moreover, the Si sample is periodically injected every 20 µs. By considering that photocarrier recombination is larger than the pump period, the diffusion length $L_D = \sqrt{D\tau_{decay}} = 0.26$ mm is smaller than the penetration depth. This condition entails two important consequences: the first is that of a significant impact of diffusion in the overall photocarrier dynamics, and hence on the accumulation of carriers upon successive injection, and the second implication is related to a modification of the spatial distribution of photocarriers with time as carriers diffuse in all directions. In both instances, solving Eq. 3.7 requires an accurate description of the

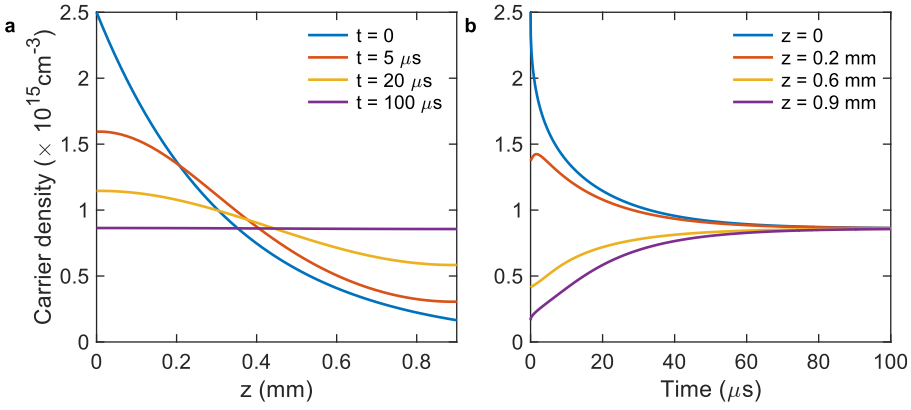

Figure S3. Time-varying carrier distribution with diffusion only. (a) Spatial distribution of photocarrier density at different points in time, (b) photocarrier dynamics at different points in space. Parameters considered are $N_d(z = 0, t = 0) = 2.5 \times 10^{15}$ cm^3, $D = 38$ cm^2/s, and $\alpha_{pump} = 30.2$ cm^{-1}.

spatial distribution of photocarriers at all times t. Previous pump-probe experiments address this issue by considering that photocarriers keep an exponential decay distribution over the probing duration[10,14]. This approximation is valid when the probing duration (a few hundred picoseconds) is very small compared to the recombination time. However, in the present case of bulk Si, the microsecond to millisecond time scale of carrier dynamics is of the same order of magnitude as the recombination time in bulk Si, and hence strengthens the need for proper modeling of $N(z, t > 0)$.

From the exponential distribution at $t = 0$, we approximate the second derivative in the diffusion term in Eq. 3.7 at a given point in space (z_i) and time (t_j) with the help of central difference approximations from neighboring carrier densities ($N(z_{i+1}, t_j)$ and $N(z_{i-1}, t_j)$).

$$\frac{d^2N(z,t)}{dz^2} = \frac{N(z_{i+1},t_j) + N(z_{i-1},t_j) - 2N(z_i,t_j)}{dz^2}. \tag{S3.10}$$

Figure S3a illustrates the spatial distribution of photocarriers following an injection of 2.5×10^{15} cm^{-3} carriers when calculating diffusion effects in this manner. The diffusion coefficient $D = 38$ cm^2 s^{-1} (for initial scattering time $\tau_0 = 190$ fs at room temperature[4]) is kept fixed in Fig. S3a, but in reality is proportional to the carrier-density dependent scattering time described in Eq. 3.2. The calculation results found in Fig. 3 of the main manuscript and Fig. S4 utilize this carrier dependent diffusion coefficient $D\big(N(z,t)\big) = \tau_s\big(N(z,t)\big)k_BT/m^*$, where k_B is the Boltzmann constant and $T = 300$ K. At $t = 0$, the photocarrier distribution corresponds to an exponential decay as expected from the pump energy absorption in the sample. As time increases, this spatial distribution evolves from an exponential decay towards a uniform distribution over the entire sample thickness. Figure S3b shows the corresponding photocarrier dynamics resulting from diffusion alone at various points in space throughout the 0.9 mm thick wafer. It can be seen that carrier density at the front interface ($z = 0$) decreases rapidly shortly after excitation. On the other hand, the photocarrier density at the rear interface increases with time due to carriers diffusing from the front interface. The dynamics reach equilibrium at ~100 µs where carriers are uniformly distributed, and their density remains constant with time.

3.2. Photocarrier dynamics and time-varying transmission

To evaluate the carrier dynamics given by Eqs. 7 and 8 over time, we use a split-step method between carrier diffusion and recombination over time steps of 5 ns and spatial steps of 15 µm. For each point in time and space, the carrier-dependent dielectric function (Eq. 3.1), total THz transmittance (Eq. 3.6), and recombination time (Eq. 3.9) are calculated. The input parameters for the simulation results in Fig. 3 of the

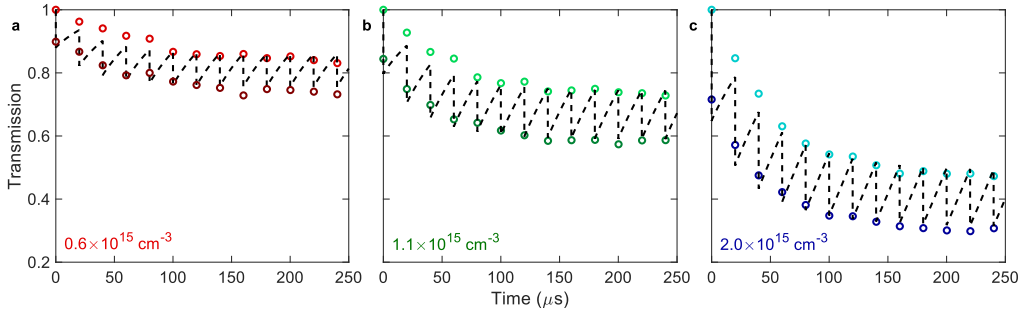

Figure S4. Time-varying THz transmission. The peak of the THz transient as the pump pulses arrive before (dark circles) and after (light circles) the THz pulse for carrier densities of a) 0.6, b) 1.1, and c) 2×10^{15} cm^{-3}. The black dashed lines represent the results from our theoretical analysis at $\omega = 0.9$ THz with the input parameters $\tau_R = 30$ µs, $N_{trap}^{max} = 6\times10^{11}$ cm^{-3}.

main manuscript are $\omega = 0.9$ THz (peak THz frequency in our experiments), $\tau_R = 30$ µs, $N_{trap}^{max} = 6{\times}10^{11}$ cm^{-3}. We use N_0, τ_R, and N_{trap}^{max} as fitting parameters for the experimental data. Low-doped silicon has an initial recombination time τ_R on the order of tens of microseconds[12], and the number of available traps should be much less than the injected number of carriers in a single optical pulse[13]. The values we have used for our simulations are well within these constraints.

Here, $G(t)$ injects the carrier distribution described in Eq. 3.5 every 20 µs. This periodic pumping is relaxed by carrier recombination and the resulting dynamics are that of an accumulation of photocarriers in the conduction band over time. Figure S4 displays the corresponding THz transmission evaluated at the peak frequency of the THz field amplitude considering $M = 60$ layers (15 µm step size) for the three injected carrier densities considered in our experiments (Fig. 3 of the main manuscript). To calculate the theoretical THz amplitude transmission spectrum, our calculations are repeated for frequencies within the bandwidth of the THz pulse (inset Fig. 1d of the main manuscript). The numerical simulations are in good agreement with experimental results.

References

1. Jiang, Z. & Zhang, X.-C. Electro-optic measurement of THz field pulses with a chirped optical beam. *Appl. Phys. Lett.* **72**, 1945–1947 (1998).
2. Hebling, J., Yeh, K.-L., Hoffmann, M. C., Bartal, B. & Nelson, K. A. Generation of high-power terahertz pulses by tilted-pulse-front excitation and their application possibilities. *JOSA B* **25**, B6–B19 (2008).
3. Blanchard, F. *et al.* Generation of 1.5 µJ single-cycle terahertz pulses by optical rectification from a large aperture ZnTe crystal. *Opt. Express* **15**, 13212–13220 (2007).
4. Jacoboni, C., Canali, C., Ottaviani, G. & Alberigi Quaranta, A. A review of some charge transport properties of silicon. *Solid-State Electron.* **20**, 77–89 (1977).
5. Krupka, J. *et al.* Measurements of Permittivity, Dielectric Loss Tangent, and Resistivity of Float-Zone Silicon at Microwave Frequencies. *IEEE Trans. Microw. Theory Tech.* **54**, 3995–4001 (2006).
6. Andorn, M. & Bar-Eli, K. H. Optical Bleaching and Deviations from Beer—Lambert's Law of Solutions Illuminated by a Ruby Laser. II. Sodium—Propylenediamine Solutions. *J. Chem. Phys.* **55**, 5017–5020 (1971).
7. Matsuzaki, H. *et al.* Photocarrier dynamics in anatase TiO2 investigated by pump-probe absorption spectroscopy. *J. Appl. Phys.* **115**, 053514 (2014).
8. Green, M. A. Self-consistent optical parameters of intrinsic silicon at 300K including temperature coefficients. *Sol. Energy Mater. Sol. Cells* **92**, 1305–1310 (2008).
9. *Semiconductor Physical Electronics*. (Springer, 2006). doi:10.1007/0-387-37766-2.
10. Zakar, A. *et al.* Carrier dynamics and surface vibration-assisted Auger recombination in porous silicon. *Phys. Rev. B* **97**, 155203 (2018).
11. He, W., Wu, R., Yurkevich, I. V., Canham, L. T. & Kaplan, A. Reconstructing charge-carrier dynamics in porous silicon membranes from time-resolved interferometric measurements. *Sci. Rep.* **8**, 17172 (2018).
12. Schroder, D. K. Carrier lifetimes in silicon. *IEEE Trans. Electron Devices* **44**, 160–170 (1997).
13. Yokoyama, K., Lord, J. S., Miao, J., Murahari, P. & Drew, A. J. Photoexcited Muon Spin Spectroscopy: A New Method for Measuring Excess Carrier Lifetime in Bulk Silicon. *Phys. Rev. Lett.* **119**, 226601 (2017).
14. Němec, H. *et al.* Ultrafast carrier dynamics in Br+-bombarded InP studied by time-resolved terahertz spectroscopy. *Phys. Rev. B* **78**, 235206 (2008).

Chapter 5

Optical fibers as a tool to achieve broadband THz spectroscopy

As mentioned in chapter 2, when generating THz waves through nonlinear effects in a $\chi^{(2)}$ crystal, the spectral bandwidth of the NIR pulse used for nonlinear frequency conversion plays a large role in the maximum attainable THz spectral bandwidth. Consequently, the choice of ultrafast source for the time-resolved THz system becomes crucial. For instance, a Gaussian laser pulse with duration of 300 fs has a spectral bandwidth of ∼1.5 THz. To even be given the opportunity to generate and detect high frequency THz pulses (>3 THz) with nonlinear crystals, a laser delivering sub-100 fs NIR pulses is therefore required, which carries a significant financial burden. The initial cost of such a source can be upwards of $100k and amplified ultrafast lasers require additional daily operational costs to maintain the proper temperature inside the laser head. Instead of throwing money at the problem and buying a new source to overcome spectral bandwidth limitations, we proposed to use optical fibers, alleviating the financial requirement of a new ultrafast source without sacrificing THz bandwidth or sensitivity.

5.1 NIR pulse shaping with silica fibers

To generate the frequency content required for broadband THz generation, we can utilize nonlinear propagation in a standard silica fiber. In this case, self-phase modulation (SPM) as described in section 2.1.2, is the dominant nonlinear effect responsible for the generation of new NIR frequencies and can broaden the spectrum from a width of a few THz to >6 THz with only nanojoules of NIR pulse energy and after only a few centimeters of propagation in the fiber. However, a pulse with a central wavelength near 1 μm undergoes positive dispersion in a standard silica fiber, which we must compensate for to achieve the highest peak power possible. A high peak power will enhance nonlinear effects in the crystal for optimal THz generation. In fact, with the additional frequency content gained due to SPM, even shorter pulse durations are achievable. Recalling the time-bandwidth product of a transform-limited Gaussian pulse $\Delta\tau\Delta\omega = 0.88\pi$, an increased spectral bandwidth $\Delta\omega$ will allow a lower pulse duration $\Delta\tau$. A short pulse duration is crucial not only for enhanced nonlinear effects for THz generation, but also to enable the detection of high THz frequencies through EOS.

There are several ways to compensate for dispersion, otherwise known as pulse compression. One may use angular dispersion from glass prisms or diffraction gratings. This allows high and low frequency components of the pulse to experience unique optical path lengths,

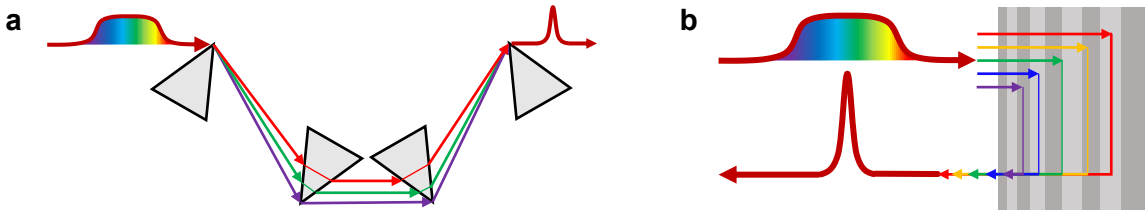

Figure 5.1: a) Dispersion compensation scheme relying on dispersive prisms. An initially chirped pulse is incident on a prism, spatially separating the frequency components of the pulse, lower frequencies (red) having longer optical propagation lengths than high frequency components (violet), analogous to negative GDD. b) Dispersion compensation technique relying on a chirped mirror consisting of dielectric slabs of different indices and thickness, which are portrayed by grey slab of different shades. In each case, a Fourier transform limited pulse duration is the result.

as shown in Fig. 5.1a. With this configuration, the group delay dispersion (GDD) is set by the dispersive properties of the prisms and the distance between prisms. In the situation where a large amount of dispersion needs to be compensated for, this scheme can become quite large as the distance between prisms needs to be increased to produce higher magnitude negative GDD (or specialty highly dispersive prisms need to be manufactured to keep it compact). The same argument applies to the configuration implementing gratings instead of prisms, which is the same as that shown in Fig. 5.1a with gratings replacing the prisms. Moreover, in the situation where one requires high transmission through the pulse compressor, it is impractical to use components that lose light to Fresnel reflection (prisms) or higher diffraction orders (gratings).

A more straightforward and compact manner of dispersion compensation is the implementation of chirped mirrors [94]. These specialty mirrors consist of a stack of dielectrics with alternating refractive index and varying layer thickness. Here, instead of utilizing angular dispersion, each spectral component will penetrate the mirror to a unique depth to experience a different GDD, as schematically drawn in Fig. 5.1b. The choice and thickness of materials used to fabricate chirped mirrors determines the GDD and operating bandwidth and the number of reflections off the chirped mirror determines the total GDD of the pulse compressor. The high reflectivity of these mirrors (typically >99%) maximizes transmission through the pulse compression scheme, making them an ideal candidate for NIR pulse shaping. In the time domain, after dispersion compensation, this permits all frequency components to arrive at the same time, otherwise known as a Fourier transform limited pulse.

A combination of optical fiber and dispersion compensation technique is therefore a valid way of altering a NIR pulse that initially lacked the requirements for broadband THz generation and detection. However, as NIR pulse energies increase into the microjoule regime, silica fibers are no longer a viable option as the fiber can burn when exposed to extremely high intensities. This approach is therefore inappropriate for amplified ultrafast sources. A different kind of fiber, however, can handle intense optical fields such that we can achieve similar results.

5.2 NIR pulse shaping with hollow-core photonic crystal fibers

Hollow-core photonic crystal fibers (HCPCFs) are a specialty fiber that possess unique advantages compared to standard silica fibers [95]. The name is rather self-explanatory: instead of a solid core, the light is guided through a hollow core surrounded by a photonic crystal structure made of thin-walled glass capillaries. These fibers use an anti-resonant guiding mechanism to transmit the light through the fiber instead of total internal reflection. The thin walls of the capillaries surrounding the hollow core act as Fabry-Pérot resonators and therefore possess the same transmission and reflection properties. Specific frequencies can be transmitted through the resonator (i.e. towards the cladding of the fiber), reflecting the remaining anti-resonant frequencies and thereby confining them within the core [96]. As a result, the thickness of the walls surrounding the core plays a key role in the transmissive properties of the fiber. A cross-section of the HCPCF with kagomé design surrounding the core used in this work is shown in Fig. 5.2. Fun fact: the kagomé lattice [97], consisting of corner-sharing triangles, is inspired by Japanese basket patterns. Placing this fiber in a gas cell and filling the fiber with a gas allows us to tune linear and nonlinear effects; the species and pressure of the gas in the core and the waveguiding

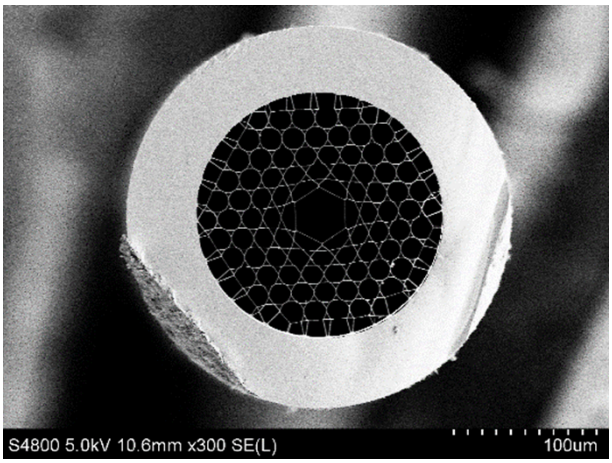

Figure 5.2: Cross-section of kagomé HCPCF measure with scanning electron microscope. The white areas represent glass and dark spaces represent air.

properties of the HCPCF. This allows phase-matched nonlinear effects to occur over long propagation lengths [98, 99]. The only downside to these fibers is that their implementation requires a custom gas cell and the fiber cannot be tightly coiled, occupying valuable space on an optical table. The benefits of these kinds of fibers, however, heavily outweigh these technical drawbacks:

1. The light propagating in the fiber is not subjected to the losses associated with the material of the fiber core. Silica, for example, does not transmit light with wavelengths beyond 2.2 μm while HCPCFs are capable of generating and transmitting frequencies from the UV to the mid IR regimes [100, 101, 102, 103].

2. The selection of gas species and gas pressure inside the fiber tune nonlinear and linear properties of the fiber. Not only can this permit supercontinuum generation over large bandwidths [104], it also enables self-compression such that the output pulse has a duration of only a few femtoseconds [105].

3. Finally, they achieve single-mode guidance with a core diameter >6 times greater than solid core fibers and do not experience losses at the input due to Fresnel reflection, allowing higher throughput at higher pulses energies [106]. Among the many applications of these fibers, NIR pulse shaping via gas pressure and input pulse energy tuning to enable broadband THz generation and detection is among them [35, 107].

This chapter contains two articles in their published forms. The first one is titled "Compact, low-cost, and broadband terahertz time-domain spectrometer" and was published in *Applied Optics* [34], and presented at *SPIE Photonics West* in 2023 [108]. In this work, we built a time-domain THz spectrometer relying on a modest and compact NIR ultrafast oscillator source (5 nJ pulse energy). We then built and mounted a device that we call a peak field booster (PFB) onto the laser head. The PFB consists of a short silica polarization-maintaining fiber and chirped mirror pair and was used to render the NIR pulse suitable for broadband THz generation and detection. This module successfully spectrally broadened the NIR bandwidth from a few THz to ∼12 THz and compressed the pulse from a duration of 130 fs to 50 fs after 14 total reflections from the chirped mirrors (see Fig. 5.3). The high throughput through the fiber combined with a temporal compression ratio >2 yields a NIR

pulse with a higher peak electric field than the input pulse – hence the reason we call it the peak-field booster. As a result, the PFB in conjunction with custom GaP crystals to optimize phase matching conditions at high THz frequencies [109, 110, 111, 112], produced a THz time-domain spectrometer with 50 dB dynamic range, peaking at 3.5 THz, and extending to 6 THz. Current commercial THz systems relying on photoconductive antennas have a peak sensitivity below 1 THz. Our system, peaking at 3.5 THz, therefore fills a void in the THz spectrometer market. The entire time-resolved THz system, laser included, is built on a small breadboard (2'×3') that is mounted on a trolley for easy transportation; a photograph of the system is shown in Fig. 5.4. To highlight this feature, we wheeled the system to another lab that was well-equipped for the spectroscopy of gases described in [113] and performed spectroscopy of low volumes of water vapor. This work presented a practical and cost-effective way of performing broadband and sensitive THz spectroscopy with a low-energy ultrafast source. Once again, the versatility of optical fibers has unlocked a key functionality of THz spectroscopy.

The second publication is titled "Optical pulse structuring in gas-filled hollow-core kagomé PCF for generation and detection of phase-locked multi-THz pulses" and was published

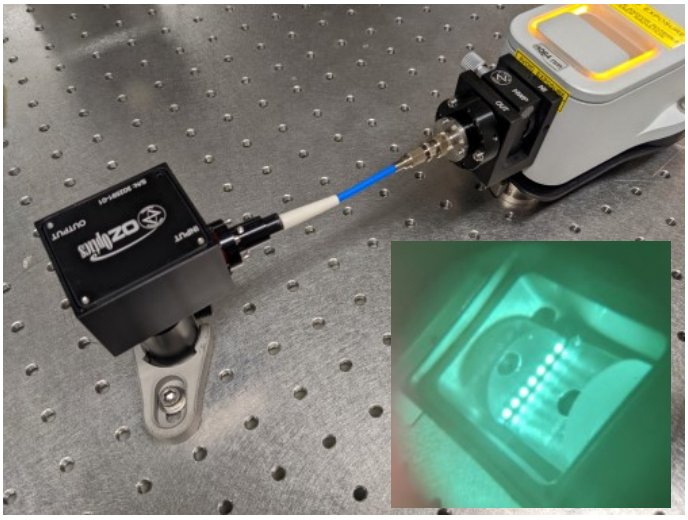

Figure 5.3: Photograph of the peak-field booster mounted on the laser head. (inset) Photograph taken through an IR-viewer of the beam transmitted through chirped mirror pair after 14 total reflections.

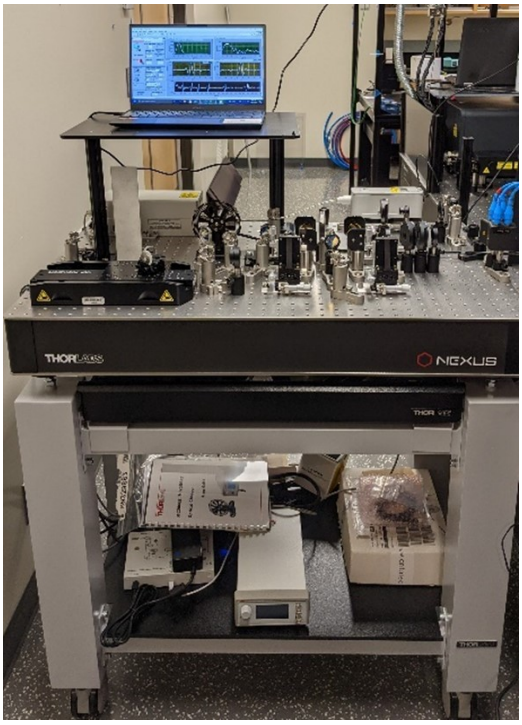

Figure 5.4: Photograph of the compact and portable time-resolved THz spectrometer mounted on the trolley.

in *Optical Materials Express* in 2019 [35]. Here, we used an amplified NIR optical source delivering pulse energies of a few microjoules, 50 cm of a kagomé HCPCF filled with 13 bar of argon gas, a chirped mirror pair, and GaSe crystals to generate and detect THz pulses up to 20 THz. By increasing the pulse energy injected into the fiber, we gained the NIR frequency content required to generate such high THz frequencies and compressed the pulse to short enough duration with the chirped mirror pair to resolve them with EOS. The birefringence of the GaSe crystals allowed us to use angle tuning and achieve phase-matching at high THz frequencies [114]. This work demonstrated the versatility of implementing a HCPCF and chirped mirror pair into a THz system employing an amplified ultrafast source with limited spectral bandwidth.

Research Article Vol. 62, No. 15 / 20 May 2023 / Applied Optics 4097

applied optics

Compact, low-cost, and broadband terahertz time-domain spectrometer

Nicolas Couture,[1] Jakob Schlosser,[1] Akif Ahmed,[2] Mamoun Wahbeh,[2] Garland Best,[2] Angela Gamouras,[1,3] and Jean-Michel Ménard[1,3,*]

[1]Department of Physics, University of Ottawa, Ottawa, Ontario K1N 6N5, Canada
[2]OZ Optics Limited, Ottawa, Ontario K0A 1L0, Canada
[3]National Research Council Canada, Ottawa, Ontario K1A 0R6, Canada
*jean-michel.menard@uottawa.ca

Received 15 February 2023; revised 23 April 2023; accepted 1 May 2023; posted 2 May 2023; published 18 May 2023

Terahertz time-domain spectroscopy (THz-TDS) is a powerful technique that enables the characterization of a large range of bulk materials, devices, and products. Although this technique has been increasingly used in research and industry, the standard THz-TDS configuration relying on the use of a near-infrared (NIR) laser source remains experimentally complex and relatively costly, impeding its availability to those without the expertise to build a high-performance setup based on nonlinear optics or without the financial means to acquire a commercial unit. Broadband THz-TDS systems require an even larger financial investment, primarily because the generation and detection of spectral components exceeding 3 THz typically need an ultrafast NIR source delivering sub-100-fs pulses. Such an ultrafast source can be bulky and cost upwards of $100,000. Here, we present a broadband, compact, and portable THz-TDS system comprising three modules that allow for the implementation of a single low-cost ultrafast laser, hence significantly decreasing the overall cost of the system. In the first module, the output laser pulses are spectrally broadened through nonlinear propagation in a polarization-maintaining optical fiber and then temporally compressed to achieve a higher peak power. The other two modules utilize thick nonlinear crystals with periodically patterned surfaces that diffract NIR pulses and optimize the efficiency of THz generation and detection processes by enabling a noncollinear beam geometry. Phase-matching conditions in the nonlinear crystals are controlled by the period of the gratings to gain access to a large spectral THz bandwidth. The whole system, combining these three modules, provides access to a THz spectrum peaking at 3.5 THz and extending beyond 6 THz with a maximum dynamic range of 50 dB for time-resolved spectroscopy applications. We demonstrate the functionality of this configuration by performing THz spectroscopy measurements of water vapor contained within a closed cell. Our compact system design paves the way towards a high-performance, yet cost-effective, THz-TDS system that can be readily used in academia and industry.

https://doi.org/10.1364/AO.486938

1. INTRODUCTION

The far-infrared region of the electromagnetic spectrum, broadly corresponding to optical wavelengths between 10 μm and 1000 μm and known as the terahertz (THz) band, is a rich area of research and development. THz radiation has a nonionizing photon energy offering new opportunities for noninvasive optical characterization of products and materials [1,2]. Notably, it is used to evaluate drug quality [3–5], detect structural flaws [6], identify organic and nonorganic contaminants in foods [7–9], and alert on the presence of bacteria and viruses [10–12]. These applications take advantage of unique properties of THz radiation: it can be transmitted through cardboards, polymers, and other materials opaque in the visible region. Additionally, THz radiation interacts with a large range of molecular vibrations, thereby enabling the detection and identification of many different compounds. THz time-domain spectroscopy (THz-TDS) is a characterization technique that relies on the generation and detection of phase-locked THz pulses. Compared to other optical characterization techniques that only record variations in optical intensity, THz-TDS has the advantage of extracting both amplitude and phase information of a THz pulse while mapping its full oscillating electric field. When a THz pulse is transmitted through or reflected at a surface, THz-TDS can directly extract the refractive index and absorption spectrum of that medium [2]. As THz spectroscopy and technologies offer such distinctive specifications, it complements, rather than competes with, other characterization techniques based on spectrometers, mass spectrometry, and Raman spectroscopy. Due to their scientific and practical significance, THz technologies and devices are in increasingly high demand and are a fast-growing research field in photonics.

1559-128X/23/154097-05 Journal © 2023 Optica Publishing Group

Nonetheless, access to a broadband, sensitive, and affordable THz spectrometer is still a major hurdle to many applications in industrial, government, and academic laboratory settings. Some commercial THz-TDS systems that rely on photoconductive antennas (PCAs) feature a high dynamic range over a large spectral range, in part due to the ability to average over thousands of THz waveforms using rapid scanning methods such as asynchronous optical sampling [13]. THz systems employing PCAs typically have a peak sensitivity at frequencies below 1 THz [14], but can still reach, through averaging, an acceptable signal-to-noise ratio for particular spectroscopy applications at frequencies exceeding 4 THz. Other THz systems based on optical rectification in semiconductor crystals [15,16] can routinely generate and detect THz radiation at frequencies up to ∼3 THz. However, to generate higher THz frequency components, a near-infrared (NIR) laser source supporting a spectral bandwidth exceeding 3 THz is required. This condition corresponds to a < 100 fs pulse duration, which can only be delivered by high-end ultrafast systems. An alternative option to accessing broadband THz radiation consists of employing an independent optical module that broadens the laser spectrum in a nonlinear medium and recompresses the pulses with dispersion compensation optics [17,18]. We present such a module, consisting of a fiber and a chirped mirror pair, which significantly decreases the pulse duration while maintaining low-injection loss, hence boosting the peak field of the NIR laser pulses. Another major factor limiting the THz bandwidth is the nature and thickness of the crystals used for nonlinear generation and detection. Semiconductors such as ZnTe, GaAs, and $LiNbO_3$ have phase-matching conditions and phonon absorption tails preventing efficient THz generation above 3 THz. Previous work has demonstrated that a GaP crystal can be used to access larger THz frequencies [17], but a relatively thin crystal was required to achieve a broad THz bandwidth. Thick crystals are more desirable to increase THz generation and detection efficiencies since they enable long nonlinear interaction lengths. However, phase mismatch then becomes a dominant factor, and only those THz frequencies satisfying phase-matching conditions can be efficiently generated or detected. Here, we use surface phase gratings etched onto thick GaP crystals to overcome this limitation [19]. This configuration induces a tilted-pulse front inside the generation and detection crystals to increase the nonlinear interaction length while also providing access to a large THz spectral bandwidth [20,21]. The combination of the three modules allows the THz-TDS system to cover a large THz spectral bandwidth of >4 THz (FWHM) at a peak frequency of 3.5 THz. This THz-TDS system is, to our knowledge, unique in terms of its spectral properties combined with a simple and compact design. This article is ordered as follows: first, we demonstrate how the first module, referred to as the peak field booster (PFB), improves the performance of a fiber–laser source to yield suitable pulses to generate and detect broadband THz radiation. Then, we investigate the performance of the THz-TDS system employing GaP crystals with phase gratings on their surfaces by comparing to THz generation and detection results obtained with the same setup using standard nonpatterned GaP crystals. Finally, we demonstrate the functionality of our THz-TDS by performing spectroscopy of water vapor.

2. EXPERIMENT

A schematic of the THz-TDS scheme described in this work is shown in Fig. 1. To realize broadband THz-TDS, we employ a low-energy (5 nJ) femtosecond fiber laser oscillator delivering 130 fs pulses at a repetition rate of 40 MHz centered at a wavelength of 1064 nm (Ekspla FF200) and a PFB mounted directly onto the laser head. In a THz-TDS setup, spectral broadening of the incident NIR pulses allows the generation of higher THz frequencies, while temporal compression of these pulses ensures more efficient electro-optic sampling (EOS) detection [22]. Nonlinear propagation in a 10-cm-long polarization-maintaining fiber (PMF) with a 6 μm core diameter (OZ Optics PMF-980-6/125-0.25-L) broadens the NIR spectral bandwidth from 24 nm to 40 nm. As shown in Fig. 2(a), these bandwidths correspond to roughly 6 THz and 12 THz (FWHM) in optical frequency, respectively. Multiple reflections (14 in total) on the chirped mirror pair (CMP, Edmund Optics #12-328) provide a total group delay dispersion of -2800 fs^2 and compress the pulse from 130 fs to 50 fs [Fig. 2(b)]. This compression combined with a relatively high power transmission (78%) through the PFB yields an increase of the NIR pulse peak field by a factor of 2. A 1-mm-thick GaP crystal is used for THz generation, and a 2-mm-thick GaP crystal is used for detection through EOS. With a NIR wavelength of 1064 nm, phase-matching conditions and a second-order nonlinear process in a standard GaP window yield the production and detection of radiation at 1.5 THz [23,24]. Here, a phase grating is etched onto the surface of these two crystals via inductively coupled plasma

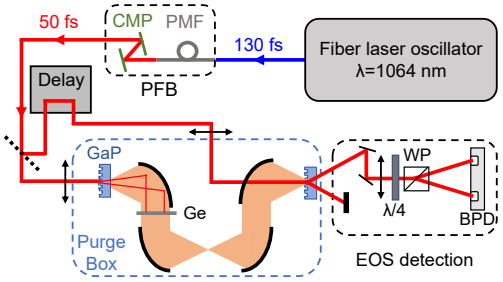

Fig. 1. Schematic of the compact and broadband THz-TDS system. A peak field booster (PFB) module, mounted to the output of a fiber laser oscillator (blue line), contains a polarization-maintaining fiber (PMF) to broaden the spectrum and a chirped mirror pair (CMP) to temporally compress the pulse. The output of the PFB is sent to a THz-TDS scheme relying on GaP crystals with phase gratings etched on their surfaces to generate and detect THz radiation. A germanium (Ge) wafer in the THz beam blocks the remaining NIR laser radiation after THz generation. THz detection is performed with electro-optic sampling (EOS) on one of the diffracted orders of the phase grating to achieve noncollinear phase matching and enhances sensitivity at frequencies >3 THz. This diffracted beam is collected with a periscope and then passed through a quarter-wave plate ($\lambda/4$) and Wollaston prism (WP) before being focused onto a pair of balanced photodiodes (BPDs) effectively monitoring the THz-induced change in polarization. The delay stage allows this process to be repeated for different temporal overlaps between the THz transient and the NIR pulse, allowing us to map out the full oscillating THz electric field via lock-in detection. A purge box filled with dry air removes atmospheric water vapor.

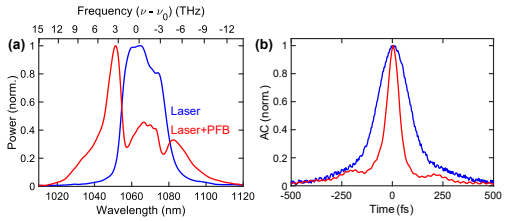

Fig. 2. (a) Spectra and (b) intensity autocorrelation (AC) traces of the pulses at the output of the ultrafast NIR source (blue line) and the PFB module (red line). The laser delivers 130 fs pulses carrying a 6 THz spectral bandwidth, which are spectrally broadened by the PFB to a 12 THz bandwidth and compressed to a 50 fs pulse duration. The high device throughput (only 22% loss in transmission) leads to an increase of the NIR pulse peak field by a factor of 2.

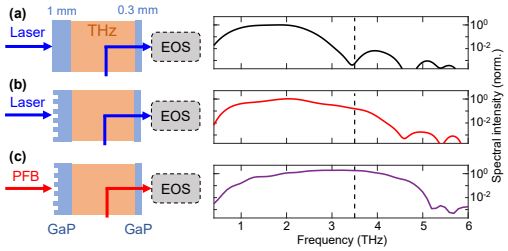

Fig. 3. Spectrum recorded by a THz-TDS system (plotted in log scale) using the direct laser output and (a) nonpatterned or (b) patterned 1-mm-thick GaP generation crystal. The grating on the surface of the generation crystal allows for nonlinear phase-matching conditions to be satisfied at higher THz frequencies, extending the spectrum beyond 4 THz. (c) THz spectrum measured with a setup incorporating both the PFB and the patterned 1-mm-thick GaP THz generation crystal. The spectrum extends beyond 5 THz, and the peak frequency shifts from 2 THz to 3.5 THz with the peak spectral intensity increasing by a factor of 2. In all three cases, the spectra are normalized to the maximum spectral intensity shown in (a), and a 0.3-mm-thick nonpatterned GaP crystal is used for detection to ensure a broadband detection window.

reactive ion etching, performed in-house, with a period of 1.635 μm corresponding to a 11.7° diffraction angle, allowing for noncollinear phase-matching conditions to be satisfied at 4 THz. The grating diffracts 85% of the incident NIR light in the first orders, whereas a mere 1.4% remains in the zeroth order, rendering the effect of the zeroth order NIR on the generated THz bandwidth negligible. Details related to the fabrication of the device are presented in [19]. This configuration mimics the titled-pulse-front generation scheme, commonly used for high-field THz generation in lithium niobate crystals [25–27], but without the complex beam geometry involving an external grating and a wedge-shaped nonlinear crystal. For EOS detection, a periscope collecting one of the grating diffraction orders is the only additional component needed when implementing a patterned detection crystal in the setup. Moreover, measuring one of the transmitted diffraction orders, instead of the zeroth order, leads to a polarization filtering effect at the back surface of the crystal resulting in an enhanced measurement sensitivity through a larger dynamic range [20,21]. The use of thick nonlinear crystals provides another advantage as it allows users to measure long EOS scanning ranges without recording parasitic THz echoes originating from multiple back reflections inside these crystals [28]. For the same reason, a thick (1 mm) Ge wafer is used as a spectral filter blocking the remaining NIR light after the THz generation crystal. As a result, an EOS scan of 30 ps can be performed before observing the first THz echo, yielding a spectral resolution of 33 GHz. The entire THz-TDS system, including the ultrafast source with the PFB, has the footprint of a 2′ × 3′ optical breadboard and is mounted on a trolley for easy transportation. This proof-of-concept setup allows for additional design modifications for further miniaturization of the system.

3. RESULTS AND DISCUSSION

We first investigate how the PFB and THz generation crystal with the periodically patterned surface can be combined to achieve a broad THz spectrum. For this experiment, a standard thin 0.3-mm-thick GaP crystal is used for EOS detection to provide access to a large THz bandwidth as we study the effect of the laser spectral bandwidth and different types of THz generation crystals. The measurements performed with the reference setup, shown in Fig. 3(a), rely on laser output pulses directly impinging onto a 1-mm-thick nonpatterned THz generation crystal. The resulting THz spectrum extends up to 3 THz, peaks at ∼2 THz, and has a bandwidth of 2 THz (FWHM). In a second version of this setup, a patterned GaP crystal is used for THz generation, instead of the nonpatterned crystal with same thickness. In this case, the THz spectrum is extended beyond 4 THz and the bandwidth is increased to 3 THz (FWHM) [Fig. 3(b)]. After inserting the PFB immediately after the laser source [Fig. 3(c)], we observe spectral components extending beyond 5 THz, a peak frequency shifting from 2 to 3.5 THz, and a bandwidth exceeding 4 THz (FWHM).

Figure 4 shows the effect of replacing the 0.3 mm nonpatterned THz detection crystal by the 2-mm-thick crystal with a phase grating in a configuration that already combines the PFB and patterned THz generation crystal. In this case, we observe a larger field amplitude in the time-domain THz signal, by a factor of 6, resulting in an overall increase in detected spectral amplitude, especially around 3.5 THz. The phase gratings on the two nonlinear crystals diffract the NIR beam and allow noncollinear phase-matching conditions to be satisfied at 4 THz, which considerably improves both THz generation and detection processes around that frequency. Notably, the signal at lower THz frequencies is not significantly reduced as the corresponding wavelengths intrinsically have longer nonlinear coherence lengths. Furthermore, a polarization filtering effect at the back surface of the detection crystal enhances the THz detection sensitivity over the full spectrum by effectively reducing the optical noise on the photodiodes [20,21]. Combining the three modules, we achieve a spectrum reaching up to ∼ 6 THz, with the peak frequency at 3.5 THz and a spectral bandwidth of >4 THz. Figure 4(c) shows a dynamic range exceeding 50 dB at 3.5 THz, which is more than 20 dB higher than the value measured with a thin detection crystal (purple line). We evaluate the dynamic range of the system by dividing the intensity spectrum

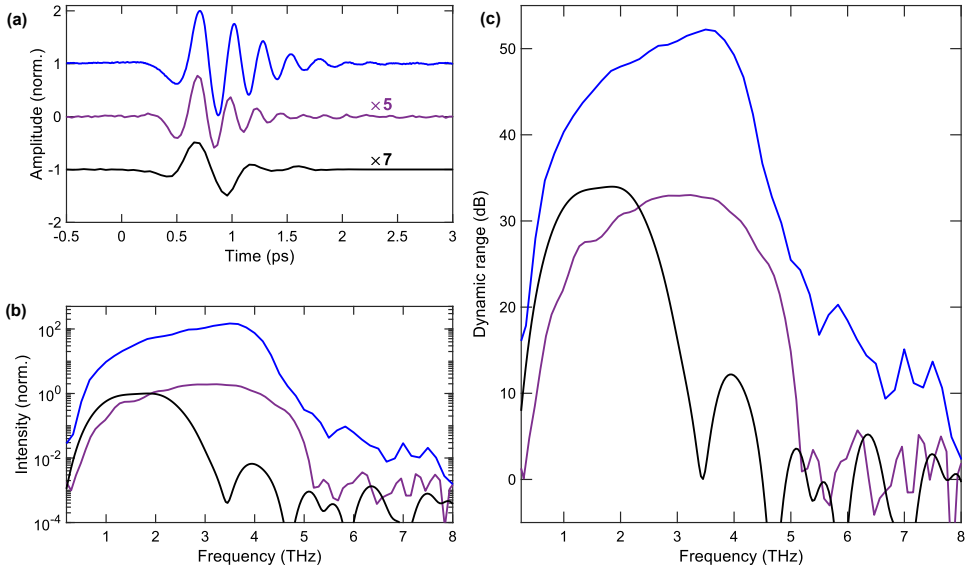

Fig. 4. (a) Time-domain signal and (b) spectral intensity measured with a setup using the PFB and the two thick patterned GaP crystals for THz generation (1 mm) and detection (2 mm) (blue line), a similar setup relying instead on a nonpatterned thin (0.3 mm) detection crystal (purple line), and a setup that is not relying on any of the three modules (black line). The spectral intensities are normalized to the peak of the black line. (c) Corresponding dynamic range achieved with each configuration.

by the noise floor. Our system's spectral coverage and sensitivity, related to its dynamic range, are comparable to those achieved with other THz-TDS systems relying on thin nonlinear crystals and a more complex optical source [29–31].

To demonstrate the spectroscopic capabilities of the system employing the three modules, time-resolved THz spectroscopy of a cell of water vapor is performed over a broad frequency range. The 3.8 cm by 2.5 cm by 2.5 cm cell has two external ports for gas injection and exhaust, and uses two input and output 10-μm-thick windows made of Zeonor, a cyclo olefin copolymer with high transparency in the THz region. The water vapor concentration is controlled and measured with a standard testing apparatus used to investigate gas sensing devices [32]. We achieve the desired concentration of water vapor in the cell by carefully adjusting the flow between two combined nitrogen gas lines, where one line is passed through a bubbler with water to reach a high vapor concentration. A reference THz time-domain waveform is recorded with a nitrogen-purged cell, allowing for the characterization of a cell containing 37% relative humidity (RH) [Fig. 5(a)]. These measurements were collected over a 30 ps time delay scanning range yielding a frequency resolution of 33 GHz. The corresponding measured absorption spectrum, which is in agreement with the transition intensity lines from the HITRAN database [33], is shown in Fig. 5.

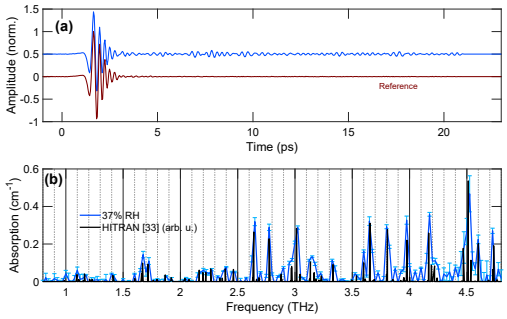

Fig. 5. (a) Recorded time-domain waveforms of the THz pulse passing through a 3.8-cm-long cell filled with water vapor at 37% RH (blue line), compared to a reference taken by purging the same cell with nitrogen (maroon line). The transients, normalized to the maximum field amplitude of the reference signal, are displayed with a vertical offset for clarity. In (b), the absorption spectrum of water vapor (blue line) is calculated from the Fourier transform of the waveforms in (a), possessing a frequency resolution of 33 GHz. Water vapor transition intensity lines (in arbitrary units) from the HITRAN database (black line) are superimposed on the experimental data. Error bars correspond to the standard deviation over three scans.

4. CONCLUSION

We demonstrate an easily transportable, broadband, and sensitive THz-TDS system relying on a cost-effective NIR source and a combination of three modules involving a PFB and two patterned nonlinear crystals. We show that the three respective components work together to ensure access to a broadband THz spectrum peaking at 3.5 THz and extending to a frequency range exceeding 6 THz. The system features a maximum dynamic range of 50 dB, which is approximately two orders of magnitude higher than a standard THz configuration relying

on the same laser source but without any of the three modules. Finally, the functionality of the system has been successfully tested for spectroscopic applications by performing broadband THz-TDS on a small volume of water vapor at 37% RH. Further technical development may still increase the measured dynamic range and scanning speed, potentially allowing our configuration to outperform THz characterization systems relying on high-end ultrafast laser systems. Our cost-effective and compact configuration is a major step towards enabling broader access to THz-TDS systems for broadband characterization of materials in research and manufacturing.

Funding. Natural Sciences and Engineering Research Council of Canada (ALLRP/556169-20); National Research Council Canada (JCEP).

Acknowledgment. The authors thank Wei Cui for insightful discussions. We acknowledge funding from the Natural Sciences and Engineering Research Council of Canada (NSERC) Alliance Program and Ontario Graduate Scholarship. We also acknowledge funding from the NRC-uOttawa Joint Centre for Extreme Photonics.

Disclosures. The authors declare no conflicts of interest.

Data availability. Data underlying the results presented in this paper are not publicly available at this time but may be obtained from the authors upon request.

REFERENCES

1. B. Ferguson and X.-C. Zhang, "Materials for terahertz science and technology," Nat. Mater. **1**, 26–33 (2002).
2. M. Tonouchi, "Cutting-edge terahertz technology," Nat. Photonics **1**, 97–105 (2007).
3. K. L. Nguyen, T. Friscić, G. M. Day, L. F. Gladden, and W. Jones, "Terahertz time-domain spectroscopy and the quantitative monitoring of mechanochemical cocrystal formation," Nat. Mater. **6**, 206–209 (2007).
4. J. A. Zeitler, P. F. Taday, D. A. Newnham, M. Pepper, K. C. Gordon, and T. Rades, "Terahertz pulsed spectroscopy and imaging in the pharmaceutical setting—a review," J. Pharm. Pharmacol. **59**, 209–223 (2007).
5. Y.-C. Shen, "Terahertz pulsed spectroscopy and imaging for pharmaceutical applications: a review," Int. J. Pharm. **417**, 48–60 (2011).
6. C. Jördens, M. Scheller, S. Wietzke, D. Romeike, C. Jansen, T. Zentgraf, K. Wiesauer, V. Reisecker, and M. Koch, "Terahertz spectroscopy to study the orientation of glass fibres in reinforced plastics," Compos. Sci. Technol. **70**, 472–477 (2010).
7. H. J. Shin, S.-W. Choi, and G. Ok, "Qualitative identification of food materials by complex refractive index mapping in the terahertz range," Food Chem. **245**, 282–288 (2018).
8. S. H. Baek, H. B. Lim, and H. S. Chun, "Detection of melamine in foods using terahertz time-domain spectroscopy," J. Agric. Food Chem. **62**, 5403–5407 (2014).
9. W. Liu, C. Liu, F. Chen, J. Yang, and L. Zheng, "Discrimination of transgenic soybean seeds by terahertz spectroscopy," Sci. Rep. **6**, 35799 (2016).
10. A. Mazhorova, A. Markov, A. Ng, R. Chinnappan, O. Skorobogata, M. Zourob, and M. Skorobogatiy, "Label-free bacteria detection using evanescent mode of a suspended core terahertz fiber," Opt. Express **20**, 5344–5355 (2012).
11. X. Yang, K. Yang, Y. Luo, and W. Fu, "Terahertz spectroscopy for bacterial detection: opportunities and challenges," Appl. Microbiol. Biotechnol. **100**, 5289–5299 (2016).
12. D.-K. Lee, J.-H. Kang, J. Kwon, J.-S. Lee, S. Lee, D. H. Woo, J. H. Kim, C.-S. Song, Q.-H. Park, and M. Seo, "Nano metamaterials for ultrasensitive Terahertz biosensing," Sci. Rep. **7**, 8146 (2017).
13. T. Yasui, E. Saneyoshi, and T. Araki, "Asynchronous optical sampling terahertz time-domain spectroscopy for ultrahigh spectral resolution and rapid data acquisition," Appl. Phys. Lett. **87**, 061101 (2005).
14. M. El Ghzaoui, S. Das, T. R. Lenka, and A. Biswas, eds., *Terahertz Wireless Communication Components and System Technologies* (Springer, 2022).
15. R. Huber, B. A. Schmid, R. A. Kaindl, and D. S. Chemla, "Femtosecond THz studies of intra-excitonic transitions," Phys. Status Solidi B **245**, 1041–1048 (2008).
16. A. Leitenstorfer, S. Hunsche, J. Shah, M. C. Nuss, and W. H. Knox, "Detectors and sources for ultrabroadband electro-optic sampling: experiment and theory," Appl. Phys. Lett. **74**, 1516–1518 (1999).
17. W. Cui, A. W. Schiff-Kearn, E. Zhang, N. Couture, F. Tani, D. Novoa, P. St.J. Russell, and J.-M. Ménard, "Broadband and tunable time-resolved THz system using argon-filled hollow-core photonic crystal fiber," APL Photon. **3**, 111301 (2018).
18. A. Halpin, N. Couture, and J.-M. Ménard, "Optical pulse structuring in gas-filled hollow-core kagomé PCF for generation and detection of phase-locked multi-THz pulses [Invited]," Opt. Mater. Express **9**, 3115–3122 (2019).
19. M. Bashirpour, W. Cui, A. Gamouras, and J.-M. Ménard, "Scalable fabrication of nanogratings on GaP for efficient diffraction of near-infrared pulses and enhanced terahertz generation by optical rectification," Crystals **12**, 684 (2022).
20. W. Cui, K. M. Awan, R. Huber, K. Dolgaleva, and J.-M. Ménard, "Broadband and high-sensitivity time-resolved THz system using grating-assisted tilted-pulse-front phase matching," Adv. Opt. Mater. **10**, 2101136 (2022).
21. A. Halpin, W. Cui, A. W. Schiff-Kearn, K. M. Awan, K. Dolgaleva, and J.-M. Ménard, "Enhanced terahertz detection efficiency via grating-assisted noncollinear electro-optic sampling," Phys. Rev. Appl. **12**, 031003 (2019).
22. A. Tomasino, A. Parisi, S. Stivala, P. Livreri, A. C. Cino, A. C. Busacca, M. Peccianti, and R. Morandotti, "Wideband THz time domain spectroscopy based on optical rectification and electro-optic sampling," Sci. Rep. **3**, 3116 (2013).
23. W. L. Bond, "Measurement of the refractive indices of several crystals," J. Appl. Phys. **36**, 1674–1677 (1965).
24. D. F. Parsons and P. D. Coleman, "Far infrared optical constants of gallium phosphide," Appl. Opt. **10**, 1683–1685 (1971).
25. J. Hebling, G. Almási, I. Z. Kozma, and J. Kuhl, "Velocity matching by pulse front tilting for large-area THz-pulse generation," Opt. Express **10**, 1161–1166 (2002).
26. J. Hebling, A. G. Stepanov, G. Almási, B. Bartal, and J. Kuhl, "Tunable THz pulse generation by optical rectification of ultrashort laser pulses with tilted pulse fronts," Appl. Phys. B **78**, 593–599 (2004).
27. A. G. Stepanov, J. Kuhl, I. Z. Kozma, E. Riedle, G. Almási, and J. Hebling, "Scaling up the energy of THz pulses created by optical rectification," Opt. Express **13**, 5762–5768 (2005).
28. F. Träger, *Springer Handbook of Lasers and Optics* (Springer, 2012).
29. K. Aoki, J. Savolainen, and M. Havenith, "Broadband terahertz pulse generation by optical rectification in GaP crystals," Appl. Phys. Lett. **110**, 201103 (2017).
30. C. Paradis, J. Drs, N. Modsching, O. Razskazovskaya, F. Meyer, C. Kränkel, C. J. Saraceno, V. J. Wittwer, and T. Südmeyer, "Broadband terahertz pulse generation driven by an ultrafast thin-disk laser oscillator," Opt. Express **26**, 26377–26384 (2018).
31. J. Drs, N. Modsching, C. Paradis, C. Kränkel, V. J. Wittwer, O. Razskazovskaya, and T. Südmeyer, "Optical rectification of ultrafast Yb lasers: pushing power and bandwidth of terahertz generation in GaP," J. Opt. Soc. Am. B **36**, 3039–3045 (2019).
32. R. Rautela, S. Scarfe, J.-M. Guay, P. Lazar, M. Pykal, S. Azimi, C. Grenapin, J. Boddison-Chouinard, A. Halpin, W. Wang, L. Andrzejewski, R. Plumadore, J. Park, J.-M. Ménard, M. Otyepka, and A. Luican-Mayer, "Mechanistic insight into the limiting factors of graphene-based environmental sensors," ACS Appl. Mater. Interfaces **12**, 39764–39771 (2020).
33. I. E. Gordon, L. S. Rothman, C. Hill, *et al.*, "The HITRAN2016 molecular spectroscopic database," J. Quant. Spectrosc. Radiat. Transf. **203**, 3–69 (2017).

Research Article | Vol. 9, No. 7 / 1 July 2019 / Optical Materials Express 3115
Optical Materials EXPRESS

Optical pulse structuring in gas-filled hollow-core kagomé PCF for generation and detection of phase-locked multi-THz pulses [Invited]

ALEXEI HALPIN, NICOLAS COUTURE, AND JEAN-MICHEL MÉNARD*

Department of Physics, University of Ottawa, 25 Templeton Street, Ottawa, Ontario K1N 6N5, Canada
**jean-michel.menard@uottawa.ca*

Abstract: A gas-filled hollow-core photonic crystal fiber is used to structure near-infrared ultrashort pulses and enable the generation and time-resolved detection of multi-terahertz radiation. Due to self-phase modulation, near-infrared pulses launched into the fiber experience spectral broadening characterized by the appearance of side lobes at the edges of the spectrum. Phase-locked terahertz generation between 10 and 18 terahertz is achieved by difference-frequency mixing of these spectral side lobes. This method allows for an implementation of time-resolved spectroscopy in the multi-terahertz range through the efficient production of near-infrared pulses with tailored spectra, without requiring ultrabroadband optical sources.

1. Introduction

Field-resolved spectroscopies represent an ever-growing research domain, allowing to overcome the restrictions of intensity-based measurements through phase-sensitive detection. In the terahertz (THz) spectral range, such techniques have previously been leveraged to great success for measuring the complex conductivity of photoexcited systems [1], allowing for contact-free probes of free and bound carriers in optoelectronic materials including bulk [2] or nanostructured inorganic semiconductors [3], organic systems [4,5], as well as novel materials such as monolayer transition metal dichalcogenides [6]. More recently, the increased access to few- or even sub-cycle fields in the multi-THz (> 10 THz) range has opened new avenues for ultrabroadband probes of materials across enormous spectral ranges using nonlinear crystals [7–10] or plasma-based sources [11,12]. Such sources have been applied to studies of the quantum vacuum [13,14], the spectroscopy of excitonic dynamics in perovskites [15] and two-dimensional materials [16], as well as the dynamics of phase transitions measured using ultrafast nanoscopy [17].

The sources employed in these impressive spectroscopic results exploit difference-frequency generation (DFG) from ultrashort near-infrared (NIR) pulses in nonlinear crystals. This process results in broadband THz pulses that are phase-locked with the NIR fields for performing time-domain spectroscopy. The continued development of these techniques has been facilitated in part by the increasing bandwidth of available pump sources. By definition, the frequencies produced using DFG depend directly on those contained in the associated pump fields. However, most commercially available laser sources, such as Yb:KGW sources, offer bandwidths of 5 THz or less. As such, the realization of broadband pulses at multi-THz frequencies or higher have instead been generated using bulky Ti:Sapphire amplifiers or other specialized sources [9,18]. An alternative approach, aiming to maximize the generation efficiency for specific frequency ranges in the > 10 THz range or in the mid-infrared (MIR), has relied on mixing two separate frequency-detuned pulses in nonlinear crystals [19,20]. Overall, these implementations either rely on the use of lasers with uniquely large bandwidths, or hinge on the nontrivial combination of multiple sources such as parametric amplifiers.

#360713 https://doi.org/10.1364/OME.9.003115
Journal © 2019 Received 22 Feb 2019; revised 4 Jun 2019; accepted 7 Jun 2019; published 25 Jun 2019

Optical Materials EXPRESS

Meanwhile, in the optical and NIR domains, the maturation of hollow-core fiber-based technologies has provided researchers with an inherently flexible tool for achieving spectral broadening and self-compression for various sources [21–23]. Contrary to regular solid-core fibers, these specialty fibers can be filled with a gaseous medium. This provides tunability of the linear and nonlinear optical properties of the fiber, through the selection of gas along with its pressure in the fiber. The capability of hollow-core photonic crystal fibers (HC-PCF) to transmit high peak fields is also desirable for many nonlinear optical applications.

As a result of the tight and relatively long confinement of optical pulses in gas-filled HC-PCFs, self-phase modulation (SPM) can be used to broaden the spectrum of NIR pulses possessing relatively low-energy in the μJ range [24–26]. Moreover, the HC-PCF can operate in the negative dispersion regime [25–27], an added feature to achieve a short pulse duration at the output of the fiber. Therefore, the use of a HC-PCF allows to extend the capabilities of narrowband femtosecond laser sources towards broadband and ultrashort optical applications such as phase-locked multi-THz generation and detection.

In this article we present an instrument for multi-THz spectroscopy based on SPM inside an Ar-filled HC-PCF. We use gallium selenide (GaSe) as a material for THz generation and detection due to favorable phase matching conditions for accessing the multi-THz region. The key operating principle of the instrument relies on the action of SPM in the HC-PCF, which causes spectral broadening and the appearance of side lobes at the edges of the NIR spectrum. The two lobes are separated in the frequency domain, where this spectral separation follows the strength of the SPM in the fiber. Following subsequent DFG in GaSe, we demonstrate tuning of the central THz frequency generated between 10 and 18 THz. This frequency can be tuned in a facile manner through external control of the amount of SPM in the gas-filled HC-PCF via the gas pressure or injected NIR pulse energy. Using an HC-PCF in this way provides high-throughput and flexible access to this portion of the THz spectrum for researchers relying on femtosecond laser sources with a < 5 THz bandwidth.

2. Experiment

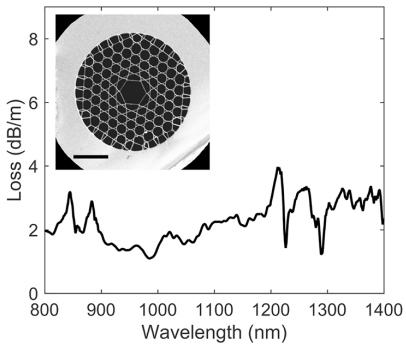

Fig. 1. Measured loss spectrum of the HC-PCF, showing low losses in the vicinity of the wavelengths of interest in these experiments. Inset: electron micrograph of the cross-section of the fiber, showing the kagomé lattice and 34 μm-diameter core (scale bar of 50 μm).

The ultrafast optical source consists of a commercially available Yb:KGW amplifier delivering 180 fs pulses centered at 1035 nm at a repetition rate of 1.1 MHz. These pulses are coupled into a 55 cm-long kagomé HC-PCF with a 34 μm-diameter core (side-to-side). The measured loss-spectrum of the fiber used in these experiments in Fig. 1 shows relatively low losses of

and flexible access to this portion of the THz spectrum for researchers relying on femtosecond laser sources with a < 5 THz bandwidth.

Optical Materials EXPRESS

2. Experiment

The ultrafast optical source consists of a commercially available Yb:KGW amplifier delivering 180 fs pulses centered at 1035 nm at a repetition rate of 1.1 MHz. These pulses are coupled into a 55 cm-long kagomé HC-PCF with a 34 µm-diameter core (side-to-side). The measured loss spectrum of the fiber used in these experiments in Fig. 1 shows relatively low losses of < 2 dB/m over the spectral range of 900–1100 nm used in our experiment. The two-dimensional structure of the photonic crystal defining the fiber can be seen in the electron micrograph in the inset of Fig. 1. The fiber is entirely placed inside a gas cell which is then filled with Ar gas. In the fiber the pulses undergo SPM, a $\chi^{(3)}$ effect, which leads to the generation of new frequencies through the intensity dependent refractive index of Ar. By changing the gas pressure inside the HC-PCF or the input pulse energy, we can control the amount of SPM. Here, we apply a constant Ar pressure of 13 bar to provide sufficient SPM at different pulse energies. Under these experimental conditions, the calculated zero-dispersion wavelength (ZDW) occurs at 650 nm and the group velocity dispersion (GVD) is ~6 fs^2/mm. After passing through the HC-PCF, the pulse is sent to a chirped mirror pair (CMP) that compensates for GVD, leading to nearly transform-limited NIR pulses entering the THz section of the setup. In this work, the CMP corrects for approximately −2200 fs^2.

A conventional THz time-domain spectroscopy (THz-TDS) scheme is used to generate and detect THz radiation with the structured NIR pulses [28]. The full experimental setup is shown in Fig. 2. Following spectral shaping in the HC-PCF, the beam is split into two paths. In the first path, THz radiation is generated via DFG in a 50 (± 10) µm thick GaSe crystal, and it is subsequently focused into a similar GaSe crystal for detection. Meanwhile, the beam in the second path acts as a gate pulse for time-resolved detection of the multi-THz pulse. The gate pulse, which can be temporally delayed using a translation stage, is spatially and temporally overlapped with the THz pulse in the detection crystal. Time-resolved electro-optic sampling (EOS) is performed to directly measure the oscillating electric field of the THz radiation.

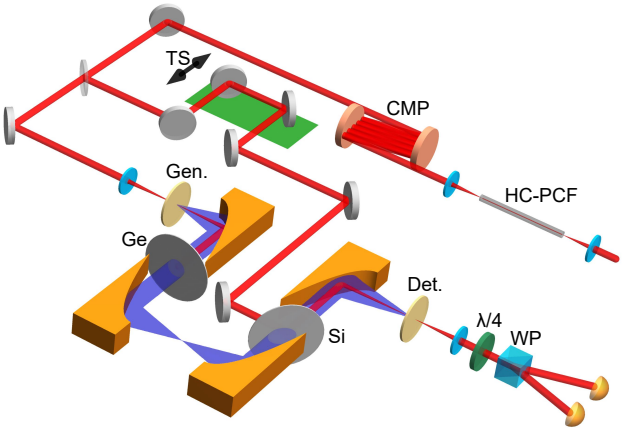

Fig. 2. Schematic of the experimental setup. Ultrashort NIR pulses are coupled into a HC-PCF filled with 13 bar of Ar gas. THz radiation is subsequently generated and detected using a standard THz-TDS system. CMP: chirped mirror pair; TS: translation stage; Gen.: generation crystal; Ge: germanium wafer; Si: silicon wafer; Det: detection crystal; $\lambda/4$: quarter-wave plate; WP: Wollaston prism.

3. Results and discussion

Figure 3 shows the measured NIR spectral amplitudes and autocorrelation traces of the pulse at the output of the HC-PCF for different input pulse energies. The amplitudes are obtained from the intensity spectra measured with a USB spectrometer while the temporal profiles are measured with a home-made intensity autocorrelator utilizing second harmonic generation (SHG) from a

temporally overlapped with the THz pulse in the detection crystal. Time-resolved electro-optic sampling (EOS) is performed to directly measure the oscillating electric field of the THz radiation.

3. Results and Discussion

Optical Materials EXPRESS

Figure 3 shows the measured NIR spectral amplitudes and autocorrelation traces of the pulse at the output of the HC-PCF for different input pulse energies. The amplitudes are obtained from the intensity spectra measured with a USB spectrometer while the temporal profiles are measured with a home-made intensity autocorrelator utilizing second harmonic generation (SHG) from a 150-μm-thick beta-barium borate (BBO) crystal. We display the spectra in Fig. 3a in amplitude, rather than in intensity, as the THz generation efficiency from the DFG process depends on the spectral field amplitudes. Directly at the output of the optical source, the reference NIR amplitude spectrum has a bandwidth of approximately 4 THz full-width-half-maximum (FWHM). The spectrum is strongly modified by nonlinear propagation inside the HC-PCF. We observe a gradual spectral broadening as well as the appearance of new spectral components as the pulse energy is increased. For pulse energies above 0.9 μJ, the NIR spectral energy is mostly distributed within two side lobes at the edges of the spectrum, while the amplitude significantly decreases around the central frequency. From the spectroscopic measurements shown in Fig. 3a, we determine that the side lobe separation increases from 4.5 THz to 24 THz for the lowest to highest pulse energies considered here.

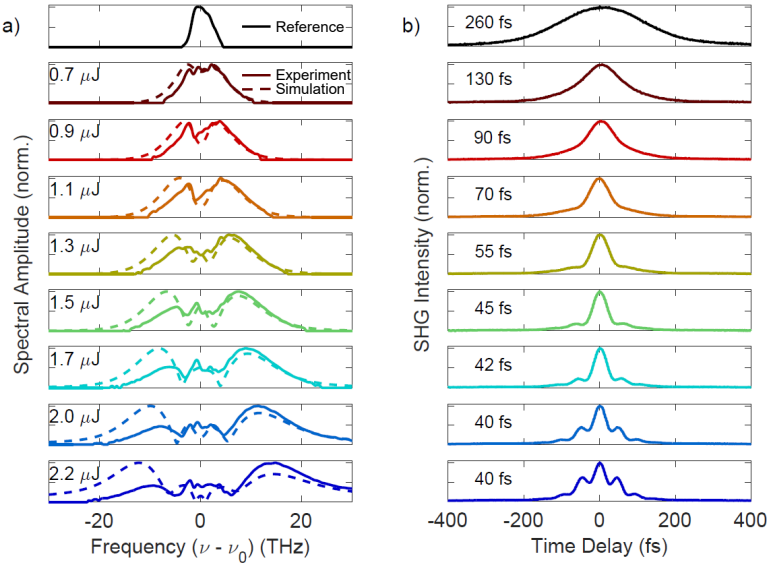

Fig. 3. (a) Measured NIR spectra (plotted in amplitude) following broadening in the HC-PCF through SPM for increasing pulse energies injected into the fiber and (b) their corresponding measured intensity autocorrelation traces. The full-width-half-maximum (FWHM) of the autocorrelation traces are displayed. The spectral and temporal profiles of the reference pulse, before entering the HC-PCF, are shown in the top panels in black. Solid lines represent experimental data while dashed lines are simulations. The spectra are re-centered about the central frequency of the laser.

In order to model the spectral response of the HC-PCF we performed simulations solving the nonlinear wave equation for a Gaussian input spectrum [29], where the fiber dispersion is approximated by that of a narrow-bore capillary [30] and SPM is applied via the addition of a nonlinear spectral phase. For the pulse duration and input coupling used in our experimental conditions we find reasonable agreement between the simulations and the experimental results. Some discrepancies nevertheless remain due to the non-Gaussian spectral shape of our input pulse, and due to residual third-order chirp which is not compensated by the grating compressor in the amplified laser system.

The autocorrelation (AC) traces shown in Fig. 3(b) demonstrate the consequences of the SPM and CMP on the temporal profile of the NIR pulses. While broadband spectra are required for

Optical Materials EXPRESS

In order to model the spectral response of the HC-PCF we performed simulations solving the nonlinear wave equation for a Gaussian input spectrum [29], where the fiber dispersion is approximated by that of a narrow bore capillary [30] and SPM is applied via the addition of a nonlinear spectral phase. For the pulse duration and input coupling used in our experimental conditions we find reasonable agreement between the simulations and the experimental results. Some discrepancies nevertheless remain due to the non-Gaussian spectral shape of our input pulses and due to residual third-order chirp which is not compensated by the grating compressor in the amplified laser system.

The autocorrelation (AC) traces shown in Fig. 3b demonstrate the consequences of the SPM and CMP on the temporal profile of the NIR pulses. While broadband spectra are required for efficient DFG at multi-THz frequencies, short NIR pulses are also crucial to achieve (i) broadband THz generation, since relevant frequencies involved in the DFG process overlap in time and (ii) for time-domain detection, since the gating pulse must be shorter than the period of the oscillating THz field. The "reference" NIR pulse in Fig. 3b yields an AC trace with a 260 fs FWHM, which corresponds to a 180 fs pulse duration assuming a Gaussian temporal shape. For an input pulse energy of 0.7 μJ, propagation through the HC-PCF and post-compression stage in the CMP reduces the pulse duration by half. We then further shorten the NIR pulses by another factor of three by increasing the input pulse energy up to 1.7 μJ. At that pulse energy we approach the resolution limit of our autocorrelator. The shortest pulse measured yields an AC trace of 40 fs corresponding to a pulse duration of ~30 fs. The non-Gaussian shape of the AC trace at the highest pulse energies is due to an imperfect spectral phase compensation by the CMP. Nonetheless, the NIR pulses are measured to be sufficiently short to achieve THz generation and detection over the frequency range considered in our experiments (< 20 THz).

Figures 4(a) and 4(b) show measured time-resolved THz transients and their associated amplitude spectral, respectively. For clarity we have normalized each trace and its spectrum to their maximal value. In the top panel, we show a THz measurement obtained with the NIR reference pulse. We observe oscillatory THz field transients at low frequencies, whereas the amplitude spectrum presents a narrow peak in the vicinity of 4 THz, consistent with the bandwidth of our laser source. In contrast, when a HC-PCF is used, we observe a rapidly oscillating field in the time domain, corresponding to frequencies generated beyond 4 THz, with a gap in the vicinity of 3 - 4 THz within the reststrahlen band of GaSe [31].

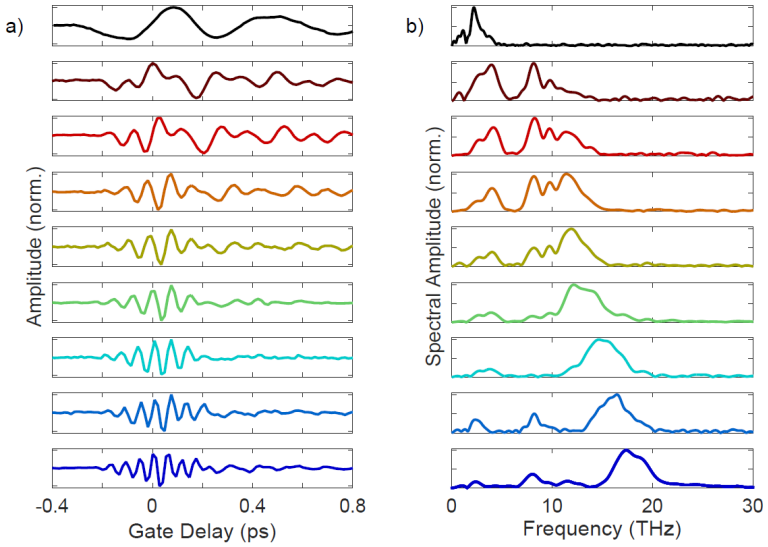

Fig. 4. (a) THz transients and (b) spectra corresponding to the pulse energies given in Fig. 3. In the top panels we show the measured THz transient and spectrum corresponding to the reference NIR pulse before entering the HC-PCF. For low pulse energies injected into the HC-PCF the time-domain traces contain mostly low-frequency oscillations. For higher pulse energies the full transients shorten considerably and the high-frequency components of the transient become more evident in the spectral domain.

Optical Materials EXPRESS

For increasing NIR pulse energy the transients shorten, and begin to resemble a few-cycle pulse with high-frequency oscillations. Correspondingly, we observe the emergence of more high-frequency content in the THz amplitude spectra plotted in Fig. 4(b). By varying the input pulse energy launched into the HC-PCF, we can smoothly tune the maximum generated THz frequency from 10 to 18 THz. This frequency tuning is the direct result of the NIR spectral and temporal reshaping, which provides access to high THz frequencies by enabling nonlinear interaction between a larger range of NIR spectral components. Furthermore, the redistribution of the NIR spectral weight into two separated side lobes allows us to target a particular THz frequency. The dominant side lobes of the structured NIR pulse possess unequal amplitudes, however, the optical energy contained within the two dominant side lobes can be maximized by adjusting the high-order dispersion of the input pulse before entering the HC-PCF, according to numerical simulations. This scheme would then result in a more efficient THz generation in the high-frequency regime, and may even be able to compete with more complex configurations relying on a dual beam geometry [19,20].

We do not explore the regime above 20 THz, however, due to technical limitations in controlling the spectral phase of the SPM-broadened pulses following the HC-PCF: the CMP employed in this work only compensates for dispersion over a range of approximately 20 THz, which is narrower than the largest NIR bandwidth shown in the bottom panel of Fig. 3(a). For increasing bandwidths, achieving transform-limited pulses to allow for effective generation and detection of THz pulses requires a more precise approach to dispersion compensation [32]. With suitably compressed broadband pulses, there is no fundamental limitation restricting our approach from reaching higher frequencies into the MIR.

4. Conclusion

The use of NIR pulses undergoing SPM in a gas-filled HC-PCF is shown to provide a platform for the generation of tunable multi-THz pulses in the range of 10-18 THz using a compact Yb:KGW system. In our experiment, the structured NIR pulses have spectra characterized by two side lobes, which can be separated in frequency by an arbitrary amount determined by the input pulse energy. Alternatively, one could also keep the input pulse energy constant and instead vary the gas pressure inside the HC-PCF to modulate the spectral broadening [28]. Compensating for linear chirp using a CMP decreases the time duration of the SPM-broadened pulses following propagation in the HC-PCF, as verified through autocorrelation measurements. The central THz frequency generated using the associated ultrashort NIR pulses can thus be controlled between 10-20 THz by exploiting SPM, through DFG between the associated side lobes in the NIR spectrum.

Reaching higher THz frequencies above 20 THz also demands a more broadband compensation of dispersion after the HC-PCF. Nevertheless, we believe that our general fiber-based scheme does not impose any fundamental limitations for achieving higher generation frequencies into the MIR, and can potentially be used with various ultrafast optical sources. We expect this configuration, leveraging the robust technology of nonlinear photonics in fibers and the use of compact Yb:KGW laser systems, to be widely applicable and easily multiplexed for enabling THz spectroscopy covering the full multi-THz range.

Finally, by combining PCF and THz technologies, this work is even more relevant in the recent context of emerging HC-PCFs able to transmit MIR and THz radiation [33–37]. In the future, it could also be integrated with a design enabling second-order nonlinear effects in HC-PCF, allowing an all-fiber configuration for tunable phase-locked THz generation by DFG [38,39].

Funding

Natural Sciences and Engineering Research Council of Canada (NSERC); Canada Foundation for Innovation (CFI); Ontario Ministry of Research, Innovation and Science (MRIS).

Optical Materials EXPRESS

Acknowledgments

We thank the Russell division (Max Planck Institute for the Science of Light) for providing the kagomé PCF and Prof. David Cooke (McGill University) for providing GaSe crystals.

References

1. R. Ulbricht, E. Hendry, J. Shan, T. F. Heinz, and M. Bonn, "Carrier dynamics in semiconductors studied with time-resolved terahertz spectroscopy," Rev. Mod. Phys. **83**(2), 543–586 (2011).
2. M. C. Beard, G. M. Turner, and C. A. Schmuttenmaer, "Terahertz spectroscopy," J. Phys. Chem. B **106**(29), 7146–7159 (2002).
3. P. Parkinson, C. Dodson, H. J. Joyce, K. A. Bertness, N. A. Sanford, L. M. Herz, and M. B. Johnston, "Noncontact Measurement of Charge Carrier Lifetime and Mobility in GaN Nanowires," Nano Lett. **12**(9), 4600–4604 (2012).
4. F. A. Hegmann, R. R. Tykwinski, K. P. H. Lui, J. E. Bullock, and J. E. Anthony, "Picosecond Transient Photoconductivity in Functionalized Pentacene Molecular Crystals Probed by Terahertz Pulse Spectroscopy," Phys. Rev. Lett. **89**(22), 227403 (2002).
5. E. Hendry, M. Koeberg, J. Schins, H. Nienhuys, V. Sundström, L. Siebbeles, and M. Bonn, "Interchain effects in the ultrafast photophysics of a semiconducting polymer: THz time-domain spectroscopy of thin films and isolated chains in solution," Phys. Rev. B **71**(12), 125201 (2005).
6. C. J. Docherty, P. Parkinson, H. J. Joyce, M.-H. Chiu, C.-H. Chen, M.-Y. Lee, L.-J. Li, L. M. Herz, and M. B. Johnston, "Ultrafast Transient Terahertz Conductivity of Monolayer MoS_2 and WSe_2 Grown by Chemical Vapor Deposition," ACS Nano **8**(11), 11147–11153 (2014).
7. R. A. Kaindl, F. Eickemeyer, M. Woerner, and T. Elsaesser, "Broadband phase-matched difference frequency mixing of femtosecond pulses in GaSe: Experiment and theory," Appl. Phys. Lett. **75**(8), 1060–1062 (1999).
8. R. Huber, A. Brodschelm, F. Tauser, and A. Leitenstorfer, "Generation and field-resolved detection of femtosecond electromagnetic pulses tunable up to 41 THz," Appl. Phys. Lett. **76**(22), 3191–3193 (2000).
9. C. Kübler, R. Huber, S. Tübel, and A. Leitenstorfer, "Ultrabroadband detection of multi-terahertz field transients with GaSe electro-optic sensors: Approaching the near infrared," Appl. Phys. Lett. **85**(16), 3360–3362 (2004).
10. A. Sell, A. Leitenstorfer, and R. Huber, "Phase-locked generation and field-resolved detection of widely tunable terahertz pulses with amplitudes exceeding 100 MV/cm," Opt. Lett. **33**(23), 2767–2769 (2008).
11. E. Matsubara, M. Nagai, and M. Ashida, "Ultrabroadband coherent electric field from far infrared to 200 THz using air plasma induced by 10 fs pulses," Appl. Phys. Lett. **101**(1), 011105 (2012).
12. V. A. Andreeva, O. G. Kosareva, N. A. Panov, D. E. Shipilo, P. M. Solyankin, M. N. Esaulkov, P. González de Alaiza Martínez, A. P. Shkurinov, V. A. Makarov, L. Bergé, and S. L. Chin, "Ultrabroad Terahertz Spectrum Generation from an Air-Based Filament Plasma," Phys. Rev. Lett. **116**(6), 063902 (2016).
13. C. Riek, D. V. Seletskiy, A. S. Moskalenko, J. F. Schmidt, P. Krauspe, S. Eckart, S. Eggert, G. Burkard, and A. Leitenstorfer, "Direct sampling of electric-field vacuum fluctuations," Science **350**(6259), 420–423 (2015).
14. C. Riek, P. Sulzer, M. Seeger, A. S. Moskalenko, G. Burkard, D. V. Seletskiy, and A. Leitenstorfer, "Subcycle quantum electrodynamics," Nature **541**(7637), 376–379 (2017).
15. D. A. Valverde-Chavez, C. S. Ponseca, C. C. Stoumpos, A. Yartsev, M. G. Kanatzidis, V. Sundström, and D. G. Cooke, "Intrinsic femtosecond charge generation dynamics in single crystal $CH_3NH_3PbI_3$," Energy Environ. Sci. **8**(12), 3700–3707 (2015).
16. P. Steinleitner, P. Merkl, P. Nagler, J. Mornhinweg, C. Schüller, T. Korn, A. Chernikov, and R. Huber, "Direct Observation of Ultrafast Exciton Formation in a Monolayer of WSe_2," Nano Lett. **17**(3), 1455–1460 (2017).
17. M. A. Huber, M. Plankl, M. Eisele, R. E. Marvel, F. Sandner, T. Korn, C. Schüller, R. F. Haglund, R. Huber, and T. L. Cocker, "Ultrafast Mid-Infrared Nanoscopy of Strained Vanadium Dioxide Nanobeams," Nano Lett. **16**(2), 1421–1427 (2016).
18. I. Pupeza, D. Sánchez, J. Zhang, N. Lilienfein, M. Seidel, N. Karpowicz, T. Paasch-Colberg, I. Znakovskaya, M. Pescher, W. Schweinberger, V. Pervak, E. Fill, O. Pronin, Z. Wei, F. Krausz, A. Apolonski, and J. Biegert, "High-power sub-two-cycle mid-infrared pulses at 100 MHz repetition rate," Nat. Photonics **9**(11), 721–724 (2015).
19. M. Knorr, J. Raab, M. Tauer, P. Merkl, D. Peller, E. Wittmann, E. Riedle, C. Lange, and R. Huber, "Phase-locked multi-terahertz electric fields exceeding 13 MV/cm at a 190 kHz repetition rate," Opt. Lett. **42**(21), 4367 (2017).
20. M. Seidel, X. Xiao, S. A. Hussain, G. Arisholm, A. Hartung, K. T. Zawilski, P. G. Schunemann, F. Habel, M. Trubetskov, V. Pervak, O. Pronin, and F. Krausz, "Multi-watt, multi-octave, mid-infrared femtosecond source," Sci. Adv. **4**(4), eaaq1526 (2018).
21. P. St. J. Russell, P. Hölzer, W. Chang, A. Abdolvand, and J. C. Travers, "Hollow-core photonic crystal fibres for gas-based nonlinear optics," Nat. Photonics **8**(4), 278–286 (2014).
22. T. Balčiūnas, C. Fourcade-Dutin, G. Fan, T. Witting, A. A. Voronin, A. M. Zheltikov, F. Gerome, G. G. Paulus, A. Baltuška, and F. Benabid, "A strong-field driver in the single-cycle regime based on self-compression in a kagome fibre," Nat. Commun. **6**(1), 6117 (2015).
23. G. Fan, T. Balčiūnas, T. Kanai, T. Flöry, G. Andriukaitis, B. E. Schmidt, F. Légaré, and A. Baltuška, "Hollow-core-waveguide compression of multi-millijoule CEP-stable 32 μm pulses," Optica **3**(12), 1308 (2016).

Optical Materials EXPRESS

24. C. Schriber, C. J. Saraceno, C. F. Dutin, F. Benabid, F. Emaury, F. Gerome, M. Trant, O. H. Heckl, T. Südmeyer, U. Keller, and Y. Y. Wang, "Beam delivery and pulse compression to sub-50 fs of a modelocked thin-disk laser in a gas-filled Kagome-type HC-PCF fiber," Opt. Express **21**(4), 4986–4994 (2013).
25. J. C. Travers, W. Chang, J. Nold, N. Y. Joly, and P. St. J. Russell, "Ultrafast nonlinear optics in gas-filled hollow-core photonic crystal fibers [Invited]," J. Opt. Soc. Am. B **28**(12), A11–A26 (2011).
26. M. Gebhardt, C. Gaida, S. Hädrich, F. Stutzki, C. Jauregui, J. Limpert, and A. Tünnermann, "Nonlinear compression of an ultrashort-pulse thulium-based fiber laser to sub-70 fs in Kagome photonic crystal fiber," Opt. Lett. **40**(12), 2770 (2015).
27. K. F. Mak, M. Seidel, O. Pronin, M. H. Frosz, A. Abdolvand, V. Pervak, A. Apolonski, F. Krausz, J. C. Travers, and P. St. J. Russell, "Compressing µJ-level pulses from 250 fs to sub-10 fs at 38-MHz repetition rate using two gas-filled hollow-core photonic crystal fiber stages," Opt. Lett. **40**(7), 1238–1241 (2015).
28. W. Cui, A. W. Schiff-Kearn, E. Zhang, N. Couture, F. Tani, D. Novoa, P. St. J. Russell, and J.-M. Ménard, "Broadband and tunable time-resolved THz system using argon-filled hollow-core photonic crystal fiber," APL Photonics **3**(11), 111301 (2018).
29. G. Agrawal, *Nonlinear Fiber Optics* (Elsevier, 2013).
30. E. Marcatili and R. Schmeltzer, "Hollow metallic and dielectric waveguides for long distance optical transmission and lasers," Bell Syst. Tech. J. **43**(4), 1783–1809 (1964).
31. C.-S. Chang, C.-W. Chen, C.-L. Pan, J. Y. Huang, P.-K. Chung, S.-T. Yen, S.-H. Lin, and T.-T. Tang, "Optical properties and potential applications of e-GaSe at terahertz frequencies," J. Opt. Soc. Am. B **26**(9), A58–A65 (2009).
32. R. L. Fork, C. H. Cruz, P. C. Becker, and C. V. Shank, "Compression of optical pulses to six femtoseconds by using cubic phase compensation," Opt. Lett. **12**(7), 483–485 (1987).
33. K. Nielsen, H. K. Rasmussen, A. J. L. Adam, P. C. Planken, O. Bang, and P. U. Jepsen, "Bendable, low-loss Topas fibers for the terahertz frequency range," Opt. Express **17**(10), 8592–8601 (2009).
34. J. Anthony, A. Argyros, R. Leonhardt, and S. G. Leon-Saval, "THz propagation in kagome hollow-core microstructured fibers," Opt. Express **19**(19), 18470–18478 (2011).
35. A. N. Kolyadin, A. F. Kosolapov, A. D. Pryamikov, A. S. Biriukov, V. G. Plotnichenko, and E. M. Dianov, "Light transmission in negative curvature hollow core fiber in extremely high material loss region," Opt. Express **21**(8), 9514 (2013).
36. J. Yang, J. Zhao, C. Gong, H. Tian, L. Sun, P. Chen, L. Lin, and W. Liu, "3D printed low-loss THz waveguide based on Kagome photonic crystal structure," Opt. Express **24**(20), 22454 (2016).
37. H. Li, G. Ren, B. Zhu, Y. Gao, B. Yin, J. Wang, and S. Jian, "Guiding terahertz orbital angular momentum beams in multimode Kagome hollow-core fibers," Opt. Lett. **42**(2), 179 (2017).
38. J.-M. Ménard and P. St. J. Russell, "Phase-matched electric-field-induced second-harmonic generation in Xe-filled hollow-core photonic crystal fiber," Opt. Lett. **40**(15), 3679–3682 (2015).
39. J.-M. Ménard, F. Köttig, and P. St. J. Russell, "Broadband electric-field-induced LP_{01} and LP_{02} second harmonic generation in Xe-filled hollow-core PCF," Opt. Lett. **41**(16), 3795–3798 (2016).

Chapter 6

Supercontinuum generation in fiber

Optical fiber has long been a flexible vehicle in which to explore nonlinear optical effects, both to improve our understanding of fundamental physics and to develop compact, practical systems for a variety of applications. Though nonlinear effects in fiber are now well-documented, reaching a high degree of nonlinearity at a lower power threshold remains an objective to facilitate integration of on-chip and fiber-based systems without the need for an intense pump [115, 116].

To enhance fiber nonlinearity, thus increasing the nonlinear parameter γ described in section 2.1.2, there are two main strategies that can be implemented: i) engineering the fiber geometry to confine light more tightly within the core, effectively reducing the effective mode area A_{eff}; or ii) integrating a material with nonlinear properties greater than those of silica. The former technique leads to the staggering variety of photonic crystal and microstructured fibers available today. Surrounding the core with air capillaries helps to shrink A_{eff}. Moreover, the photonic crystal structure can be tuned to reach a desired wavelength dependence in the dispersion and birefringence characteristics of the fiber. The latter approach has led to the use of soft glasses including chalcogenides and tellurides [117], as well as some novel gas- and liquid-filled core fibers [118, 95]. Soft glasses can have a nonlinear index of refraction (n_2) up to 100$\times$ that of silica but suffer from being more difficult to handle and challenging to fabricate since state-of-the-art methods from silica are not easily transferrable. Gas-filled hollow fiber cores can enable high input power and dispersion or nonlinearity tunability with pressure [119]. Both strategies can be incor-

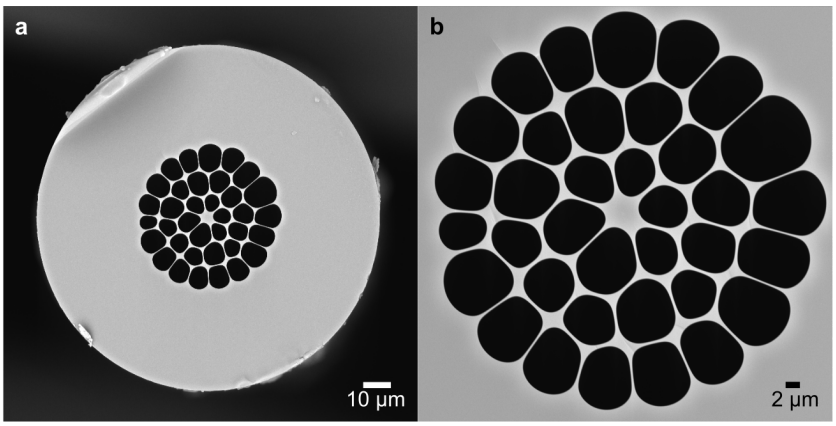

Figure 6.1: Scanning electron microscope (SEM) image of a) the tip of the PCF and b) the photonic crystal structure. The capillaries surrounding the core confine the mode more tightly to enhance nonlinear effects. Dark areas represent air and white areas represent dielectric material.

porated in the fabrication of germania-doped fibers. Germania has a more favorable loss spectrum toward the mid-infrared, a nonlinear refractive index approximately 3× greater than silica, and it has comparable thermo-mechanical properties to silica so that it can be drawn in the same way as conventional silica fiber.

6.1 Germania-doped PCF fabrication

The PCF fabrication process begins with the GeO_2-doping of a silica rod by the modified chemical vapor deposition (MCVD) process [120]. This process utilizes a flow of $SiCl_4$, $GeCl_4$ and O_2 into a silica tube to form SiO_2 and GeO_2 particles, which cling to the inside of the tube. The silica tube is then etched away and the GeO_2 layer is deposited at 1600 ^{o}C, then deposited at 2000 ^{o}C with a flow of pure $GeCl_4$ to prevent rod deformations. The doped rod used in the PCF preform has a diameter of 1.75 mm and a relatively homogeneous doping of 50 mol% GeO_2, measured with an electron probe micro-analyzer. This doping level provides a refractive index difference ∼0.045 with respect to pure silica

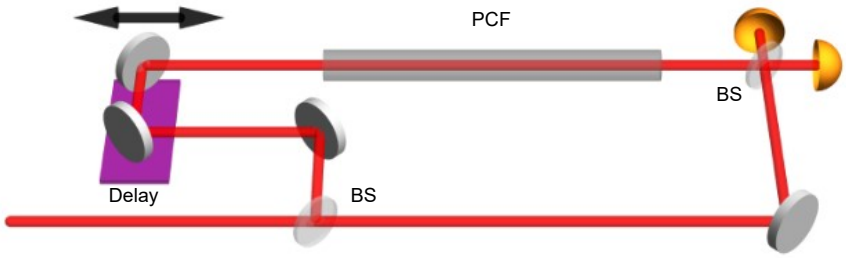

Figure 6.2: Schematic of Mach-Zehnder interferometer used to extract dispersion profile of the 70 cm-long PCF. A beamsplitter (BS) separates the beam in two paths. One to be injected into the PCF and the other travelling through air. The two beams are overlapped in another BS to then resolve the interference with two photodiodes (yellow half-spheres).

at a wavelength of 633 nm, thus better confining the light in the core to enhance nonlinear effects for SC generation.

Three layers of thin-walled capillaries are stacked around the doped rod and placed snugly inside a thick silica jacket and drawn using a conventional fiber drawing tower. The result of this first draw is then placed in a 6 mm-thick silica jacket to create the final preform, which is drawn again to achieve the PCF whose cross-section is shown in Fig. 6.1.

The dispersive properties of the germania-doped PCF are investigated with a Mach-Zehnder interferometer (MZI) using the PCF in one of its arms, as shown in Fig. 6.2. Three laser diodes operating in the spectral windows 875 to 925 nm, 950 to 1060 nm, and 1125 to 1175 nm form a quasi-continuous data set allowing us to plot the wavelength dependence of the path difference $\Delta L(\lambda)$ and fit the data to a 4^{th} order polynomial function. This data allows us to extract the dispersion D between 875 and 1175 nm through the relation

$$D(\lambda) = \frac{1}{Lc}\frac{d}{d\lambda}\Delta L(\lambda) \tag{6.1}$$

where L is the length of the PCF (70 cm) and c is the speed of light in vacuum [121]. The experimental results from this process are found in the supplementary information of the publication associated to this chapter. The calculated dispersion curve reveals a zero-dispersion wavelength (ZDW) of 1047 nm. Injecting light into the fiber near the ZDW allows phase-matched parametric processes like four-wave mixing, SPM, and self-shifted Raman solitons to generate a broad spectrum [122, 123, 124].

6.2 Influence of core geometry

Upon closer examination of the SEM image shown in Fig. 6.1b, one may not only notice asymmetry in the photonic crystal structure surrounding the core of the fiber, but also an ellipticity of the core itself. Fitting an ellipse to the central core of the PCF, we find an ellipticity of 0.17. In light of this result, we hypothesized that this fiber may have some interesting polarization properties due to the assumed birefringence induced by the elliptical core [125, 4]. To quantify the birefringence of the fiber, we performed the cut-back method to extract the beat length at the central wavelength of the laser.

First, to minimize spectral broadening in the highly nonlinear fiber, the peak power of the light injected into the PCF is minimized by keeping the average power low and by chirping the pulse to a duration of 10 ps, thus decreasing the peak intensity by a factor of more than 55 in comparison to the pulse duration of the transform limited duration of 180 fs. Next, pulses with linear polarization oriented 45 degrees from a principal fiber axis, as depicted in Fig. 2.4, are launched into the fiber. A linear polarizer and a power meter are placed at the output facet of the fiber and the orientation of the principal axes at the fiber output are unknown. The transmitted power through the fiber is measured as a function of the output polarizer angle, where the difference between the maximum and minimum transmitted powers (ΔP, normalized to input power) is extracted and the relative polarizer angle between P_{max} and P_{min} is 90 degrees. When ΔP approaches zero, it implies that orthogonal polarization components have the same magnitude, which corresponds to the case of linearly polarized light and circularly polarized light, or phase shifts of $M\pi/2$ where M is an integer. Repeating this process for several fiber lengths allow us to extract L_B. Experimental results from this process while injecting linearly polarized light 45 and 135 degrees from this process are shown in Fig. 6.3a and b, respectively. The experimental results are fitted with a sinusoidal function with linear damping to account for increased losses with longer fiber lengths. The minima in the fit function correspond to phase shifts of $M\pi/2$. Accounting for errors in measured fiber lengths, we find that L_B in on the order of 1 m and the birefringence is therefore on the order of 10^{-6} at a wavelength of 1030 nm. Birefringence with this order of magnitude is typical for elliptical core fibers and is con-

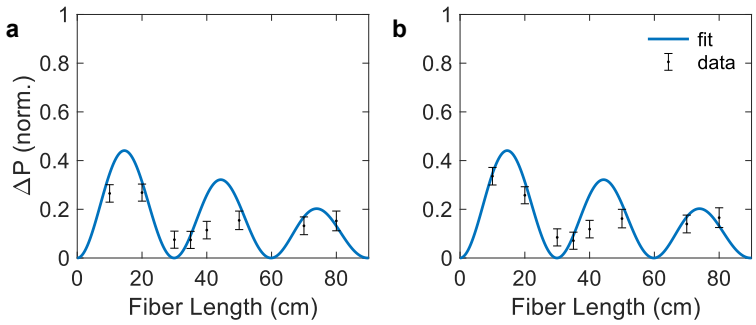

Figure 6.3: Experimental results from the cut-back method injecting linear polarized a) 45 degrees and b) 135 degrees from a principal axis of the fiber. Fiber lengths between 10 and 80 cm were explored, keeping input coupling fixed for each fiber length.

sidered to be in the "low birefringence" regime [4]. Fibers utilizing stress instead of core shape to induce birefringence, such as panda and bow-tie fibers, can reach birefringence on the order of 10^{-4}.

To explore the polarization properties of a supercontinuum generated is such a unique fiber, we built a spectrometer that is capable of resolving spectra associated with its principal axes spanning over several optical octaves. This involved an ultrabroadband linear polarizer, which in turn allowed us to extract the degree of polarization (DOP) of the spectrum, and a Czerny-Turner monochromator [126]. We started by injecting a relatively low pulse energy into the fiber, generating a modest supercontinuum spanning ∼400 nm, and recorded the spectrum as we rotated the linear polarization of the input pulse. This step allowed us to find the polarization orientation which corresponded to the principal axes of the fiber that were favorable for SC generation. Next, keeping the input polarization fixed to a principal axis, we increased the pulse energy and recorded the output spectrum associated to the principal axis of injection and the orthogonal axis. Raman solitons, dispersive waves, and four-wave mixing broadened the spectrum such that it spans from 450 nm to 2150 nm. Increasing the pulse energy launched into the fiber, thus increasing the peak power launched into the fiber, allowed us to observe the generation of higher order solitons populating the SC. We found that Raman solitons preserved their polarization during propagation in the fiber and associated a depolarization mechanism associated to a Rayleigh-like scattering, preferentially scattering high frequency components of the SC

to the orthogonal fiber axis. In fact, as more light scattered into the orthogonal principal axis of the fiber, we observed solitons being generated in this orthogonal as enough light scattered into it to reach the fundamental soliton threshold, which also preserved its polarization. Though we could not generate mid-IR light as originally planned, these results revealed fascinating information on soliton behavior.

This work was published in *Journal of Physics: Photonics* in 2021 and titled "Polarization-resolved supercontinuum generated in a germania-doped photonic crystal fiber" [36]. The paper and supplementary information are found in this chapter in their published forms. This work was also presented at several conferences [127, 128, 129]. The paper includes the main results of the work described above. The supplementary information includes the experimentally retrieved dispersion of the fiber from the MZI measurement, details on the modified nonlinear Schrödinger equation used to simulate propagation in the fiber, and the results of the numerical simulations that include depolarization due to the birefringence of the fiber.

IOP Publishing J. Phys. Photonics 3 (2021) 025002 https://doi.org/10.1088/2515-7647/abe7d9

Journal of Physics: Photonics

PAPER

Polarization-resolved supercontinuum generated in a germania-doped photonic crystal fiber

Nicolas Couture[1], Rachel Ostic[1], P Harshavardhan Reddy[2,3], Ajoy Kumar Kar[4], Mukul Chandra Paul[3] and Jean-Michel Ménard[1]

[1] Department of Physics, University of Ottawa, Ottawa, ON K1N 6N5, Canada
[2] Academy of Scientific and Innovative Research, CSIR-CGCRI Campus, Kolkata 700032, India
[3] Fiber Optics and Photonics Division, CSIR-CGCRI Campus, Kolkata 700032, India
[4] Institute of Photonics and Quantum Sciences, Heriot-Watt University, Riccarton Campus, EH14 4AS Edinburgh, United Kingdom

E-mail: jean-michel.menard@uottawa.ca

OPEN ACCESS

RECEIVED
28 August 2020

REVISED
2 February 2021

ACCEPTED FOR PUBLICATION
18 February 2021

PUBLISHED
9 March 2021

Keywords: supercontinuum generation, photonic crystal fibers, spectrometers, depolarization, nonlinear optics, fiber optics

Supplementary material for this article is available online

Abstract

We characterize the polarization properties of a supercontinuum (SC) generated in a GeO_2-doped photonic crystal fiber (PCF) to reveal the interplay between nonlinear broadening mechanisms of a pulse propagating in two independent fundamental modes associated to the principal axes of the fiber. Notably, we resolve self-phase modulation, self-shifted Raman solitons and dispersive waves within a set of orthogonal polarization states as they contribute to generate a broad spectrum spanning from 450 to 2150 nm. Interestingly, our experimental results feature a high degree of polarization at the edges of the spectrum in comparison to the region near the pump wavelength. We show that this modulation is caused by nonlinear spectral broadening. We also identify an additional depolarization mechanism preferentially acting on shorter wavelengths, indicative of a Rayleigh-like scattering effect due to the presence of intrinsic sub-wavelength defects in the fiber. Experiments rely on a free-space grating-based monochromator and a broadband polarizer to monitor the output SC and its linear polarization components along the principal axes of the PCF. Our results and experimental technique pave the way toward an improved standard for the characterization of broadband optical spectra and more efficient implementation of highly nonlinear fibers in a large range of polarization-sensitive applications.

1. Introduction

The ability to rely on nonlinear optical phenomena to convert a narrow laser spectral linewidth into a broad frequency spectrum, also called supercontinuum (SC), has enabled many applications in optical coherence tomography (OCT), photonic device testing, and optical communications [1–3]. The high spatial coherence of broadband, fiber-based sources is also ideal for applications in optical microscopy [4, 5]. Although silica-based solid-core optical fibers are most commonly used to produce intense and broad SC, there has been a recent interest to develop broadband sources in different optical media to avoid some limitations imposed by silica. Specialty fibers like hollow-core photonic crystal fibers (PCFs) [6–9] and fibers made of soft glasses, like fluoride [10–13] or chalcogenide [14–17], have notably been used to generate SC extending to the ultraviolet (UV) or mid-infrared (MIR) regions, where silica is strongly absorptive [13]. Moreover, pure germania (GeO_2) fibers and GeO_2-doped silica fibers have attracted interest both because of their transparency in the MIR region and the fact that their fabrication relies on well-established drawing methods for silica fibers [18, 19]. For instance, an SC spectrum extending beyond 3 μm was achieved in a highly germania-doped fiber with a record optical power of 1.44 W [19].

In general, small imperfections and inhomogeneities in all types of fibers are inevitable due to intrinsic glass impurities and the high sensitivity of the drawing process to environmental changes and vibrations. These defects can lead to polarization changes during optical propagation [20], which are detrimental to

many applications such as OCT [21]. To minimize these changes, techniques relying on stress rods and high core ellipticity are used to obtain polarization-maintaining fibers, which induce a large birefringence between principal fiber axes that minimizes polarization crosstalk. As a result, the fiber birefringence can be a simple and useful metric to describe the ability of a fiber to maintain a linear polarization state. However, this value is typically defined at a single wavelength and it does not describe the complex polarization landscape of a broad spectrum generated by nonlinear effects in the fiber [22]. This exhaustive information is hard to access due to the lack of proper experimental equipment to study broadband polarization properties. For example, optical spectrum analyzers (OSAs) typically used to measure spectral power are not able to analyze the polarization states of an SC associated to the principal axes of the fiber. More complex configurations were used to investigate polarization properties, but they were limited to spectra extending over an octave or less [23].

In this work, we use a free-space, broadband, and polarization-resolving spectrometer to fully characterize the spectral and linear polarization properties of an SC generated inside a germania-doped silica PCF. More specifically, we investigate depolarization within a spectral region extending from 450 to 2150 nm as we vary the input polarization and pulse energy. A number of theoretical studies of SC generated in fibers have been performed in an attempt to explore the effect of varying input pulse parameters, birefringence, and fiber length on the state of polarization of the output spectrum [23–25]. These works are complemented by many experimental studies which have focused on studying SC by changing the input polarization and power [23, 24, 26–28], but, until now, there has been no demonstrated technique allowing experimentalists to fully investigate the polarization properties of an ultrabroadband spectrum. In this work, we unveil wavelength-dependent depolarization effects attributed to optical propagation and nonlinear interactions and extract the degree of polarization (DOP) of each spectral component of an SC. To our knowledge, this is the first comprehensive experimental study of the interplay between polarization states in a fiber-based broadband source spanning more than two octaves. We notably report a high DOP toward the edges of the spectrum and a negligible polarization crosstalk during the nonlinear spectral broadening process, even in a low-birefringence fiber. Interestingly, we observe a consistently lower DOP at shorter wavelengths, which can be attributed to a depolarization mechanism associated to Rayleigh-like scattering in the fiber. The novel experimental configuration introduced in this work records polarization components of the spectrum associated to each principal axis of the PCF and reveals wavelength-dependent depolarization processes and features unaccounted for in previous theoretical and experimental studies. We believe such a configuration will help establish new standards for SC characterization and evaluating the polarization maintaining capabilities of optical fibers.

2. Methods

For these experiments, we fabricate a silica-based highly nonlinear PCF with 50 mol% GeO_2-doped core (figure 1). We use a two-step stack and draw method [29] with a central GeO_2-doped core obtained with the procedure described in [30]. Briefly, capillaries are stacked around the solid doped rod, inserted into a jacket and drawn to a 2 mm diameter cane with adjustable pressure controlling the spacing between the end-sealed capillaries to ensure the proper air-clad configuration. The cane is then inserted into an 8 mm outer diameter jacket and the overall size is reduced to a fiber diameter of 125 μm. The final PCF has a loss of $\sim$0.5 dB m^{-1} and a low birefringence $<1 \times 10^{-6}$ at a wavelength of 1030 nm, measured with the cutback technique. A scanning electron micrograph (SEM) image of the PCF is shown in figures 1(a) and (b). The core has an average diameter of 4.7 μm with an ellipticity $\varepsilon = 0.17$, and the air-cladding bridges branching off from the core have a 0.8 μm width. Figure 1(c) shows a relatively high and homogenous doping level of GeO_2 across the core area of the fiber as measured with electron probe microanalysis. The resulting step index $n_{\text{core}} - n_{\text{cladding}} \sim 0.045$ further increases the spatial confinement of light in the core, reducing the modal effective area and enhancing nonlinear effects.

A Yb:KGW ultrafast source is used for SC generation. The laser delivers 185 fs pulses centered at a wavelength of 1030 nm, near the zero-dispersion wavelength of the PCF at 1047 nm. The pulse energy launched into the 0.8 m long PCF is adjusted with a half-wave plate (HWP) and a polarizer, with the HWP angle finely controlled by a motorized rotation mount. A second motorized HWP is located immediately before the fiber to control the input polarization. The coupling efficiency is 40% and it allows us to inject up to 36 nJ pulse energy into the PCF without damaging the input facet. The output SC is collimated with an off-axis parabolic mirror to avoid chromatic aberrations. An ultrabroadband wire grid polarizer with an extinction ratio $>10^4$ between 500 and 2600 nm located in front of the free-space spectrometer selects the linear polarization to be analyzed. Orthogonal polarization components along the vertical (V) and horizontal (H) directions, respectively, corresponding to the transverese electric (TE) and transverse

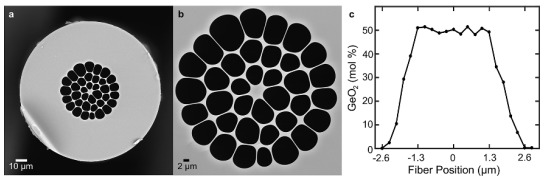

Figure 1. (a) SEM image of the fiber cross-section and (b) the inner photonic crystal structure. (c) The GeO_2 doping distribution in the fiber, measured with electron probe microanalysis.

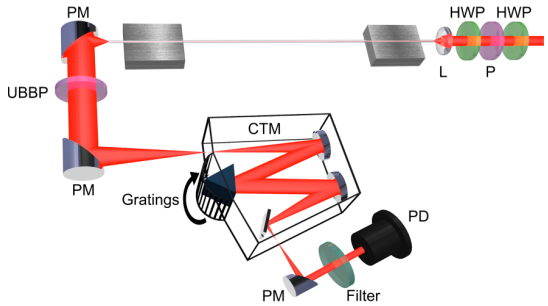

Figure 2. Schematic of the experimental setup. NIR pulses centered at 1030 nm are coupled into the GeO_2-doped PCF for SC generation. The input polarization and pulse energy are controlled with half-wave plates (HWPs) and a polarizer placed before the fiber. The principal axes of the fiber are aligned to the TE and TM modes of the gratings inside the Czerny–Turner monochromator (CTM) by rotating the output end of the PCF. The CTM possesses three gratings, sensitive to different spectral regions, to measure spectra between 400 and 5500 nm. An ultrabroadband polarizer (UBBP) is used to measure linear orthogonal polarization components of the SC independently. P: polarizer; L: lens; PM: parabolic mirror; PD: photodetector.

Table 1. Gratings, spectral filters, and photodiodes used to collect data in four spectral windows and to calibrate the spectrometer.

	Gratings			
Wavelength range (nm)	Lines mm^{-1}	Blaze wavelength (nm)	Spectral filter (long-pass)	Photodetector
400–775	1200	750	None	Si
775–1100	1200	750	750 nm	Si
1100–1800	600	1500	1100 nm	InGaAs
1800–2300	300	3000	1500 nm	InAs

magnetic (TM) modes of the grating inside the spectrometer, are measured successively as we vary the input pulse conditions. The orientation of the end facet of the fiber is adjusted with a rotation mount to ensure that the fiber's principal axes also align with the *V* and *H* orientations. To minimize stress-induced depolarization effects, we keep a 30 cm minimum bend radius and use glue to secure the fiber ends in their respective v-grooves. It has been shown, in previous studies and in our tests, that standard fiber clamping mechanisms using magnets enhance polarization crosstalk due to directional pressure [31]. In this paper, we use the term 'crosstalk' to describe any energy transfer between orthogonally polarized optical components aligned along the principal axes of a fiber.

We resolve the spectral power with a customizable Czerny–Turner configuration monochromator employing three different gratings—allowing for spectroscopic measurements from 400 to 5500 nm. Our system, shown in figure 2, also utilizes three interchangeable photodetectors, sensitive to different regions of the spectrum, and, in some cases, spectral filters that prevent the detection of higher diffraction orders from the grating (see table 1). An off-axis parabolic mirror focuses the SC into the spectrometer and motorized slits ensure a constant spectral resolution of 0.7 nm for all recorded data in our experiments. A lock-in amplifier synchronized to the laser's repetition rate is used to minimize the ambient noise while recording spectra. Finally, the spectrometer is calibrated by applying the response functions of all optical components and gratings in our setup for both *V* and *H* polarization components to the measured SC.

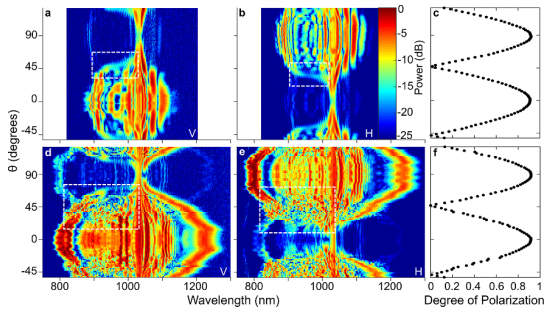

Figure 3. Evolution of the output spectrum as the input polarization (θ) is rotated over 180° with input pulse energies of 0.35 nJ (top row: (a)–(c)) and 1.09 nJ (bottom row: (d)–(f)). Spectral resolution is maintained at 0.7 nm. The degree of polarization, plotted in the right column (c), (f), identifies the principal axes of the PCF for broad SC generation at the maximum value 0.9 for both input pulse energies. White boxes at $\theta = -45°$ and 45° highlight beating in the spectrum.

3. Results and discussion

We first monitor the SC at relatively low input pulse energies (0.35 nJ and 1.09 nJ) while rotating the linear input polarization angle (θ) by 180° (figure 3). The principal axes of the PCF at $\theta = 0°$ and 90° correspond to the maximum spectral broadening. At the lowest input pulse energy (figures 3(a) and (b)), the spectrum splits into multiple closely spaced lobes from the pump ($\lambda = 1030$ nm), indicative of self-phase modulation (SPM). These lobes are still present in the data set taken at higher pulse energy but they are more numerous and they merge to fill in the entire area surrounding the pump at $\theta = 0°$ in figure 3(d) and at $\theta = 90°$ in figure 3(e). This continuous inner section of the spectrum around the pump at 1.09 nJ is framed by a Raman soliton-dispersive wave pair. The similar broadening processes recorded when the input polarization is aligned along either of the two principal axes confirms that the fiber core has a low ellipticity and a small birefringence.

These polarization measurements allow us to clearly trace the dynamics of self-shifting Raman solitons and their corresponding blue-shifted dispersive waves [6]. We confirm that soliton generation occurs independently in each fiber axis [26] since no soliton dynamics are observed at the cross-polarization angles corresponding to $\theta = 90°$ in the V spectra (figures 3(a) and (d)) and $\theta = 0°$ in the H spectra (figures 3(b) and (e)). The cross-polarization geometry also reveals a faint copy of the total output SC. For example, the component at $\lambda = 800$ nm and $\theta = 90°$ in figure 3(d) is less intense, by 15 dB, than the corresponding one in figure 3(e). In the same two figures, the components at $\lambda = 1225$ nm have a difference of 20 dB. We attribute this 'ghost' signal to a depolarization effect due to a small, but non-negligible, mechanical stress applied towards the end part of the PCF as we fix it inside a v-groove. Note that any propagation-induced depolarization mechanisms, such as cross-phase modulation (XPM), would produce a blurred copy of the SC spectrum, since solitons and dispersive waves shift in frequency as they propagate along the fiber. Here, we use glue, instead of magnetic clamps, to hold each fiber end to minimize energy transfer into the orthogonally polarized mode. During tests conducted with magnetic clamps instead of glue, 'ghost' signals were a factor of 3 larger.

Another interesting feature in the spectra of figure 3 can be observed at $\theta = -45°$ and 45° (white boxes), where a beating in the spectrum indicates interference and potential crosstalk between the spectral components guided along both principal axes of the fiber. Figures 3(c) and (f) show the DOP calculated from DOP $= |P_V - P_H|/(P_V + P_H)$, where P_V and P_H are the total powers, integrated across the full measured spectrum, along the V and H directions, respectively. Note that the DOP is not a measure of the optical ellipticity since it does not allow the phase shift between the orthogonal polarization states to be extracted. Since the maximum DOP approaches unity, we can conclude that the fiber can reliably maintain a linear polarization, even in a regime of SC generation extending from 800 to 1200 nm, without a special design inducing stress on the core. More precisely, the maximum value of the DOP is 0.9 at $\theta = 0°$ and 90°, corresponding to the principal axes. Based on the measured 'ghost' signal intensities in figure 3, we can consider a localized decrease in DOP of 0.04 induced by the clamping mechanism at the output end of the fiber. Therefore, depolarization mechanisms due to in-coupling, inhomogeneities, and impurities during optical propagation along the fiber are responsible for a decrease in DOP of 0.06, corresponding to a transfer of 3% of the total energy from one polarization axis to the other.

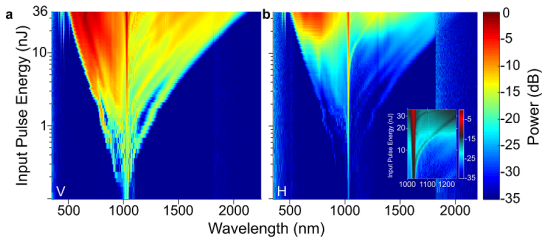

Figure 4. Evolution of the output spectrum in log scale, separated in its (a) V and (b) H components, as we increase the pulse energy launched into the fiber. The input linear polarization was set along one of the principal axes of the fiber ($\theta = 0°$). The inset in figure (b) is plotted in a different color scheme to better visualize the Raman solitons breaking off from the pump in the H axis at 5 nJ and at 25 nJ. Spectral resolution is 0.7 nm across the entire spectrum.

In another experiment, we investigate the input pulse energy dependence of the SC while monitoring both orthogonal output polarization components. Here we fix the input polarization to $\theta = 0°$, corresponding to the highest DOP measured in figure 3. Results are shown in figure 4 as we increase the input pulse energy from 0.1 to 36 nJ. The unperturbed linear polarization is detected in the V direction (figure 4(a)), while cross-polarized components are detected in the H direction (figure 4(b)). We expect analogous results with an input polarization of $\theta = 90°$, considering the similar broadening mechanisms and DOP observed for orthogonal input polarizations shown in figure 3.

As we increase the pulse energy, we observe in the V direction self-shifted Raman solitons breaking off from the pump toward lower frequencies and their corresponding dispersive waves shifting toward higher frequencies [32]. Simultaneously, four-wave mixing broadens the spectral features, flattening out the overall spectrum [26, 32, 33]. As observed in figure 3, the output spectrum in V produces a 'ghost' image in H because of the small depolarization induced by a mechanical stress from the glue holding the output end of the fiber inside the v-groove. For pulse energies below 5 nJ, spectra measured along H mainly feature such 'ghost' images in addition to a peak at the input pump wavelength. However, above this pump energy, the spectrum shows SPM-like broadening and Raman solitons (inset figure 4(b)) indicating that enough pump energy from V is scattered into H to induce strong nonlinear effects.

Using the pulse energy-dependent spectrum measurements in V and H, we calculate the total optical power P_V and P_H in four spectral windows from which we calculate the DOP. Figure 5(a) shows the DOP obtained by integrating the power over the full spectrum, labeled SC; two 10 nm wide bands at 800 nm and 1500 nm, labeled λ short and λ long, respectively; and an 8 nm wide window centered at $\lambda = 1030$ nm corresponding to the pump. The spectral width of these three selected windows is comparable to the input pulse bandwidth and they contain enough data points to average out the experimental noise. At pulse energies below ~10 nJ, the SC line displays a DOP = 0.9, which agrees well with results shown in figures 3(c) and (f). However, at higher pulse energies, the SC line gradually decreases to 0.4. Previous work has attributed this depolarization to nonlinear interactions [24, 34]. Here we establish a more direct correlation between this reduced DOP and a depolarization mechanism acting preferentially on shorter wavelengths, corresponding to the region that contains the larger portion of the optical power. A comparison between the short and long wavelength ranges allows us to expose this wavelength-dependent depolarization mechanism. For instance, the DOP measured in the λ short region is consistently smaller than the one in the λ long region after an input pulse energy of 7 nJ. More importantly, the λ short line already begins to decrease sharply at 5 nJ while the λ long line remains constant, around 0.9, until 15 nJ. Therefore, we can conclude that short wavelengths are more susceptible to depolarization. Interestingly, the pump line remains stable at DOP ~0.5. We attribute the relatively low DOP at the pump wavelength to the nonlinear redistribution of the spectral weight away from the input wavelength in the V polarization from SPM, which occurs even at the lowest pulse energies investigated here, while the scattered signal in the H polarization remains mostly concentrated near the input pump wavelength from depolarization at the input facet of the fiber [35]. These results highlight the importance of evaluating the DOP over the entire spectrum. Simply characterizing the polarization state at the pump wavelength can lead to false conclusions about the polarization properties of an SC source; especially when considering spectra spanning more than an octave.

Figure 5(b) shows the DOP calculated for each spectral component. Here, instead of integrating the spectra to extract P_V and P_H and calculate the DOP, the spectra in figure 4, labeled $S_V(\lambda)$ and $S_H(\lambda)$ for the spectra in figures 4(a) and (b), respectively, are used directly to calculate the DOP spectrum for all pulse

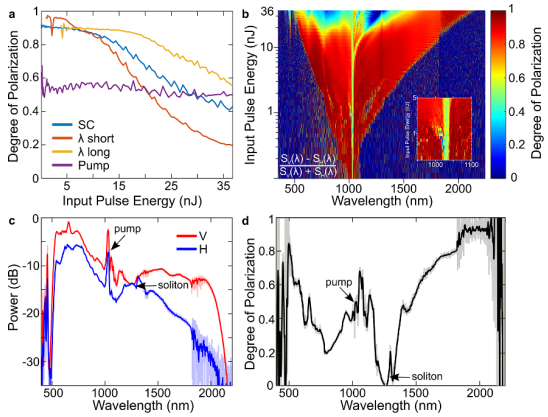

Figure 5. (a) The degree of polarization calculated by integrating the entire spectrum (SC) and various bands (λ short, λ long, pump) along both V and H directions for different input pulse energies. (b) The degree of polarization of every spectral component calculated with the surface plots in figure 4. The inset indicates where broadening in H begins. (c) The output spectra at the highest input pulse energy from figures 4(a), (b) and (d) the corresponding DOP attributed to each spectral component. Dark lines are the averaged spectra while the faint lines represent the relative noise. Larger noise in the spectral window from 1800 to 2300 nm is due to a smaller slits size (to maintain a constant spectral resolution) and the resulting lower detected intensity. Arrows labeled soliton indicate the spectral position of self-shifted Raman solitons generated from nonlinear effects acting on the signal in the H polarization, while arrows labeled pump indicate the input wavelength.

energies. The surface plot reveals not only the overall depolarization trends, but also fine depolarization-related features. For example, at input pulse energies exceeding 5 nJ, we can distinguish a red-shifting spectral region of low DOP corresponding to a Raman soliton in the H polarization. At 1 nJ, we also trace the depolarization of a gradually blue-shifting component from the pump wavelength (see inset in figure 5(b)). We observe, for all input pulse energies, that the spectral edges of the SC consistently correspond to a localized DOP approaching unity [23, 27]. This result is to be expected because of the nature of nonlinear spectral broadening in optical fibers: shortest and longest wavelengths are generated towards the end facet of the fiber and are thus less susceptible to depolarization effects during optical propagation. The large DOP at the edges of the spectrum is reproduced by numerical simulations (figure S2, supplementary material (available online at stacks.iop.org/JPPHOTON/3/025002/mmedia)) that solve the coupled nonlinear Schrödinger equations, calculate the output spectrum as a function of propagation length in the PCF, and extract the DOP at each wavelength while considering linear and nonlinear depolarization mechanisms. Figure 5(b) also shows, at high pulse energies, a significant decrease of the DOP between 800 and 1400 nm. We can attribute this low DOP to the spectral broadening of the H polarized component, which notably features self-shifting Raman soliton dynamics above 5 nJ.

Figure 5(c) shows the output spectrum in the V and H polarization at the highest pump energy used in the experiment (36 nJ). In the V direction, the SC extends from 450 to 2150 nm at a 30 dB cutoff. The SC measured in the H polarization is slightly narrower and shows a pronounced spectral asymmetry caused by a preferential depolarization of the short wavelength components. The arrow labeled soliton indicates the spectral position of self-shifted Raman solitons in the H polarized signal (see inset of figure 4(b)). The same arrow in figure 5(d) shows a correspondingly low DOP at the same position. The solitons propagate with the same polarization state as the light that generated them [36]. Since the PCF has a relatively low birefringence, the intensity-dependent refractive index associated to a soliton may increase the effective linear birefringence, and therefore reduce depolarization occurring via scattering events. This phenomenon was previously described in a context of a beam injected along the slow axis of a birefringent fiber [37]. This effect could explain the low level of depolarization observed during solitonic propagation and the resulting complex polarization landscape (figure 5(d)) at high power when both orthogonal components independently generated Raman solitons. Figure 5(d) also allows us to clearly observe larger DOP values at longer wavelengths, in comparison to the values at shorter wavelengths, which remain below 0.6.

Lower DOP values at shorter wavelengths shown in figures 5(a) and (d), are consistent with a wavelength-dependent depolarization mechanism, which can be attributed to a Rayleigh scattering effect preferentially acting on shorter wavelengths propagating in the fiber. Such mechanism was previously

proposed to account for the depolarization in fiber communication systems [38]. In our experiment, this effect becomes especially important at high input pulse energies where a large fraction of the optical energy in V is shifted to the visible region. Numerical simulations (figure S3, supplementary material) establish that linear (scattering effects) and nonlinear (XPM) depolarization mechanisms do not fully explain the wavelength-dependent depolarization we observe experimentally in this work. Note that our results do not directly correlate with the signature λ^{-4}-dependence of Rayleigh scattering caused by emitters smaller than the wavelength. We believe it can be in part attributed to depolarization effects caused by defects of different sizes in the fiber and also to the spatial mode distribution at shorter wavelengths, which is better confined in the center of the core and therefore less sensitive to structural deformations occurring at the air-core interface.

4. Conclusion

In this work, we introduce a novel technique to measure the SC generated in each fiber axis of a highly nonlinear fiber and investigate wavelength-dependent polarization properties. We collect output spectra for varying input polarization states and pulse energies, allowing us to confirm that Raman soliton and dispersive wave generation remain axis-specific as they propagate along our low-birefringent PCF. Measurements also reveal that the edges of the SC have a consistently larger DOP than the central region near the pump. More specifically, we identify a depolarization mechanism indicative of Rayleigh-like scattering preferentially reducing the DOP at shorter wavelengths. In summary, our results and analysis show the importance of characterizing the polarization properties of every spectral component when using fiber-based broadband radiation. Such information is not attainable using conventional measurement techniques based on standard OSAs. We believe that our versatile experimental configuration is the most accurate method to date for quantifying the polarization maintaining ability of optical fibers, as it provides an in-depth understanding of the relationship between spectral broadening and depolarization effects over all frequencies of an SC. In the future, elliptical-sensitive detection could be readily implemented in such a setup to allow for the full polarization characterization of each spectral component. This system could then retrieve a relevant set of parameters to describe twisted fibers, which are optimized to guide circularly polarized light and exhibit exotic polarization properties [39, 40].

Acknowledgments

The authors are grateful for the technical assistance provided by Shyamal Das, Anirban Dhar and Mrinmay Pal to fabricate the photonic crystal fiber. We also acknowledge the NSERC-Canada Graduate Scholarship, Ontario Graduate Scholarship, NSERC Discovery program and the Canada Foundation for Innovation (Project Number 35269). Professor A K Kar would like to acknowledge the support of UK Engineering and Physical Sciences Research Council (Project CHAMP, EP/M015130/1). Dr M C Paul acknowledges the support of CSIR-CGCRI and the DST-Inspired Research (INSPIRE) Fellowship (IF150744) as well as the Newton-Bhabha Fellowship of P H Reddy awarded by the British Council, UK.

ORCID iDs

Nicolas Couture https://orcid.org/0000-0002-7137-8102
Rachel Ostic https://orcid.org/0000-0002-1634-0478
P Harshavardhan Reddy https://orcid.org/0000-0002-8799-6060
Mukul Chandra Paul https://orcid.org/0000-0001-8805-6129
Jean-Michel Ménard https://orcid.org/0000-0002-6458-758X

References

[1] Jiao K *et al* 2019 Mid-infrared flattened supercontinuum generation in all-normal dispersion tellurium chalcogenide fiber *Opt. Express* **27** 2036–43
[2] Jiang Z, Wang T, Sun Z, Chen J, Zhang X, Lin P, Chen P and Zhao Y 2019 Partially coherent seeding of supercontinuum generation in picosecond regime *Opt. Laser Technol.* **120** 105752
[3] Poudel C and Kaminski C F 2019 Supercontinuum radiation in fluorescence microscopy and biomedical imaging applications *J. Opt. Soc. Am.* B **36** A139–A153
[4] Borondics F, Jossent M, Sandt C, Lavoute L, Gaponov D, Hideur A, Dumas P and Février S 2018 Supercontinuum-based Fourier transform infrared spectromicroscopy *Optica* **5** 378–81
[5] Dupont S, Petersen C, Thøgersen J, Agger C, Bang O and Keiding S R 2012 IR microscopy utilizing intense supercontinuum light source *Opt. Express* **20** 4887–92

[6] Travers J C, Chang W, Nold J, Joly N Y and Russell P S J 2011 Ultrafast nonlinear optics in gas-filled hollow-core photonic crystal fibers [Invited] *J. Opt. Soc. Am.* B **28** A11–A26
[7] Köttig F, Novoa D, Tani F, Günendi M C, Cassataro M, Travers J C and Russell P S J 2017 Mid-infrared dispersive wave generation in gas-filled photonic crystal fibre by transient ionization-driven changes in dispersion *Nat. Commun.* **8** 813
[8] Cassataro M, Novoa D, Günendi M C, Edavalath N N, Frosz M H, Travers J C and Russell P S J 2017 Generation of broadband mid-IR and UV light in gas-filled single-ring hollow-core PCF *Opt. Express* **25** 7637–44
[9] Belli F, Abdolvand A, Chang W, Travers J C and Russell P S J 2015 Vacuum-ultraviolet to infrared supercontinuum in hydrogen-filled photonic crystal fiber *Optica* **2** 292–300
[10] Qin G, Yan X, Kito C, Liao M, Chaudhari C, Suzuki T and Ohishi Y 2009 Ultrabroadband supercontinuum generation from ultraviolet to 6.28 μm in a fluoride fiber *Appl. Phys. Lett.* **95** 161103
[11] Swiderski J, Michalska M and Mazé G 2013 Mid-IR supercontinuum generation in a ZBLAN fiber pumped by a gain-switched mode-locked Tm-doped fiber laser and amplifier system *Opt. Express* **21** 7851–7
[12] Xia C, Kumar M, Kulkarni O P, Islam M, Terry J F L, Freeman M J, Poulain M and Mazé G 2006 Mid-infrared supercontinuum generation to 4.5 μm in ZBLAN fluoride fibers by nanosecond diode pumping *Opt. Lett.* **31** 2553–5
[13] Jiang X, Joly N Y, Finger M A, Babic F, Wong G K L, Travers J C and Russell P S J 2015 Deep-ultraviolet to mid-infrared supercontinuum generated in solid-core ZBLAN photonic crystal fibre *Nat. Photon.* **9** 133–9
[14] Saghaei H, Moravvej-Farshi M K, Ebnali-Heidari M and Moghadasi M N 2016 Ultra-wide mid-infrared supercontinuum generation in $As_{40}Se_{60}$ chalcogenide fibers: solid core PCF versus SIF *IEEE J. Sel. Top. Quantum Electron.* **22** 279–86
[15] Wei D P, Galstian T V, Smolnikov I V, Plotnichenko V G and Zohrabyan A 2005 Spectral broadening of femtosecond pulses in a single-mode As–S glass fiber *Opt. Express* **13** 2439–43
[16] Kubat I *et al* 2014 Mid-infrared supercontinuum generation to 12.5 μm in large NA chalcogenide step-index fibres pumped at 4.5 μm *Opt. Express* **22** 19169–82
[17] Hudson D D, Antipov S, Li L, Alamgir I, Hu T, Amraoui M E, Messaddeq Y, Rochette M, Jackson S D and Fuerbach A 2017 Toward all-fiber supercontinuum spanning the mid-infrared *Optica* **4** 1163–6
[18] Yang L, Zhang B, Yin K, Yao J, Liu G and Hou J 2016 0.6–3.2 μm supercontinuum generation in a step-index germania-core fiber using a 4.4 kW peak-power pump laser *Opt. Express* **24** 12600–6
[19] Jain D, Sidharthan R, Moselund P M, Yoo S, Ho D and Bang O 2016 Record power, ultra-broadband supercontinuum source based on highly GeO_2 doped silica fiber *Opt. Express* **24** 26667–77
[20] Monerie M and Jeunhomme L 1980 Polarization mode coupling in long single-mode fibre *Opt. Quantum Electron.* **12** 449–61
[21] de Boer J F, Hitzenberger C K and Yasuno Y 2017 Polarization sensitive optical coherence tomography—a review [Invited] *Biomed. Opt. Express* **8** 1838–73
[22] Herrera R A 2017 Influence of the wavelength dependence of birefringence in the generation of supercontinuum and dispersive wave in fiber optics *Math. Probl. Eng.* **2017** 3517407
[23] Zhu Z and Brown T G 2004 Experimental studies of polarization properties of supercontinua generated in a birefringent photonic crystal fiber *Opt. Express* **12** 791–6
[24] Tu H, Liu Y, Liu X, Turchinovich D, Lægsgaard J and Boppart S A 2012 Nonlinear polarization dynamics in a weakly birefringent all-normal dispersion photonic crystal fiber: toward a practical coherent fiber supercontinuum laser *Opt. Express* **20** 1113–28
[25] Chao Q and Wagner K H 2015 Polarization instability of Raman solitons ejected during supercontinuum generation *Opt. Express* **23** 33691–704
[26] Proulx A, Ménard J-M, Hô N, Laniel J M, Vallée R and Paré C 2003 Intensity and polarization dependences of the supercontinuum generation in birefringent and highly nonlinear microstructured fibers *Opt. Express* **11** 3338–45
[27] Tarnowski K, Martynkien T, Mergo P, Poturaj K, Anuszkiewicz A, Béjot P, Billard F, Faucher O, Kibler B and Urbanczyk W 2017 Polarized all-normal dispersion supercontinuum reaching 2.5 μm generated in a birefringent microstructured silica fiber *Opt. Express* **25** 27452–63
[28] Sopalla R P, Wong G K L, Joly N Y, Frosz M H, Jiang X, Ahmed G and Russell P S J 2019 Generation of broadband circularly polarized supercontinuum light in twisted photonic crystal fibers *Opt. Lett.* **44** 3964–7
[29] Jiang X, Euser T G, Abdolvand A, Babic F, Tani F, Joly N Y, Travers J C and Russell P S J 2011 Single-mode hollow-core photonic crystal fiber made from soft glass *Opt. Express* **19** 15438–44
[30] Reddy P H, Kir'yanov A V, Dhar A, Das S, Dutta S, Pal M, Barmenkov Y M, Minguella-Gallardo J A, Bhadra S K and Paul M C 2017 Fabrication of ultra-high numerical aperture GeO_2-doped fiber and its use for broadband supercontinuum generation *Appl. Opt.* **56** 9315–24
[31] Noda J, Okamoto K and Sasaki Y 1986 Polarization-maintaining fibers and their applications *J. Lightwave Technol.* **4** 1071–89
[32] Dudley J M, Genty G and Coen S 2006 Supercontinuum generation in photonic crystal fiber *Rev. Mod. Phys.* **78** 1135
[33] Dudley J M and Taylor R 2010 *Supercontinuum Generation in Optical Fibers* (Cambridge: Cambridge University Press) (https://doi.org/10.1017/CBO9780511750465)
[34] Domingue S R and Bartels R A 2013 Overcoming temporal polarization instabilities from the latent birefringence in all-normal dispersion, wave-breaking-extended nonlinear fiber supercontinuum generation *Opt. Express* **21** 13305–21
[35] Chick B J, Chon J W M and Gu M 2008 Polarization effects in a highly birefringent nonlinear photonic crystal fiber with two-zero dispersion wavelengths *Opt. Express* **16** 20099–105
[36] Flores-Rosas A, Peralta-Hernandez J I, Bracamontes-Rodríguez J E, Villagomez-Bernabe B A, Beltrán-Pérez G, Pottiez O, Ibarra-Escamilla B, Rojas-Laguna R and Kuzin E A 2014 Observation of a high grade of polarization of solitons generated in the process of pulse breakup in a twisted fiber *J. Opt. Soc. Am.* B **31** 821–6
[37] Winful H G 1986 Polarization instabilities in birefringent nonlinear media: application to fiber-optic devices *Opt. Lett.* **11** 33–35
[38] Barfuss H and Brinkmeyer E 1986 Polarization holding and anisotropic Rayleigh scattering in birefringent single-mode fibers *J. Opt. Soc. Am.* A **3** 426–31
[39] Palmieri L 2006 Polarization properties of spun single-mode fibers *J. Lightwave Technol.* **24** 4075–88
[40] Wong G K L, Kang M S, Lee H W, Biancalana F, Conti C, Weiss T and Russell P S J 2012 Excitation of orbital angular momentum resonances in helically twisted photonic crystal fiber *Science* **337** 446–9

Polarization-resolved supercontinuum generated in a germania-doped photonic crystal fiber: supplementary material

NICOLAS COUTURE[1], RACHEL OSTIC[1], P. HARSHAVARDHAN REDDY[2,3], AJOY KUMAR KAR[4], MUKUL CHANDRA PAUL[3] AND JEAN-MICHEL MÉNARD[1,*]

[1] Department of Physics, University of Ottawa, Ottawa, ON K1N 6N5, Canada
[2]Academy of Scientific and Innovative Research, CSIR-CGCRI Campus, Kolkata 700032, India
[3]Fiber Optics and Photonics Division, CSIR-CGCRI Campus, Kolkata 700032, India
[4]Institute of Photonics and Quantum Sciences, Heriot-Watt University, Riccarton Campus, Edinburgh EH14 4AS, UK

*E-mail: jean-michel.menard@uottawa.ca

Abstract

This document provides supplementary information to "Polarization-resolved supercontinuum generated in a germania-doped photonic crystal fiber". We simulate the spectrum of the laser pulse in the fiber as a function of its propagation length for different input pulse energies used in our experiments and provide the parameters required to reproduce these numerical simulations. We calculate the degree of polarization of the output spectrum assuming a linear polarization mode coupling term and nonlinear coupling between two polarization components, each aligned with one of the fiber's principal axes.

Main

In this supplement, we solve coupled generalized nonlinear Schrödinger equations that describe the propagation of two near-degenerate orthogonal polarization modes within an optical fiber. The polarization modes correspond to the fiber's principal axes, which we consider aligned along the *x* and *y* directions. The equations to solve [1] are:

$$\frac{\partial A_x}{\partial z}+\frac{\alpha}{2}A_x+\frac{\Delta\beta}{2}\frac{\partial A_x}{\partial t}-\sum_{k\geq 2}\frac{i^{k+1}}{k!}\beta_k\frac{\partial^k A_x}{\partial t^k}-\epsilon A_y = i\gamma\left(1+\frac{i}{\omega_0}\frac{\partial}{\partial t}\right)\left\{(1-f_R)\left[A_x\left(|A_x|^2+\frac{2}{3}|A_y|^2\right)+\frac{i\gamma}{3}A_x^*A_y^2e^{-2i\Delta\beta z}\right]+f_R R_x\right\} \quad (1)$$

$$\frac{\partial A_y}{\partial z}+\frac{\alpha}{2}A_y+\frac{\Delta\beta}{2}\frac{\partial A_y}{\partial t}-\sum_{k\geq 2}\frac{i^{k+1}}{k!}\beta_k\frac{\partial^k A_y}{\partial t^k}-\epsilon^* A_x = i\gamma\left(1+\frac{i}{\omega_0}\frac{\partial}{\partial t}\right)\left\{(1-f_R)\left[A_y\left(|A_y|^2+\frac{2}{3}|A_x|^2\right)+\frac{i\gamma}{3}A_y^*A_x^2e^{-2i\Delta\beta z}\right]+f_R R_y\right\} \quad (2)$$

where A_x and A_y refer respectively to the slowly varying amplitudes in the *x* and *y* polarization states. On the left side of the equations are the linear terms: α is the fiber loss, $\Delta\beta$ is the birefringence [2,3], β_k are polynomial expansion coefficients of the fiber dispersion, and ϵ is the polarization mode coupling coefficient [4]. The right sides contain the nonlinear terms. The (1-f_R) contribution is the instantaneous response with nonlinear coefficient γ. The remaining f_R

term accounts for its Raman response, taking into account parallel and perpendicular components of the response [1]. The expression for R_x form is as follows:

$$R_x = A_x \int h_R^{new}(t')|A_x(z,t-t')|^2 dt' + f_a A_x \int h_a(t')\left|A_y(z,t-t')\right|^2 dt' + \frac{f_b}{2} A_y \int h_b(t')\left[A_x(z,t-t')A_y^*(z,t-t') + A_x^*(z,t-t')A_y(z,t-t')e^{-2i\Delta\beta z}\right]dt' \quad (3)$$

Note that the x and y indices can be swapped to give the expression for R_y. The form of the Raman response has two components, h_a and h_b, defined as follows [1]:

$$h_R^{new} = f_a h_a + f_b h_b \quad (4)$$

$$h_a = \frac{\tau_1^2 + \tau_2^2}{\tau_1 \tau_2^2} e^{-t/\tau_2} \sin(t/\tau_1) \quad (5)$$

$$h_b = \frac{2\tau_b - t}{\tau_b^2} e^{-t/\tau_b} \quad (6)$$

Using the transformations defined in [5], we transform the equation into the frequency domain with a phase based on the fiber dispersion to yield a convenient form to solve numerically. We build on previous work [2,5-7] by integrating additional terms that affect polarization and cross-coupling.

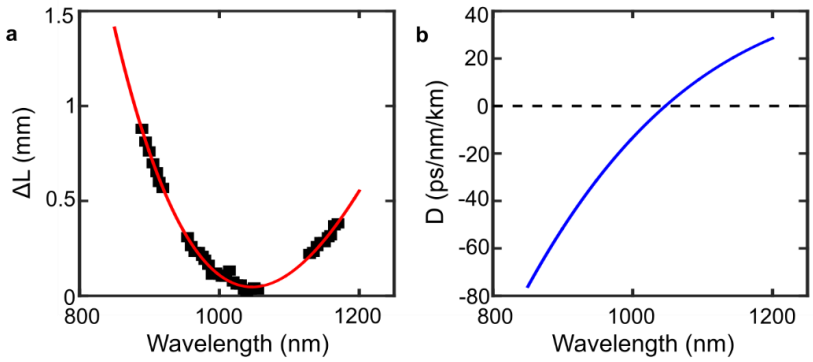

Figure S1. **Dispersive properties of the PCF.** a) A Mach-Zehnder interferometer (MZI) using 70 cm of the PCF in one of its arms and three laser diodes operating in the spectral windows 875 to 925 nm, 950 to 1060 nm, and 1125 to 1175 nm measures the difference in optical propagation length ΔL (black squares) in the PCF as a function of wavelength. b) The resulting fiber dispersion is calculated using methods described in [8].

Parameters are adapted to the fiber used in our experiments. The fiber length is set to 0.8 m. The dispersion curve is modelled numerically based on a polynomial expansion fitted to the dispersion measured between 875 nm and 1175 nm in Fig. S1a and plotted in Fig. S1b. The values are: $\beta_2 = 1.8\times10^{-3}$ ps^2/m, $\beta_3 = 8.6\times10^{-5}$ ps^3/m, $\beta_4 = -7.8\times10^{-8}$ ps^4/m, $\beta_5 = -1.1\times10^{-10}$ ps^5/m. The birefringence, measured with cut-off measurements, is approximately $\Delta\beta = 1\times10^{-6}$. We only consider the first order terms in $\Delta\beta$ in Eqs. 1 and 2. Higher order terms can be considered negligible [1,7]. For properties that were not measured experimentally, we refer to the fiber geometry, composition, and previous studies to estimate appropriate values. The nonlinear index of refraction is set to 5.2×10^{-20} m^2/W based on the 50% concentration of germania measured in the PCF core [9], yielding a nonlinear coefficient $\gamma = 0.0063$ W^{-1}m^{-1}.

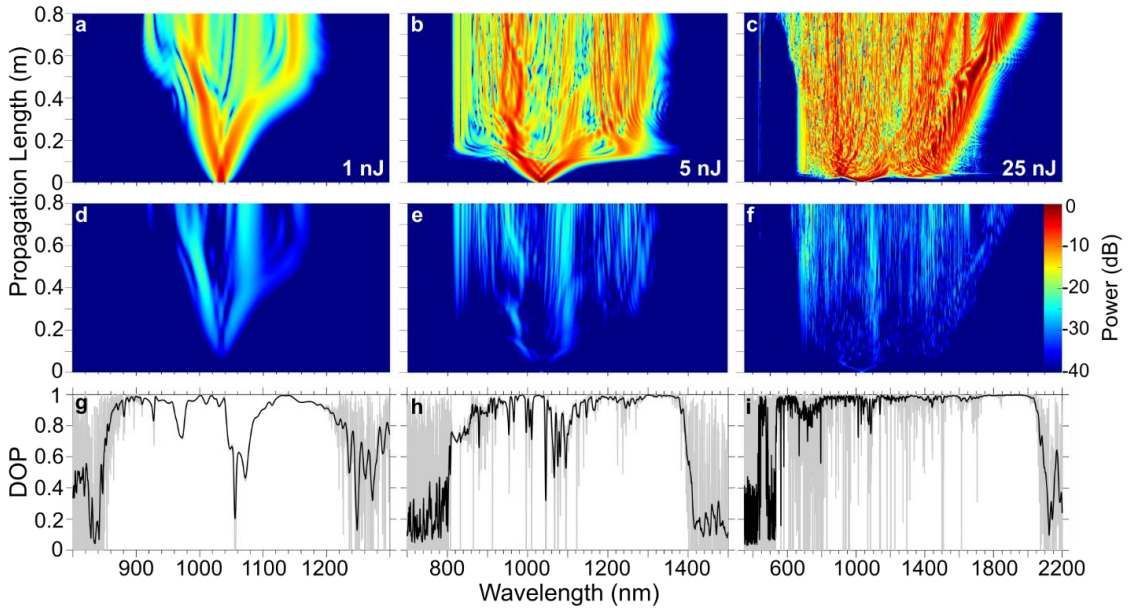

Figure S2. **Simulation results.** Spectrum in the *x* (a-c) and *y* (d-f) axes as a function of propagation length inside the weakly birefringent germania-doped PCF. (g-i) The output DOP spectrum calculated from the output spectra in a-f. Simulations and DOP are plotted for input pulse energies of 1 nJ (left column), 5 nJ (middle column), and 25 nJ (right column).

An effective mode area of 50 μm^2, consistent with the SEM image, provides a spectral bandwidth that closely matches experimental data. We neglect loss in the fiber. The simulation includes a harmonic oscillator model for the Raman response of the material with fractional contribution $f_R = 0.24$ [1] and $\tau_1 = 12.2$ fs, similar for both SiO_2 and GeO_2 [10,11], while $\tau_2 = 65$ fs is taken from [10], which also uses a germania-doped fiber. This τ_2 value is between the values for pure silica (~35 fs) and germania (85 fs) [11], as the fiber contains 50% GeO_2 in the core (Fig. 1c of the main manuscript). The non-oscillatory Raman timescale is $\tau_b = 96$ fs with $f_B = 0.21 = 1 - f_A$. We use polarization mode coupling coefficient $\epsilon = 0.6$ m^{-1}.

The input pulse is of Gaussian temporal shape with a duration of 185 fs FWHM and an initial polarization state (θ in main manuscript) 1° off the *x* axis to reproduce experimental uncertainty. We study the SC generation at three different input pulse energies of 1 nJ, 5 nJ, and 25 nJ as shown in Fig. S2. Like in our experimental measurements, the initial broadening mechanism is dominated by self-phase modulation, with the spectrum splitting into two lobes. With increasing pulse energy, Raman solitons become evident as they red-shift, branching off from the pump. A key observation is that the spectral broadening occurs on a shorter length scale as the input pulse energy increases. Starting at 5 nJ, the spectral broadening occurs almost exclusively within the first 15 cm of propagation in the fiber, though the long and short wavelength edges do continue to extend gradually as they travel along the rest of the fiber. This supports our observation that the spectral region centered at the pump wavelength has the greatest propagation length over which to depolarize. We illustrate this claim by estimating the DOP across the spectrum in Figs. S2 g-i.

Note that an incoherent spectral background set at 0.001% of the maximum input pulse amplitude is added to both orthogonal polarization components to create the noise floor. Figure S2 shows for all input pulse energies that the spectral edges of the generated SC conserve the highest DOP. This result is in agreement with our experimental results.

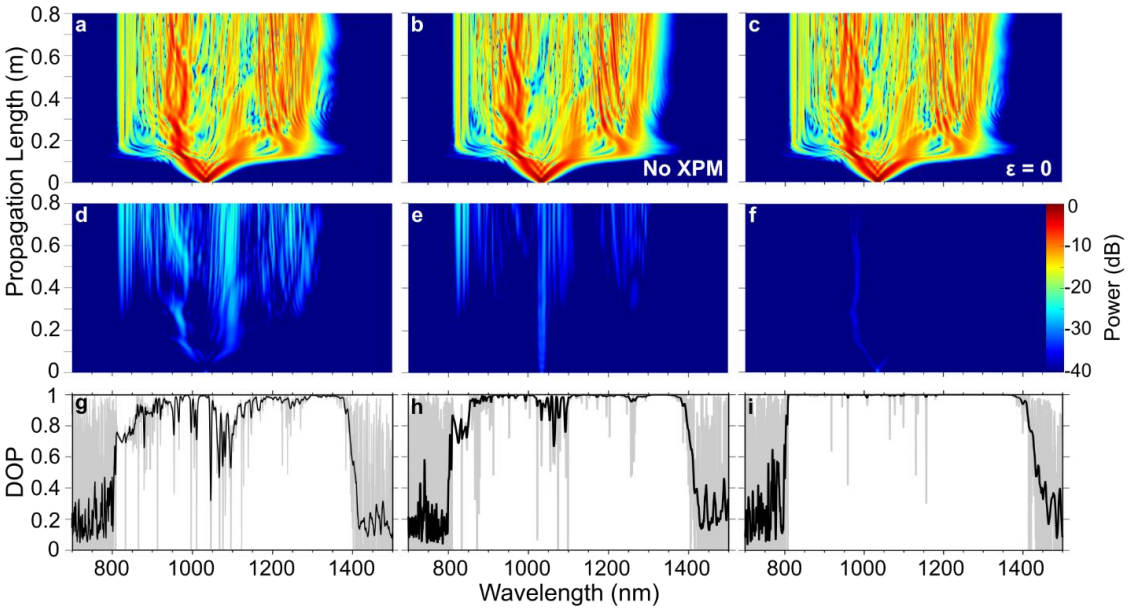

Figure S3. **Depolarization.** Spectrum in the *x* (a-c) and *y* (d-f) axes as a function of propagation length with an input pulse energy of 5 nJ along with the associated DOP spectra (g-i). Left column: linear and nonlinear depolarization mechanisms are considered. Middle column: purely linear depolarization is considered (no XPM). Right column: purely nonlinear depolarization is considered ($\epsilon = 0$).

In another set of simulations, shown in Fig. S3, we study the strength of depolarization arising from linear and nonlinear effects while keeping the input pulse energy fixed at 5 nJ. In the left column, we run our simulations with both linear ($\epsilon \neq 0$) and nonlinear (XPM) depolarization, identical to the middle column of Fig. S2. In the middle column of Fig. S3, we repeat the simulations with only the linear depolarization component ($\epsilon \neq 0$ and no XPM). The corresponding DOP spectrum in Fig. S3h bears a similar form as that in Fig. S3g, with only a difference in amplitude. Finally, in the right column, we repeat the simulations with purely nonlinear depolarization ($\epsilon = 0$ and with XPM). Here, only the most intense section of the spectrum in Fig. S3c (near 975 nm) depolarizes into the *y* axis (Fig. S3f), as is commonly expected with nonlinear effects. The result is a relatively flat DOP completely polarized in the *x* direction.

For our configuration, where the input pulse has a linear polarization aligned along one of the principal fiber axes, numerical simulations show that the overall depolarization is dominated by linear mechanisms and not XPM. These results support the discussion surrounding Fig. 5 of the main manuscript. Although most of the spectral power in our experiments lies in the short wavelength region, simulations show that XPM alone cannot account for a significant depolarization in this spectral region.

References

1. Agrawal G P 2019 *Nonlinear Fiber Optics 6th edn* (Academic Press)
2. Tu H, Liu X, Turchinovich D, Lægsgaard J and Boppart S A 2012 Nonlinear polarization dynamics in a weakly birefringent all-normal dispersion photonic crystal fiber: toward a practical coherent fiber supercontinuum laser *Opt. Express* **20** 1113-1128
3. Zhu Z and Brown T G 2004 Polarization properties of supercontinuum spectra generated in birefringent photonic crystal fibers *J. Opt. Soc. Am. B* **21** 249–257
4. Monerie M and Jeunhomme L 1980 Polarization mode coupling in long single-mode fibres *Opt. Quant. Electron.* **12** 449–461
5. Dudley J M and Taylor J R 2010 *Supercontinuum Generation in Optical Fibers*. (Cambridge University Press)
6. Dudley J M, Genty G and Coen S 2006 Supercontinuum generation in photonic crystal fiber *Rev. Mod. Phys.* **78** 1135

7. Ghosh A N, Meneghetti M, Peterson C R, Bang O, Brilland L, Venck S, Troles J, Dudley J M and Sylvestre T 2019 Chalcogenide-glass polarization-maintaining photonic crystal fiber for mid-infrared supercontinuum generation *J. Phys. Photonics* **1** 044003
8. Akhmetshin U G, Bogatyrev V A, Senatorov A K, Sysolyatin A A and Salygin M G 2003 New single-mode fibres with the flat spectral dependence of the chromatic dispersion varying over the fibre length *Quant. Electron.* **33** 265
9. Wada A, Okude S, Sakai T and Yamauchi R 1996 GeO_2 Concentration Dependence of Nonlinear Refractive Index Coefficients of Silica-Based Optical Fibers *Electron. Commun. Jpn.* **79** Part 1
10. Kieu K, Schneebeli L, Hales J M, Perry J W, Norwood R A and Peyghambarian N 2011 Demonstration of Zeno switching through inverse Raman scattering in an optical fiber *Opt. Express* **19** 12532-12539
11. Rottwitt K and Povlsen J H 2005 Analyzing the Fundamental Properties of Raman Amplification in Optical Fibers *J. Lightwave Technol.* **23** 3597-3605

Chapter 7

Conclusions and outlook

In conclusion, this thesis has summarized four projects which demonstrate the versatility of optical fibers and how they can be used to solve common issues plaguing time-resolved THz systems.

In chapter 2, we presented background information on the physical processes pertinent to this thesis. Namely, we provided the framework of ultrashort pulse propagation in optical fibers, highlighting how certain nonlinear effects, like SPM, and linear effects, like GVD, sculpt NIR pulses as they propagate in an optical fiber. We also explored how the balance between nonlinear and linear effects combined with the dispersion-engineered fibers can allow soliton-dispersive wave pair formation and produce a SC. Finally, we described physical processes behind THz generation and detection in electro-optic crystals, along with their phase matching considerations, and how we can extract information of a material from experimentally acquired THz waveform data.

In chapter 3, we elaborated on experimental techniques that are not typically described in the literature. This included technical considerations when coupling into an optical fiber and steps for initial alignment of a time-resolved THz system. We also characterized the pulse properties of the ultrafast source used for much of the work presented in this thesis with intensity autocorrelation and frequency-resolved optical gating.

In chapter 4, we showed how optical fibers can be used to enable single-pulse THz spectroscopy up to a rate of 50 kHz, where we were only limited by the ultrafast source available to us in the laboratory. Here, we used standard fibers to generate a chirped SC and to per-

form photonic time-stretch technique, mapping out the spectrum of a THz-encoded NIR SC to the time domain with fast electronics. With this system, we investigated carrier dynamics as successive NIR pump pulses populated a silicon wafer with carriers, attenuating the transmitted THz pulse more significantly with each pump pulse until a saturation density was reached. With the simple addition of an optical chopper to the pump beam line, we were also able to passively observe carrier recombination without mechanically scanning a delay line.

Further improvements to this system will drastically improve the dynamic range. Although the PMF used for SC generation was satisfactory in terms of bandwidth and noise level, the use of more sophisticated fibers, like the chiral PCF described in [44], would be more ideal. The wider achievable NIR bandwidth from this fiber will drastically improve the temporal resolution, allowing us to resolve higher THz frequencies and thus perform single-pulse THz spectroscopy over a wider spectral range. The lower noise from this fiber will also yield a more stable SC on a pulse-to-pulse basis. Finally, this fiber in combination with a balanced photonic time-stretch technique similar to the technique described in [89] will significantly increase the dynamic range of our single-pulse spectroscopy scheme as pulse-to-pulse fluctuations from the laser source will be cancelled out. One can also consider reducing the complexity of the system without sacrificing performance. The THz generation scheme in the current system relies on the tilted-pulse-front technique in lithium niobate as described in section 4.1. This technique, though reliable and well-studied, requires great care in alignment. Slight misalignment in the THz generation configuration can therefore cost us dearly in THz field strength impinging on the detection crystal. Organic crystals have emerged themselves as prime candidates for high-field THz generation at high repetition rates. Their high electro-optic coefficients ($\chi^{(2)}$) combined with their favorable phase matching conditions at NIR frequencies allows us to generate similar THz field strengths as the tilted-pulse-front technique without the complex geometry [130, 131, 132, 133].

Future work with this single-pulse THz spectroscopy system is exciting. Resolving microsecond dynamics with classical methods relying on mechanical delay stages is a technical challenge as microsecond time delays require km-long delay lines. Moreover, classical methods are not sensitive to irreversible or chaotic dynamics as they intrinsically rely on averaging over numerous pulses and require the successive THz pulses to probe the same state after, say, optical excitation. With the system we developed here, we aim to resolve more complex phenomena occurring within materials or samples. Notably, it has been

shown that enzyme dynamics occur on microsecond timescales [134, 135]. Revealing these types of dynamics can provide a new insight into underlying physical and chemical processes that have yet to be experimentally resolved, paving the way towards new discoveries and application in all fields of research.

This single-pulse THz spectroscopy scheme can also be quite impactful in an industrial setting. It is currently impractical to use THz spectroscopy as a method for non-invasive quality control since standard THz detection techniques are too slow to keep up with assembly lines. In the pharmaceutical industry, determining the thickness and uniformity of the coating surrounding active pharmaceutical ingredients in tablets is a crucial component of the quality control process [136]. Moreover, the porosity of individual tablets, which directly affects the transport properties of the active ingredient, is also a feature of individual tablets that can be resolved with THz spectroscopy [137]. Extracting as much information as possible of individual tablets can reduce production costs and provide consumers with more trust in the tablets they are purchasing and ingesting [138]. The ability to perform THz spectroscopy at arbitrary rates, like we demonstrated at a rate of 50 kHz, opens the door to performing non-invasive quality control of individual tablets without sacrificing the tablet manufacturing rate, a feature that is quite desirable to pharmaceutical companies. Finally, although it was not discussed in this thesis, applying this technology to single-pixel THz imaging could be an interesting research venture to image interesting samples in real-time and accelerate the raster scanning process [139, 140].

In chapter 5, we used optical fibers and a chirped mirror pair to overcome spectral bandwidth limitations of ultrafast NIR sources to provide the NIR spectral bandwidth and pulse duration necessary for broadband THz generation and detection. This included using a standard polarization-maintaining fiber to build a compact and portable time-domain THz system with a THz spectrum reaching 6 THz, and an argon-filled kagomé HCPCF to generate THz pulses with spectra beyond 20 THz.

Further development of the compact THz spectrometer, namely a detection scheme with faster electro-optic detection, will improve the dynamic range of the system. Recording waveforms at faster rates will allow us to average a large number of waveforms in a short amount time, thereby lowering the noise floor, so that we can achieve a dynamic range approaching 100 dB. The portability feature of the system allows us to perform broadband and sensitive THz spectroscopy in any lab of our choosing, opening the door to revealing THz properties of sensitive materials or samples that may need to remain in a controlled

environment. Although we did not have the opportunity to implement this fast detection technique or further miniaturize and industrialize this system, the prototype presented in this thesis has great potential to become a successful commercial THz system. Its unique spectral properties and peak sensitivity at 3.5 THz fill a void in the commercially available time-resolved THz spectrometer market. The low-cost components it relies on also makes it an enticing system for consumers wishing to dabble in broadband THz spectroscopy without breaking the bank and without sacrificing performance. The performance specifications of this prototype are already comparable to other schemes utilizing complex, large, and high power ultrafast sources at a fraction of the cost [141].

The THz system relying on the kagomé HCPCF and GaSe crystals may be used to generate tunable THz spectra up to 20 THz by simply varying the pulse energy injected into the fiber. Though we cannot access all these frequencies (0-20 THz) at once, we can use this system to easily extract information of a sample up to 20 THz. Seeing as this system relies on a one-of-a-kind fiber, it does not hold much value as a commercial product. However, this demonstration can inspire researchers to use a similar approach to tailor their NIR pulses to achieve a specific goal, using commercially available hollow-core fibers instead.

Finally, in chapter 6 we explored the extreme case of nonlinear propagation in optical fiber: SC generation. We used a solid-core PCF whose dispersive properties are engineered to shift the ZDW of the fiber towards the central wavelength of our laser and whose core is doped with germania to expand the transmitted bandwidth, reaching the mid-IR, and increase the nonlinear refractive index of the core. Though we did not accomplish the generation of mid-IR radiation in this fiber, we nevertheless discovered interesting phenomena. We investigated the polarization properties of this weakly birefringent PCF and discovered that solitons also preserve their polarization and shorter wavelengths (higher frequencies) are more susceptible to depolarization than longer wavelengths (lower frequencies). We associated this wavelength-dependent depolarization to a Rayleigh-like effect preferentially scattering shorter wavelengths into the orthogonal principal axis of the fiber.

In the future, exploring the polarization properties of a highly birefringent PCF with nearly identical dispersive properties should be performed. Often, the polarization properties of the entire broadband spectrum are not measured but rather at a single wavelength, largely due to the lack of a polarization sensitive spectrometer covering extremely broad spectral windows. Exploring highly birefringent fibers tailored for SC generation to reveal true polarization-maintaining capabilities across a broadband spectrum is crucial for ap-

plications requiring a clean polarization state and extremely large spectral bandwidth like high-contrast optical coherence tomography [142]. Moreover, extracting all the Stokes parameters across the entire spectrum of the SC would be an interesting experiment as it would reveal the polarization ellipse of each spectral component.

We hope that we have convinced the reader that optical fibers (of all kinds) should be a standard component in their lab and not just as a vessel to easily guide light where they need it to go (although this is a very nice bonus feature). As researchers continue to design and fabricate new optical fibers, the possibilities become endless for these useful and user-friendly pieces of equipment.

Bibliography

[1] X.-C. Zhang and J. Xu, *Introduction to THz Wave Photonics* (Springer US, Boston, MA, 2010).

[2] J. K. Ranka, R. S. Windeler, and A. J. Stentz, "Visible continuum generation in air–silica microstructure optical fibers with anomalous dispersion at 800 nm," Opt. Lett. **25**, 25–27 (2000).

[3] K. Okamoto, *Fundamentals of Optical Waveguides* (Academic Press), 2nd ed.

[4] G. Agrawal, *Nonlinear Fiber Optics* (Elsevier, 2013), 5th ed.

[5] Q. Wu and X.-C. Zhang, "Design and characterization of traveling-wave electrooptic terahertz sensors," IEEE Journal of Selected Topics in Quantum Electronics **2**, 693–700 (1996).

[6] F. P. Kapron, D. B. Keck, and R. D. Maurer, "Radiation losses in glass optical waveguides," Appl. Phys. Lett. **17**, 423–425 (1970).

[7] R. Stolen and A. Ashkin, "Optical Kerr effect in glass waveguide," Appl. Phys. Lett. **22**, 294–296 (1973).

[8] R. Stolen, "Phase-matched-stimulated four-photon mixing in silica-fiber waveguides," IEEE J. Quant. Electron. **11**, 100–103 (1975).

[9] R. H. Stolen, E. P. Ippen, and A. R. Tynes, "Raman Oscillation in Glass Optical Waveguide," Appl. Phys. Lett. **20**, 62–64 (1972).

[10] R. H. Stolen and C. Lin, "Self-phase-modulation in silica optical fibers," Phys. Rev. A **17**, 1448–1453 (1978).

[11] A. Hasegawa and F. Tappert, "Transmission of stationary nonlinear optical pulses in dispersive dielectric fibers. I. Anomalous dispersion," Appl. Phys. Lett. **23**, 142–144 (1973).

[12] L. F. Mollenauer, R. H. Stolen, and J. P. Gordon, "Experimental Observation of Picosecond Pulse Narrowing and Solitons in Optical Fibers," Phys. Rev. Lett. **45**, 1095–1098 (1980).

[13] L. F. Mollenauer and R. H. Stolen, "The soliton laser," Opt. Lett. **9**, 13–15 (1984).

[14] J. C. Knight, T. A. Birks, P. S. J. Russell, and D. M. Atkin, "All-silica single-mode optical fiber with photonic crystal cladding," Opt. Lett. **21**, 1547–1549 (1996).

[15] B. J. Eggleton, C. Kerbage, P. S. Westbrook, R. S. Windeler, and A. Hale, "Microstructured optical fiber devices," Opt. Express **9**, 698–713 (2001).

[16] R. S. Windeler, J. L. Wagener, and D. J. DiGiovanni, "Silica-Air Microstructured Fibers: Properties and Applications," in *Optical Fiber Communication Conference and the International Conference on Integrated Optics and Optical Fiber Communication (1999), paper FG1,* (Optica Publishing Group, 1999), p. FG1.

[17] T. A. Birks, J. C. Knight, and P. S. J. Russell, "Endlessly single-mode photonic crystal fiber," Opt. Lett. **22**, 961–963 (1997).

[18] F. Silva, D. R. Austin, A. Thai, M. Baudisch, M. Hemmer, D. Faccio, A. Couairon, and J. Biegert, "Multi-octave supercontinuum generation from mid-infrared filamentation in a bulk crystal," Nat. Commun. **3**, 807 (2012).

[19] J. M. Dudley, G. Genty, and S. Coen, "Supercontinuum generation in photonic crystal fiber," Rev. Mod. Phys. **78**, 1135–1184 (2006).

[20] R. Dorsinville, P. Ho, J. Manassah, and R. Alfano, "Applications of Supercontinuum: Present and Future," in *The Supercontinuum Laser Source: Fundamentals with Updated References,* R. R. Alfano, ed. (Springer, New York, NY, 2006), pp. 377–398.

[21] D. H. Auston, "Picosecond optoelectronic switching and gating in silicon," Appl. Phys. Lett. **26**, 101 (1975).

[22] D. Strickland and G. Mourou, "Compression of amplified chirped optical pulses," Opt. Commun. **56**, 219–221 (1985).

[23] W. Zouaghi, M. D. Thomson, K. Rabia, R. Hahn, V. Blank, and H. G. Roskos, "Broadband terahertz spectroscopy: principles, fundamental research and potential for industrial applications," Eur. J. Phys. **34**, S179 (2013).

[24] M. Tonouchi, "Cutting-edge terahertz technology," Nat. Photon. **1**, 97–105 (2007).

[25] J. Xu, K. W. Plaxco, and S. J. Allen, "Absorption spectra of liquid water and aqueous buffers between 0.3 and 3.72THz," J. Chem. Phys. **124**, 036101 (2006).

[26] A. Redo-Sanchez, B. Heshmat, A. Aghasi, S. Naqvi, M. Zhang, J. Romberg, and R. Raskar, "Terahertz time-gated spectral imaging for content extraction through layered structures," Nat. Commun. **7**, 12665 (2016).

[27] J. F. Federici, B. Schulkin, F. Huang, D. Gary, R. Barat, F. Oliveira, and D. Zimdars, "THz imaging and sensing for security applications—explosives, weapons and drugs," Semicond. Sci. Technol. **20**, S266–S280 (2005).

[28] L. Ho, M. Pepper, and P. Taday, "Signatures and fingerprints," Nat. Photon. **2**, 541–543 (2008).

[29] A. Hirata, T. Kosugi, H. Takahashi, R. Yamaguchi, F. Nakajima, T. Furuta, H. Ito, H. Sugahara, Y. Sato, and T. Nagatsuma, "120-GHz-band millimeter-wave photonic wireless link for 10-Gb/s data transmission," IEEE Trans. Microw. Theory Tech. **54**, 1937–1944 (2006).

[30] P. Sen, J. V. Siles, N. Thawdar, and J. M. Jornet, "Multi-kilometre and multi-gigabit-per-second sub-terahertz communications for wireless backhaul applications," Nat. Electron. **6**, 164–175 (2023).

[31] J. D. Buron, D. M. A. Mackenzie, D. H. Petersen, A. Pesquera, A. Centeno, P. Bøggild, A. Zurutuza, and P. U. Jepsen, "Terahertz wafer-scale mobility mapping

of graphene on insulating substrates without a gate," Opt. Express **23**, 30721–30729 (2015).

[32] S. Scarfe, W. Cui, A. Luican-Mayer, and J.-M. Ménard, "Systematic THz study of the substrate effect in limiting the mobility of graphene," Sci. Rep. **11**, 8729 (2021).

[33] N. Couture, W. Cui, M. Lippl, R. Ostic, D. J. J. Fandio, E. K. Yalavarthi, A. Vishnuradhan, A. Gamouras, N. Y. Joly, and J.-M. Ménard, "Single-pulse terahertz spectroscopy monitoring sub-millisecond time dynamics at a rate of 50 kHz," Nat. Commun. **14**, 2595 (2023).

[34] N. Couture, J. Schlosser, A. Ahmed, M. Wahbeh, G. Best, A. Gamouras, and J.-M. Ménard, "Compact, low-cost, and broadband terahertz time-domain spectrometer," Appl. Opt. **62**, 4097 (2023).

[35] A. Halpin, N. Couture, and J.-M. Ménard, "Optical pulse structuring in gas-filled hollow-core kagomé PCF for generation and detection of phase-locked multi-THz pulses [Invited]," Opt. Mater. Express **9**, 3115–3122 (2019).

[36] N. Couture, R. Ostic, P. H. Reddy, A. K. Kar, M. C. Paul, and J.-M. Ménard, "Polarization-resolved supercontinuum generated in a germania-doped photonic crystal fiber," J. Phys. Photonics **3**, 025002 (2021).

[37] D. Gloge, "Weakly Guiding Fibers," Appl. Opt. **10**, 2252–2258 (1971).

[38] D. Mogilevtsev, T. A. Birks, and P. S. J. Russell, "Group-velocity dispersion in photonic crystal fibers," Opt. Lett. **23**, 1662–1664 (1998).

[39] J. C. Knight, T. A. Birks, P. S. J. Russell, and J. P. d. Sandro, "Properties of photonic crystal fiber and the effective index model," J. Opt. Soc. Am. A **15**, 748–752 (1998).

[40] W. H. Reeves, D. V. Skryabin, F. Biancalana, J. C. Knight, P. S. J. Russell, F. G. Omenetto, A. Efimov, and A. J. Taylor, "Transformation and control of ultra-short pulses in dispersion-engineered photonic crystal fibres," Nature **424**, 511–515 (2003).

[41] G. Genty, M. Lehtonen, H. Ludvigsen, and M. Kaivola, "Enhanced bandwidth of supercontinuum generated in microstructured fibers," Opt. Express **12**, 3471–3480 (2004).

[42] K. M. Hilligsøe, T. V. Andersen, H. N. Paulsen, C. K. Nielsen, K. Mølmer, S. Keiding, R. Kristiansen, K. P. Hansen, and J. J. Larsen, "Supercontinuum generation in a photonic crystal fiber with two zero dispersion wavelengths," Opt. Express **12**, 1045–1054 (2004).

[43] A. M. Heidt, "Pulse preserving flat-top supercontinuum generation in all-normal dispersion photonic crystal fibers," J. Opt. Soc. Am. B **27**, 550–559 (2010).

[44] M. Lippl, M. H. Frosz, and N. Y. Joly, "Low-noise supercontinuum generation in chiral all-normal dispersion photonic crystal fibers," Opt. Lett. **48**, 5297–5300 (2023).

[45] J. Noda, K. Okamoto, and Y. Sasaki, "Polarization-maintaining fibers and their applications," J. Lightwave Technol. **4**, 1071–1089 (1986).

[46] R. W. Boyd, *Nonlinear Optics* (Academic Press, 2008), 3rd ed.

[47] N. Akhmediev and M. Karlsson, "Cherenkov radiation emitted by solitons in optical fibers," Phys. Rev. A **51**, 2602–2607 (1995).

[48] I. Cristiani, R. Tediosi, L. Tartara, and V. Degiorgio, "Dispersive wave generation by solitons in microstructured optical fibers," Opt. Express **12**, 124–135 (2004).

[49] O. Heavens, "Handbook of Optical Constants of Solids II," J. Mod. Opt. **39**, 189–189 (1992).

[50] A. Leitenstorfer, S. Hunsche, J. Shah, M. C. Nuss, and W. H. Knox, "Detectors and sources for ultrabroadband electro-optic sampling: Experiment and theory," Appl. Phys. Lett. **74**, 1516–1518 (1999).

[51] A. Nahata, D. H. Auston, T. F. Heinz, and C. Wu, "Coherent detection of freely propagating terahertz radiation by electro-optic sampling," Appl. Phys. Lett. **68**, 150–152 (1996).

[52] N. C. J. v. d. Valk, T. Wenckebach, and P. C. M. Planken, "Full mathematical description of electro-optic detection in optically isotropic crystals," J. Opt. Soc. Am. B **21**, 622–631 (2004).

[53] Y.-S. Lee, *Principles of Terahertz Science and Technology* (Springer US, Boston, MA, 2009).

[54] F. Blanchard, L. Razzari, H.-C. Bandulet, G. Sharma, R. Morandotti, J.-C. Kieffer, T. Ozaki, M. Reid, H. F. Tiedje, H. K. Haugen, and F. A. Hegmann, "Generation of 1.5 J single-cycle terahertz pulses by optical rectification from a large aperture ZnTe crystal," Opt. Express **15**, 13212–13220 (2007).

[55] B. Urbanek, M. Möller, M. Eisele, S. Baierl, D. Kaplan, C. Lange, and R. Huber, "Femtosecond terahertz time-domain spectroscopy at 36kHz scan rate using an acousto-optic delay," Appl. Phys. Lett. **108**, 121101 (2016).

[56] D. Molter, F. Ellrich, T. Weinland, S. George, M. Goiran, F. Keilmann, R. Beigang, and J. Léotin, "High-speed terahertz time-domain spectroscopy of cyclotron resonance in pulsed magnetic field," Opt. Express **18**, 26163–26168 (2010).

[57] C. Hoberg, P. Balzerowski, and M. Havenith, "Integration of a rapid scanning technique into THz time-domain spectrometers for nonlinear THz spectroscopy measurements," AIP Adv. **9**, 035348 (2019).

[58] S. M. Teo, B. K. Ofori-Okai, C. A. Werley, and K. A. Nelson, "Invited Article: Single-shot THz detection techniques optimized for multidimensional THz spectroscopy," Rev. Sci. Instrum. **86**, 051301 (2015).

[59] J. Shan, A. S. Weling, E. Knoesel, L. Bartels, M. Bonn, A. Nahata, G. A. Reider, and T. F. Heinz, "Single-shot measurement of terahertz electromagnetic pulses by use of electro-optic sampling," Opt. Lett. **25**, 426–428 (2000).

[60] Y. Minami, Y. Hayashi, J. Takeda, and I. Katayama, "Single-shot measurement of a terahertz electric-field waveform using a reflective echelon mirror," Appl. Phys. Lett. **103**, 051103 (2013).

[61] T. Yasui, E. Saneyoshi, and T. Araki, "Asynchronous optical sampling terahertz time-domain spectroscopy for ultrahigh spectral resolution and rapid data acquisition," Appl. Phys. Lett. **87**, 061101 (2005).

[62] T. Hochrein, R. Wilk, M. Mei, R. Holzwarth, N. Krumbholz, and M. Koch, "Optical sampling by laser cavity tuning," Opt. Express **18**, 1613–1617 (2010).

[63] G. Sharma, K. Singh, I. Al-Naib, R. Morandotti, and T. Ozaki, "Terahertz detection using spectral domain interferometry," Opt. Lett. **37**, 4338–4340 (2012).

[64] Z. Jiang and X.-C. Zhang, "Electro-optic measurement of THz field pulses with a chirped optical beam," Appl. Phys. Lett. **72**, 1945–1947 (1998).

[65] F. G. Sun, Z. Jiang, and X.-C. Zhang, "Analysis of terahertz pulse measurement with a chirped probe beam," Appl. Phys. Lett. **73**, 2233–2235 (1998).

[66] E. Roussel, C. Szwaj, C. Evain, B. Steffen, C. Gerth, B. Jalali, and S. Bielawski, "Phase Diversity Electro-optic Sampling: A new approach to single-shot terahertz waveform recording," Light Sci. Appl. **11**, 14 (2022).

[67] F. Y. Gao, Z. Zhang, Z.-J. Liu, and K. A. Nelson, "High-speed two-dimensional terahertz spectroscopy with echelon-based shot-to-shot balanced detection," Opt. Lett. **47**, 3479–3482 (2022).

[68] K. Goda, D. R. Solli, K. K. Tsia, and B. Jalali, "Theory of amplified dispersive Fourier transformation," Phys. Rev. A **80**, 043821 (2009).

[69] W. Withayachumnankul and M. Naftaly, "Fundamentals of Measurement in Terahertz Time-Domain Spectroscopy," J. Infrared Millim. Terahertz Waves **35**, 610–637 (2014).

[70] I. Pupeza, R. Wilk, and M. Koch, "Highly accurate optical material parameter determination with THz time-domain spectroscopy," Opt. Express **15**, 4335–4350 (2007).

[71] M. Scheller and M. Koch, "Fast and Accurate Thickness Determination of Unknown Materials using Terahertz Time Domain Spectroscopy," J. Infrared Millim. Terahertz Waves **30**, 762–769 (2009).

[72] J. A. Armstrong, "Measurement of picosecond laser pulse widths," Appl. Phys. Lett. **10**, 16–18 (1967).

[73] R. Paschotta, *Field guide to laser pulse generation*, vol. FG14 (SPIE, 2008).

[74] D. Kane and R. Trebino, "Characterization of arbitrary femtosecond pulses using frequency-resolved optical gating," IEEE J. Quant. Electron. **29**, 571–579 (1993).

[75] K. W. DeLong, R. Trebino, J. Hunter, and W. E. White, "Frequency-resolved optical gating with the use of second-harmonic generation," J. Opt. Soc. Am. B **11**, 2206–2215 (1994).

[76] R. Trebino, *Frequency-Resolved Optical Gating: The Measurement of Ultrashort Laser Pulses: The Measurement of Ultrashort Laser Pulses* (Springer Science & Business Media, 2000).

[77] P. J. Collings, "Simple measurement of the band gap in silicon and germanium," Am. J. Phys. **48**, 197–199 (1980).

[78] D. Grischkowsky, S. Keiding, M. v. Exter, and C. Fattinger, "Far-infrared time-domain spectroscopy with terahertz beams of dielectrics and semiconductors," J. Opt. Soc. Am. B **7**, 2006–2015 (1990).

[79] E. V. Loewenstein, D. R. Smith, and R. L. Morgan, "Optical Constants of Far Infrared Materials. 2: Crystalline Solids," Appl. Opt. **12**, 398–406 (1973).

[80] K. Aoki, J. Savolainen, and M. Havenith, "Broadband terahertz pulse generation by optical rectification in GaP crystals," Appl. Phys. Lett. **110**, 201103 (2017).

[81] Q. Wu and X. Zhang, "Ultrafast electro-optic field sensors," Appl. Phys. Lett. **68**, 1604–1606 (1996).

[82] D. F. Nelson and E. H. Turner, "Electro-optic and Piezoelectric Coefficients and Refractive Index of Gallium Phosphide," J. Appl. Phys. **39**, 3337–3343 (1968).

[83] V. G. Dmitriev, G. G. Gurzadyan, and D. N. Nikogosyan, *Handbook of Nonlinear Optical Crystals* (Springer Berlin Heidelberg, 2014).

[84] M. Nakamura, S. Higuchi, S. Takekawa, K. Terabe, Y. Furukawa, and K. Kitamura, "Optical Damage Resistance and Refractive Indices in Near-Stoichiometric MgO-Doped LiNbO3," Jpn. J. Appl. Phys. **41**, L49 (2002).

[85] L. Pálfalvi, J. Hebling, J. Kuhl, Péter, and K. Polgár, "Temperature dependence of the absorption and refraction of Mg-doped congruent and stoichiometric LiNbO3 in the THz range," J. Appl. Phys. **97**, 123505 (2005).

[86] J. Hebling, K.-L. Yeh, M. C. Hoffmann, B. Bartal, and K. A. Nelson, "Generation of high-power terahertz pulses by tilted-pulse-front excitation and their application possibilities," J. Opt. Soc. Am. B **25**, B6–B19 (2008).

[87] M. C. Hoffmann and J. A. Fülöp, "Intense ultrashort terahertz pulses: generation and applications," J. Phys. D: Appl. Phys. **44**, 083001 (2011).

[88] M. C. Hoffmann, J. Hebling, H. Y. Hwang, K.-L. Yeh, and K. A. Nelson, "THz-pump/THz-probe spectroscopy of semiconductors at high field strengths [Invited]," J. Opt. Soc. Am. B **26**, A29–A34 (2009).

[89] E. Roussel, C. Evain, M. Le Parquier, C. Szwaj, S. Bielawski, L. Manceron, J.-B. Brubach, M.-A. Tordeux, J.-P. Ricaud, L. Cassinari, M. Labat, M.-E. Couprie, and P. Roy, "Observing microscopic structures of a relativistic object using a time-stretch strategy," Sci. Rep. **5**, 10330 (2015).

[90] A. Gamouras, N. Couture, W. Cui, M. Lippl, R. Ostic, D. J. J. Fandio, E. K. Yalavarthi, A. V. Radhan, N. Y. Joly, and J.-M. Ménard, "Capturing microsecond dynamics one pulse at a time: single-shot time-resolved terahertz spectroscopy at 50 kHz," in *Ultrafast Phenomena and Nanophotonics XXVII,* vol. PC12419 (SPIE, 2023).

[91] N. Couture, W. Cui, M. Lippl, R. Ostic, D. J. J. Fandio, E. K. Yalavarthi, A. V. Radhan, A. Gamouras, N. Joly, and J.-M. Ménard, "Resolving sub-millisecond dynamics with single-pulse terahertz time-domain spectroscopy," in *Frontiers in Optics + Laser Science 2022 (FIO, LS) (2022), paper FW6C.2,* (Optica Publishing Group, 2022), p. FW6C.2.

[92] N. Couture, M. Lippl, W. Cui, R. Ostic, D. J. J. Fandio, E. K. Yalavarthi, A. Vishnuradhan, A. Gamouras, N. Y. Joly, and J.-M. Ménard, "Towards single-pulse terahertz spectroscopy at MHz rates," in *2023 48th International Conference on Infrared, Millimeter, and Terahertz Waves (IRMMW-THz),* (2023), pp. 1–2. ISSN: 2162-2035.

[93] N. Couture, M. Lippl, W. Cui, A. Gamouras, N. Y. Joly, and J.-M. Ménard, "Performance analysis of table-top single-pulse terahertz detection up to 1.1 MHz," (2023). ArXiv:2309.09803.

[94] R. Szipöcs, K. Ferencz, C. Spielmann, and F. Krausz, "Chirped multilayer coatings for broadband dispersion control in femtosecond lasers," Opt. Lett. **19**, 201–203 (1994).

[95] P. S. J. Russell, "Photonic Crystal Fibers," Science **299**, 358–362 (2003).

[96] M. A. Duguay, Y. Kokubun, T. L. Koch, and L. Pfeiffer, "Antiresonant reflecting optical waveguides in SiO2-Si multilayer structures," Appl. Phys. Lett. **49**, 13–15 (1986).

[97] M. O'Keeffe and B. Hyde, *Crystal Structures I. Patterns and Symmetry* (Mineralogical Society of America, 1996).

[98] J. Nold, P. Hölzer, N. Y. Joly, G. K. L. Wong, A. Nazarkin, A. Podlipensky, M. Scharrer, and P. S. J. Russell, "Pressure-controlled phase matching to third harmonic in Ar-filled hollow-core photonic crystal fiber," Opt. Lett. **35**, 2922–2924 (2010).

[99] P. S. J. Russell, P. Hölzer, W. Chang, A. Abdolvand, and J. C. Travers, "Hollow-core photonic crystal fibres for gas-based nonlinear optics," Nat. Photon. **8**, 278–286 (2014).

[100] F. Köttig, F. Tani, C. M. Biersach, J. C. Travers, and P. S. J. Russell, "Generation of microjoule pulses in the deep ultraviolet at megahertz repetition rates," Optica **4**, 1272–1276 (2017).

[101] F. Köttig, D. Novoa, F. Tani, M. C. Günendi, M. Cassataro, J. C. Travers, and P. S. J. Russell, "Mid-infrared dispersive wave generation in gas-filled photonic crystal fibre by transient ionization-driven changes in dispersion," Nat. Commun. **8**, 813 (2017).

[102] A. I. Adamu, M. S. Habib, C. R. Petersen, J. E. A. Lopez, B. Zhou, A. Schülzgen, M. Bache, R. Amezcua-Correa, O. Bang, and C. Markos, "Deep-UV to Mid-IR Supercontinuum Generation driven by Mid-IR Ultrashort Pulses in a Gas-filled Hollow-core Fiber," Sci. Rep. **9**, 4446 (2019).

[103] N. Y. Joly, J. Nold, W. Chang, P. Hölzer, A. Nazarkin, G. K. L. Wong, F. Biancalana, and P. S. Russell, "Bright Spatially Coherent Wavelength-Tunable Deep-UV Laser Source Using an Ar-Filled Photonic Crystal Fiber," Phys. Rev. Lett. **106**, 203901 (2011).

[104] A. Ermolov, K. F. Mak, M. H. Frosz, J. C. Travers, and P. S. J. Russell, "Supercontinuum generation in the vacuum ultraviolet through dispersive-wave and soliton-plasma interaction in a noble-gas-filled hollow-core photonic crystal fiber," Phys. Rev. A **92**, 033821 (2015).

[105] A. Ermolov, C. Heide, P. Dienstbier, F. Köttig, F. Tani, P. Hommelhoff, and P. S. Russell, "Carrier-envelope-phase-stable soliton-based pulse compression to 4.4fs and ultraviolet generation at the 800kHz repetition rate," Opt. Lett. **44**, 5005–5008 (2019).

[106] R. F. Cregan, B. J. Mangan, J. C. Knight, T. A. Birks, P. S. J. Russell, P. J. Roberts, and D. C. Allan, "Single-Mode Photonic Band Gap Guidance of Light in Air," Science **285**, 1537–1539 (1999).

[107] W. Cui, A. W. Schiff-Kearn, E. Zhang, N. Couture, F. Tani, D. Novoa, P. S. Russell, and J.-M. Ménard, "Broadband and tunable time-resolved THz system using argon-filled hollow-core photonic crystal fiber," APL Photonics **3**, 111301 (2018).

[108] N. Couture, M. Wahbeh, A. Ahmed, G. Best, A. Gamouras, and J.-M. Ménard, "Portable, broadband, and sensitive terahertz time-domain spectrometer," in *Nonlinear Frequency Generation and Conversion: Materials and Devices XXII,* vol. 12405 (SPIE, 2023), pp. 46–49.

[109] W. Cui, K. M. Awan, R. Huber, K. Dolgaleva, and J.-M. Ménard, "Broadband and High-Sensitivity Time-Resolved THz System Using Grating-Assisted Tilted-Pulse-Front Phase Matching," Adv. Opt. Mater. **10**, 2101136 (2022).

[110] A. Halpin, W. Cui, A. W. Schiff-Kearn, K. M. Awan, K. Dolgaleva, and J.-M. Ménard, "Enhanced Terahertz Detection Efficiency via Grating-Assisted Noncollinear Electro-Optic Sampling," Phys. Rev. Appl. **12**, 031003 (2019).

[111] M. Bashirpour, W. Cui, A. Gamouras, and J.-M. Ménard, "Scalable Fabrication of Nanogratings on GaP for Efficient Diffraction of Near-Infrared Pulses and Enhanced Terahertz Generation by Optical Rectification," Crystals **12**, 684 (2022).

[112] W. Cui, E. K. Yalavarthi, A. V. Radhan, M. Bashirpour, A. Gamouras, and J.-M. Ménard, "High-field THz source centered at 2.6 THz," Opt. Express **31**, 32468–32477 (2023).

[113] R. Rautela, S. Scarfe, J.-M. Guay, P. Lazar, M. Pykal, S. Azimi, C. Grenapin, J. Boddison-Chouinard, A. Halpin, W. Wang, L. Andrzejewski, R. Plumadore, J. Park, J.-M. Ménard, M. Otyepka, and A. Luican-Mayer, "Mechanistic Insight into the Limiting Factors of Graphene-Based Environmental Sensors," ACS Appl. Mater. Interfaces **12**, 39764–39771 (2020).

[114] K. Liu, J. Xu, and X.-C. Zhang, "GaSe crystals for broadband terahertz wave detection," Appl. Phys. Lett. **85**, 863–865 (2004).

[115] M. Montesinos-Ballester, C. Lafforgue, J. Frigerio, A. Ballabio, V. Vakarin, Q. Liu, J. M. Ramirez, X. Le Roux, D. Bouville, A. Barzaghi, C. Alonso-Ramos, L. Vivien, G. Isella, and D. Marris-Morini, "On-Chip Mid-Infrared Supercontinuum Generation from 3 to 13 m Wavelength," ACS Photonics **7**, 3423–3429 (2020).

[116] L. Zhang, Y. Yan, Y. Yue, Q. Lin, O. Painter, R. G. Beausoleil, and A. E. Willner, "On-chip two-octave supercontinuum generation by enhancing self-steepening of optical pulses," Opt. Express **19**, 11584–11590 (2011).

[117] J. S. Sanghera, L. B. Shaw, and I. D. Aggarwal, "Applications of chalcogenide glass optical fibers," C. R. Chim. **5**, 873–883 (2002).

[118] F. M. Cox, A. Argyros, and M. C. J. Large, "Liquid-filled hollow core microstructured polymer optical fiber," Opt. Express **14**, 4135–4140 (2006).

[119] F. Tani, J. C. Travers, and P. S. J. Russell, "Multimode ultrafast nonlinear optics in optical waveguides: numerical modeling and experiments in kagomé photonic-crystal fiber," J. Opt. Soc. Am. B **31**, 311–320 (2014).

[120] S. Nagel, J. MacChesney, and K. Walker, "An Overview of the Modified Chemical Vapor Deposition (MCVD) Process and Performance," IEEE Trans. Microw. Theory Tech. **30**, 305–322 (1982).

[121] U. G. Akhmetshin, V. A. Bogatyrev, A. K. Senatorov, A. A. Sysolyatin, and M. G. Shalygin, "New single-mode fibres with the flat spectral dependence of the chromatic dispersion varying over the fibre length," Quantum Electron. **33**, 265 (2003).

[122] S. Coen, A. H. L. Chau, R. Leonhardt, J. D. Harvey, J. C. Knight, W. J. Wadsworth, and P. S. J. Russell, "Supercontinuum generation by stimulated Raman scattering and parametric four-wave mixing in photonic crystal fibers," J. Opt. Soc. Am. B **19**, 753–764 (2002).

[123] J. M. Dudley, L. Provino, N. Grossard, H. Maillotte, R. S. Windeler, B. J. Eggleton, and S. Coen, "Supercontinuum generation in air–silica microstructured fibers with nanosecond and femtosecond pulse pumping," J. Opt. Soc. Am. B **19**, 765–771 (2002).

[124] N. I. Nikolov, T. Sørensen, O. Bang, and A. Bjarklev, "Improving efficiency of supercontinuum generation in photonic crystal fibers by direct degenerate four-wave mixing," J. Opt. Soc. Am. B **20**, 2329–2337 (2003).

[125] D. Nolan, X. Chen, and M.-J. Li, "Fibers with low polarization-mode dispersion," J. Lightwave Technol. **22**, 1066–1077 (2004).

[126] M. Czerny and A. F. Turner, "Über den Astigmatismus bei Spiegelspektrometern," Z. Physik **61**, 792–797 (1930).

[127] N. Couture, R. Ostic, P. H. Reddy, S. Das, A. Dhar, M. Pal, M. C. Paul, A. K. Kar, and J.-M. Ménard, "Polarization analysis of a supercontinuum generated in a germania-doped photonic crystal fiber," in *Conference on Lasers and Electro-Optics (2020), paper JW2E.12,* (Optica Publishing Group, 2020), p. JW2E.12.

[128] N. Couture, R. Ostic, P. H. Reddy, A. K. Kar, M. C. Paul, and J.-M. Ménard, "Polarization resolution of a fiber-based supercontinuum spanning more than 2 octaves," in *Frontiers in Optics / Laser Science (2020), paper FTh1E.5,* (Optica Publishing Group, 2020), p. FTh1E.5.

[129] R. Ostic, N. Couture, P. H. Reddy, A. K. Kar, M. C. Paul, and J.-M. Ménard, "Simulation of Linear Depolarization Effects During Supercontinuum Generation in Optical Fiber," in *2021 Photonics North (PN),* (2021), pp. 1–1. ISSN: 2693-8316.

[130] S.-J. Kim, B. J. Kang, U. Puc, W. T. Kim, M. Jazbinsek, F. Rotermund, and O.-P. Kwon, "Highly Nonlinear Optical Organic Crystals for Efficient Terahertz Wave Generation, Detection, and Applications," Advanced Optical Materials **9**, 2101019 (2021).

[131] S. Mansourzadeh, T. Vogel, M. Shalaby, F. Wulf, and C. J. Saraceno, "Milliwatt average power, MHz-repetition rate, broadband THz generation in organic crystal BNA with diamond substrate," Opt. Express **29**, 38946–38957 (2021).

[132] S. Mansourzadeh, T. Vogel, A. Omar, M. Shalaby, M. Cinchetti, and C. J. Saraceno, "Broadband, high power THz source at 540 kHz using organic crystal BNA," APL Photonics **8**, 011301 (2023).

[133] S. Mansourzadeh, T. Vogel, A. Omar, T. O. Buchmann, E. J. R. Kelleher, P. U. Jepsen, and C. J. Saraceno, "Towards intense ultra-broadband high repetition rate terahertz sources based on organic crystals [Invited]," Opt. Mater. Express **13**, 3287–3308 (2023).

[134] M. C. Thompson, B. A. Barad, A. M. Wolff, H. Sun Cho, F. Schotte, D. M. C. Schwarz, P. Anfinrud, and J. S. Fraser, "Temperature-jump solution X-ray scattering reveals distinct motions in a dynamic enzyme," Nat. Chem. **11**, 1058–1066 (2019).

[135] A. M. Wolff, E. Nango, I. D. Young, A. S. Brewster, M. Kubo, T. Nomura, M. Sugahara, S. Owada, B. A. Barad, K. Ito, A. Bhowmick, S. Carbajo, T. Hino, J. M. Holton, D. Im, L. J. O'Riordan, T. Tanaka, R. Tanaka, R. G. Sierra, F. Yumoto, K. Tono, S. Iwata, N. K. Sauter, J. S. Fraser, and M. C. Thompson, "Mapping Protein Dynamics at High-Resolution with Temperature-Jump X-ray Crystallography," (2022). BioRxiv 2022.06.10.495662.

[136] L. Ho, R. Müller, M. Römer, K. C. Gordon, J. Heinämäki, P. Kleinebudde, M. Pepper, T. Rades, Y. C. Shen, C. J. Strachan, P. F. Taday, and J. A. Zeitler, "Analysis

of sustained-release tablet film coats using terahertz pulsed imaging," J. Control. Release p. 9 (2007).

[137] P. Bawuah, D. Markl, A. Turner, M. Evans, A. Portieri, D. Farrell, R. Lucas, A. Anderson, D. J. Goodwin, and J. A. Zeitler, "A Fast and Non-destructive Terahertz Dissolution Assay for Immediate Release Tablets," J. Pharm. Sci. **110**, 2083–2092 (2021).

[138] P. Bawuah and J. A. Zeitler, "Advances in terahertz time-domain spectroscopy of pharmaceutical solids: A review," TrAC Trends Anal. Chem. **139**, 116272 (2021).

[139] R. I. Stantchev, X. Yu, T. Blu, and E. Pickwell-MacPherson, "Real-time terahertz imaging with a single-pixel detector," Nat. Commun. **11**, 2535 (2020).

[140] J. Dong, P. You, A. Tomasino, A. Yurtsever, and R. Morandotti, "Single-shot ultrafast terahertz photography," Nat. Commun. **14**, 1704 (2023).

[141] F. Meyer, N. Hekmat, T. Vogel, A. Omar, S. Mansourzadeh, F. Fobbe, M. Hoffmann, Y. Wang, and C. J. Saraceno, "Milliwatt-class broadband THz source driven by a 112 W, sub-100 fs thin-disk laser," Opt. Express **27**, 30340–30349 (2019).

[142] J. F. d. Boer, C. K. Hitzenberger, and Y. Yasuno, "Polarization sensitive optical coherence tomography – a review [Invited]," Biomed. Opt. Express **8**, 1838–1873 (2017).